UNIVERSITY OF SOUTHAMPTON

NOVEL TECHNIQUES AND MATERIALS FOR OPTICAL TELECOMMUNICATION SYSTEMS

by Periklis Petropoulos

A thesis submitted for the degree of
Doctor of Philosophy

FACULTY OF ENGINEERING AND APPLIED SCIENCE

OPTOELECTRONICS RESEARCH CENTRE

DEPARTMENT OF ELECTRONICS AND COMPUTER SCIENCE

March 2000

UNIVERSITY OF SOUTHAMPTON

ABSTRACT

FACULTY OF ENGINEERING AND APPLIED SCIENCE
OPTOELECTRONICS RESEARCH CENTRE
DEPARTMENT OF ELECTRONICS AND COMPUTER SCIENCE

Doctor of Philosophy

NOVEL TECHNIQUES AND MATERIALS FOR OPTICAL TELECOMMUNICATION SYSTEMS

by Periklis Petropoulos

This thesis describes work on a variety of novel fibre-based, all-optical approaches to the implementation of several key telecommunications operations. It can be divided into two distinct parts.

The first part relates to the generation and coherent manipulation of short pulses in all-fibre systems. The development of an actively and harmonically mode-locked polarisation-maintaining erbium fibre ring laser operating at a repetition rate of 10GHz is first presented. Long-term stable operation is ensured by the use of an optical phase lock loop to maintain resonant operating conditions. The ring laser incorporated a long length of dispersion-shifted fibre that enhanced soliton compression of the generated pulses, and a filter to allow for tuneable operation within the erbium gain bandwidth. The output was in the form of 2 - 4ps nearly transform-limited solitons, the width of which depended on pump power. A series of characterisation measurements on this laser is presented. These include autocorrelation and optical spectrum measurements of the pulses, frequency resolved optical gating (FROG) characterisation, an interpulse noise measurement, jitter measurements using the RF spectrum of the pulses, and bit error-rate measurements.

A technique that uses superstructured fibre Bragg gratings for passively manipulating short pulses in a coherent manner is presented. The technique relies on filtering in both amplitude and phase the (broad) spectrum of the input pulses, thereby producing pulses of a desired spectral, and hence temporal response. The pulses generated from the erbium fibre ring laser were used in a series of experiments that demonstrated this technique. A basic pulse encoding and decoding scheme, pulse shaping of soliton pulses into square pulses, and repetition rate multiplication from 10 to 40GHz are presented.

The second part of the thesis concerns a detailed characterisation of the recently discovered optical nonlinearities associated with the reflectivity of a gallium:glass interface. It is demonstrated that such mirrors can be formed at the tip of a cleaved fibre. The reflectivity of these mirrors is shown to change at the erbium wavelengths by ~30% under suitable temperature and optical excitation. An assessment of the dependence of the magnitude, dynamics and optical phase response of the nonlinearity on temperature and pump power is carried out. The reproducibility of the nonlinear effect was also examined.

Gallium mirrors were then used to passively Q-switch a variety of fibre lasers. Due to their broadband nature, Q-switching of lasers of significantly different lasing wavelengths was achieved (1064 and 1550nm). Pulse energies up to 10μJ were obtained. This performance is directly comparable to that achieved using state-of-the-art (wavelength-selective) saturable absorbers.

List of Contents

PART ONE

PART TWO

List of Tables and Figures

Acknowledgements

Three years in the ORC seems to have been a long time, especially when I think how much I have learnt, and how much my way of thinking has changed within this period of time. Many people have influenced, helped and accompanied me in this long, and at times painful journey. I would like to grasp this opportunity and express my sincere gratitude to all of them.

I will start by thanking my supervisor Professor David Richardson, who is the person who always stood by my side, advised and encouraged me even at the most difficult moments. I have been very lucky that I had the opportunity to work with him.

Thanks are also due to the whole Advanced Fibre Technologies and Applications group, for being like a closest family within the ORC. Especially I would like to thank Dr. Herman Offerhaus, for help in the Q-switching experiments with gallium mirrors, Dr. Hyo Sang Kim for providing his expertise in the construction of the fibre interferometer described in section 4.8, and Dr. Neil Broderick for useful discussions.

I would like to thank Morten Ibsen, not only for sharing with me his expertise on fibre Bragg gratings and manufacturing all the gratings described in Chapter Two, but also for being a good companion and friend throughout the PhD years.

I am indebted to Dr. N.I. Zheludev of the Department of Physics and his research group, especially Dr. Peter Bennett and Dr. Suki Dhanjal, for their collaboration in the work described in Chapter Four.

I am also grateful to Dr. Harald Geiger and Alexander Fu for the pulse encoding and decoding experiment we did together. I would also like to thank all the people that constitute the ORC (and especially past and present residents of office P4103) for caring to give some advice or just share a smile. There is no doubt that the ORC has been the most stimulating work environment.

I gratefully acknowledge the contribution of Benn Thomsen and Professor John Harvey of the Univ. of Auckland, New Zealand, for all their help in setting up the FROG system and carrying out with me the FROG characterisation of the mode-locked laser. I am also grateful to Dr. Andy Ellis of BT Labs for invaluable help with the phase-lock loop and a number of measurements that are presented in Chapters One and Two.

I would also like to thank my family, who I miss so much, for their unconditional moral support, and all my friends, both the old ones and those who I have made during my stay in Southampton: I miss you all, and hope to see you again soon! But above all, I would like to thank Χαρις, who has marked the recent years of my life: Σε αγαπω πολυ!

Finally, I would like to acknowledge the University of Southampton and EPSRC for financial support by means of a joint studentship.

Principal Abbreviations

ASE	Amplified Spontaneous Emission
BER	Bit-Error-Rate
CDMA	Code-Division Multiple Access
CTA	Coherence Time Analyser
cw	Continuous-wave
DFB	Distributed Feedback
DOS	Density of States
DSF	Dispersion Shifted Fibre
DUT	Device under Test
EDFA	Erbium-Doped Fibre Amplifier
EFRL	Erbium-Fibre Ring Laser
FBG	Fibre Bragg Grating
FROG	Frequency-Resolved Optical Gating
FUT	Fibre under Test
FWHM	Full-Width at Half-Maximum
GVD	Group Velocity Dispersion
LMA	Large Mode Area
LO	Local Oscillator
MAN	Metropolitan Area Network
MQW	Multiple Quantum Well
NA	Numerical Aperture

OCDMA	Optical Code-Division Multiple Access
OPO	Optical Parametric Oscillator
OTDM	Optical Time-Division Multiplexing
PLD	Pulsed Laser Deposition
PLL	Phase-Lock Loop
PM	Polarisation-Maintaining
PZT	Piezo-electric Transducer
RF	Radio Frequency
RZ	Return-to-Zero
SESAM	Semiconductor Saturable Absorber Mirror
SHG	Second-Harmonic Generation
SPM	Self-Phase Modulation
TDMA	Time-Division Multiple Access
UV	Ultra-Violet
VCO	Voltage-Controlled Oscillator
WDM	Wavelength-Division Multiplexing

Introduction

It is already well established that optical fibre telecommunications offer important advantages over the radio frequency (RF) and microwave alternatives, such as the availability of a vast bandwidth and very low propagation loss. Optical communications is now the main mode of long-distance, high-bitrate communication, and its use in the implementation of Metropolitan Area Networks (MAN's) is considered more and more favourably. Until recently though, all processing of the data within such systems was carried out in the electrical domain, with optical fibres used only for the lower layer of communication, i.e. transmission. Thus, the main bandwidth limitation imposed on optical fibre systems was determined by the driving and receiving electronics. The current limit is around 40Gbit/s - a tiny fraction of the available transmission bandwidth of fibres. However, as technology evolves, and especially after the introduction of the erbium-doped fibre amplifier (EDFA), the most interesting direction for optical fibre systems lies in the development of all-optical telecommunication networks. Significant contributions towards this direction, from the perspective of passive devices, has been made by fibre Bragg grating (FBG) technology which has already been shown to offer significant advantages in add-drop filtering of wavelength-division multiplexed (WDM) channels and dispersion compensation. However, there is still a constant need for the development of new devices that will allow one to control and process the signal optically, as well as for the investigation of new nonlinear materials that will facilitate important network operations, such as ultrafast switching, modulation, routing, etc.

The activities described in this thesis have followed these lines. The context of the thesis, as well as its structure can be readily divided into two parts. The first part relates to research focusing on the generation and control of high-bit-rate short pulses, suitable for return-to-zero (RZ) telecommunication systems. Firstly, an all-fibre, high repetition frequency (10GHz) picosecond pulse source, suitable for high speed (100Gbit/s) applications is described (Chapter One). This was an actively and harmonically mode-locked erbium-fibre ring laser (EFRL). The laser used active control of the pulse repetition rate to match any environmental drift in the mode-locking frequency (~10GHz), and the generated pulses were soliton-compressed due to the inclusion of a long length of dispersion shifted fibre (DSF). The ring was ~500m long and consisted solely of polarisation-maintaining (PM) fibres and components to give optimum environmental stability. The chapter includes a review of previous work on such sources that led to the chosen cavity design. There are also descriptions of polarisation extinction measurements of components and measurements of the group velocity dispersion (GVD) of fibres, that were necessary for the implementation of the ring. The pulsed output was fully characterised in terms of pulse shape and duration using the frequency-resolved optical gating (FROG) technique; our results constitute the first reported FROG measurement of such a low-pulse-energy source. The laser output was also characterised in terms of tunability, inter-pulse noise, timing jitter, and overall noise performance (as assessed with bit-error-rate measurements). Availability of this source was critical for the investigation of novel techniques that can be used for pulse control in transmission systems.

Chapter Two describes a technique we have developed for coherent manipulation of short pulses and the experiments that were carried out to prove its feasibility. The technique uses superstructured fibre gratings and makes use of the relation that exists between their refractive index modulation profile and their reflectivity response. It was demonstrated in three independent experiments. The first concerned an optical encoder and decoder suitable for OCDMA systems. Although the experiment was elementary, involving short codes (patterns of just 7 chips) and a low bitrate of 125MHz, it was important as it demonstrated the prospects of optical coding/pattern recognition by the use of the coherence properties of fibre Bragg gratings operating in the Fourier regime. More sophisticated control was demonstrated in the latter two experiments, in the first of which, the soliton pulses of the mode-locked laser were re-shaped into pulses of a precise duration and an (almost) square shape. The full bandwidth of the input pulses was exploited and filtering of both its amplitude and phase was performed. In the last experiment multiplication of the repetition rate of the 10GHz mode-locked laser was performed to give a 40GHz output. The filter in this case, was a sinc-sampled grating that performed selective filtering of the spectral lines that define the 10GHz laser spectrum, without altering its envelope. Part One concludes in Chapter Three with a brief discussion on the further directions that this work is now following.

The second part of the thesis relates to the investigation of the optical nonlinearities that arise at a gallium:glass interface near the melting point of the metal. Chapter Four describes all the essential experiments that investigated the attributes of the nonlinearity and its applicability at the telecommunications wavelength of 1550nm. It starts with a review of the properties of the gallium crystal, relevant to our explanation of the nonlinear phenomena, and the initial experiments that were carried out and which led to our research. The description of our experiments starts with the presentation of the all-fiberised arrangement that was set up to facilitate the observation of the nonlinearity and measurement of its magnitude and response times. This set-up, which was of a pump-probe configuration, essentially acted as an optical switch, where the signal (probe) was switched on or off accordingly with the application of the control (pump). Using this switch, the maximum induced change in reflectivity was found to be more than 30%. The variation of this figure with temperature and pump power was investigated. Separate experiments utilising nanosecond pulses were carried out in order to assess the dynamics of the nonlinearity. These experiments have proven to be of major importance in the understanding of the origin of the nonlinearity. In order to study the phase response of the nonlinearity a variation of the first experimental arrangement was needed to allow interferometric measurements. Using this new set-up, important information on the dependence of the phase response with temperature and pump power was acquired. Chapter Four also includes a report on some experiments that were carried out to investigate the longevity of gallium mirrors. The chapter closes with a discussion of our current understanding on the physical mechanisms that lie behind this nonlinearity.

Chapter Five is devoted to the application of liquefying gallium mirrors for Q-switching of fibre lasers. Our experiments demonstrated that the nonlinearity of gallium can be used for passive Q-switching of both lasers that require a rather low threshold, and of high-power fibre lasers. Furthermore, the broad spectral characteristics of the nonlinearity make it applicable to an exceptionally wide range of lasers. The chapter opens with a brief review of passively Q-switched lasers that have been reported for the infrared region. Then, an erbium-fibre ring laser is described, which was used initially in order to demonstrate the suitability of gallium for Q-switching. Also, the general pulsing behaviour of the laser for different mirror temperatures and pump powers is explored. The experiments that were performed with higher power lasers and yielded nanosecond-long pulses with μJ energies are given next. Applicability of gallium mirrors to a broad spectral band was demonstrated with lasers that comprised of either erbium- or ytterbium-doped fibre, operating at ~1550nm and ~1050nm respectively, and used a temperature stabilised gallium:glass interface as the Q-switching medium.

Part Two closes with a chapter on further directions that the ongoing research on nonlinear gallium mirrors has followed. Improvement on the technological aspects of the fabrication of the mirrors and the investigation of even faster components of the nonlinearity are discussed.

PART ONE

Chapter One

Actively Mode-Locked Erbium Fibre Ring Laser

Overview: The development and performance of a polarisation maintaining, actively and harmonically mode-locked erbium fibre ring laser (EFRL) operating at ~10GHz are described in this chapter. The interplay between self-phase modulation and group-velocity dispersion in the ring results in intracavity soliton compression of the pulses. Output pulse widths between 1.9 and 4ps are obtained, depending on the operating conditions of the laser. The chapter also includes results on the characterisation of the pulses using the Frequency Resolved Optical Gating (FROG) technique and bit-error-rate (BER) measurements.

1.1. Background study

The physics behind mode-locking is well known [Siegman86]. In general, several longitudinal modes lase together, with a (forced) phase coherence between them, resulting in pulsed output from the system. In active mode-locking, which was preferred here mainly because of the reliability that it offers, modulation of either the amplitude or phase of the optical field in the cavity is applied at a frequency equal to - or a multiple of - the mode spacing. This frequency corresponds to the cavity round trip time. Short optical pulses experience the minimum loss in such cavities and this fact provides the mechanism by which the pulses form. Either acousto-optic or electro-optic modulators can be used for modulating the optical field, but usually $LiNbO_3$ electro-optic modulators are employed in fibre lasers, due to their high operational bandwidth, compactness and low loss [Agrawal95].

A number of reports on actively mode-locked EFRL's are available in the literature. In an early experiment [Kafka89], 4ps nearly transform-limited pulses were produced with a repetition rate of 90MHz. A long length of standard fibre (2km) was introduced in the cavity, giving a large amount of anomalous group-velocity dispersion (GVD). In more recent experiments Nakazawa et. al. reported 2.7ps pulses at 10GHz [Nakazawa94]. 190m of dispersion shifted fibre (DSF) was introduced in the loop to produce suitable conditions for the development of soliton effects and to facilitate pulse compression. The pump power was around 100mW at 1480nm and the time average output power was 1.3mW. Other works reported 3.5ps at 20GHz [Takara92] and 7.6ps at 30GHz [Takada90], whereas in [Pfeiffer94] development of a laser was reported that would operate successfully over a broad tuning range of 50nm. Also, following the introduction of 40GHz electronics, preliminary results of 40GHz mode-locked EFRL's have recently been reported [Ellis99, Yoshida99]. In most of these experiments all fibres and components used were polarisation maintaining (PM) to produce a more environmentally stable cavity. Since the $LiNbO_3$ modulator is a polarisation sensitive device use of a high birefringence loop ensures that all the light incident to the modulator is launched on the correct polarisation axis and does not drift with time due to changes in environmental conditions, which would otherwise affect the mode-locked pulses.

The most common issue that appears in the implementation of actively mode-locked EFRL's is combating the supermode noise, i.e. amplitude fluctuation of the output pulses due to imperfect suppression of the harmonics of the mode-locking frequency [Nakazawa96]. In [Nakazawa96] it was claimed that the combination of a long cavity and a narrow filter should result in a reduction of the pulse width and noise. The concept behind this is that self-phase modulation (SPM) due to a strong optical pulse propagating in the long cavity results in the generation of new frequency components in the wings of the pulse. These new frequency components (pulse chirp) are then removed through the optical filter, resulting in a fast intensity-dependent loss, which increases with increasing pulse intensity. This intensity-dependent loss thus provides a means for pulse amplitude stabilisation. It was shown that the amount of nonlinear phase shift ϕ_{NL} introduced in the cavity should be at least 0.35rads for a significant noise reduction. Furthermore, in later work [Bakhshi97] suggested the ratio of the cavity length L to the soliton period z_0 as a more subjective measure of the amount of nonlinearity needed in the cavity for a good noise performance, since this ratio is independent of the order of the generated soliton pulses. The conclusion of this work was that this ratio should be larger than 0.1, which corresponds to $\phi_{NL} = 0.08$ for first-order solitons [Agrawal95]. It was shown that for a cavity of $L/z_0 \sim 0.4$ the supermode noise could be suppressed by as much as 80dB, which to our knowledge is the best value reported so far. In this work it was also shown that added noise suppression could be obtained by bi-directional pumping of the laser.

Another interesting problem that had to be coped with in all the experiments mentioned above was the production of stable, equal-amplitude pulses over long periods of time. This is because environmental temperature fluctuations result in an alteration of the cavity length and hence, of the mode-locking frequency. Several stabilisation techniques have been employed, which by some means lock the pulse phase to that of the modulating signal. Many of these techniques aim at adjusting the the cavity length (round trip frequency) to be a harmonic of the modulation frequency, by introducing an optical delay line in the cavity. In [Takada90] the signal driving the delay line was controlled by the high-frequency pulsed output. In [Takara95] the cavity length was adjusted, so that the kHz noise due to relaxation oscillations of the intracavity EDFA was minimised, whereas in [Kiyan98] the low-frequency inter-pulse noise signal monitored at the second port of the dual-output electro-optic modulator was minimised, by means of a control loop which drove the delay line.

Alternatively, the cavity modulation frequency can be adjusted to follow the drift in harmonic frequency. In [Nakazawa94] a so-called regenerative mode-locking method was used, according to which the optical signal was detected and passed through a filter of high quality factor tuned to the approximate mode-locking frequency. The resulting signal is then amplified and used directly as the modulation signal to drive the intracavity modulator. Finally, in [Widdowson94] a phase-lock loop (PLL) was employed to lock the pulse phase to that of the signal generator, which in this case is a voltage-controlled oscillator (VCO). The detected pulse and part of the output of the VCO were passed through a mixer; the output of the mixer was low-pass filtered, so that a signal having a frequency equal to the difference of the frequencies of the two initial signals was obtained, and used to control the oscillating frequency of the VCO.

1.2. Implementation

After consideration of the corresponding EFRL designs found in the literature we decided to opt for an all polarisation maintaining ring design using active amplitude modulation with intracavity soliton compression and filtering to obtain ultrashort operation and a PLL to ensure good long-term stability. The cavity layout is shown in fig. 1.1. A special splicer suitable for PM fibres was used to assemble the ring. The $LiNbO_3$ Mach-Zehnder modulator had a 10GHz electrical bandwidth. The active element in the laser was 19m of erbium-doped fibre, pumped at 1480nm by a 120mW pump laser diode. The PM-WDM coupler used also incorporated an isolator to ensure unidirectional operation of the cavity. A 5nm dichroic filter was initially used in the cavity, but due to issues involving its insertion loss and additional filtering due to an etalon effect, it was eventually replaced by an in-line 6nm filter with PM fibre pigtails. Light was coupled out of the cavity using a 30% PM coupler. An isolator at the output port of the coupler prevented any stray light from coming back into the EFRL.

Inclusion of polarisation maintaining dispersion-shifted fibre (PM-DSF) in the cavity was necessary to provide nonlinear soliton compression of the pulses. (Initial experiments with a short, net-zero GVD cavity showed that pulses shorter than 6.2ps at a repetition rate of 10GHz could not be obtained from our cavity). Moreover, as was mentioned earlier on, in order to achieve ultrastable operation the cavity needed to be long, so that amplitude noise suppression would be achieved [Nakazawa96]. The total length of fibre required depends on the amount of dispersion that it introduces. The PM-DSF that was chosen for our ring exhibited dispersion of 2.01ps/(nm·km) at 1550nm on the axis used in the cavity. 485m of this fibre was included in the ring. Since the dispersion of the PM erbium-doped fibre was -10ps/(nm·km), the average dispersion in our cavity at 1550nm is D = 1.73ps/(nm·km).

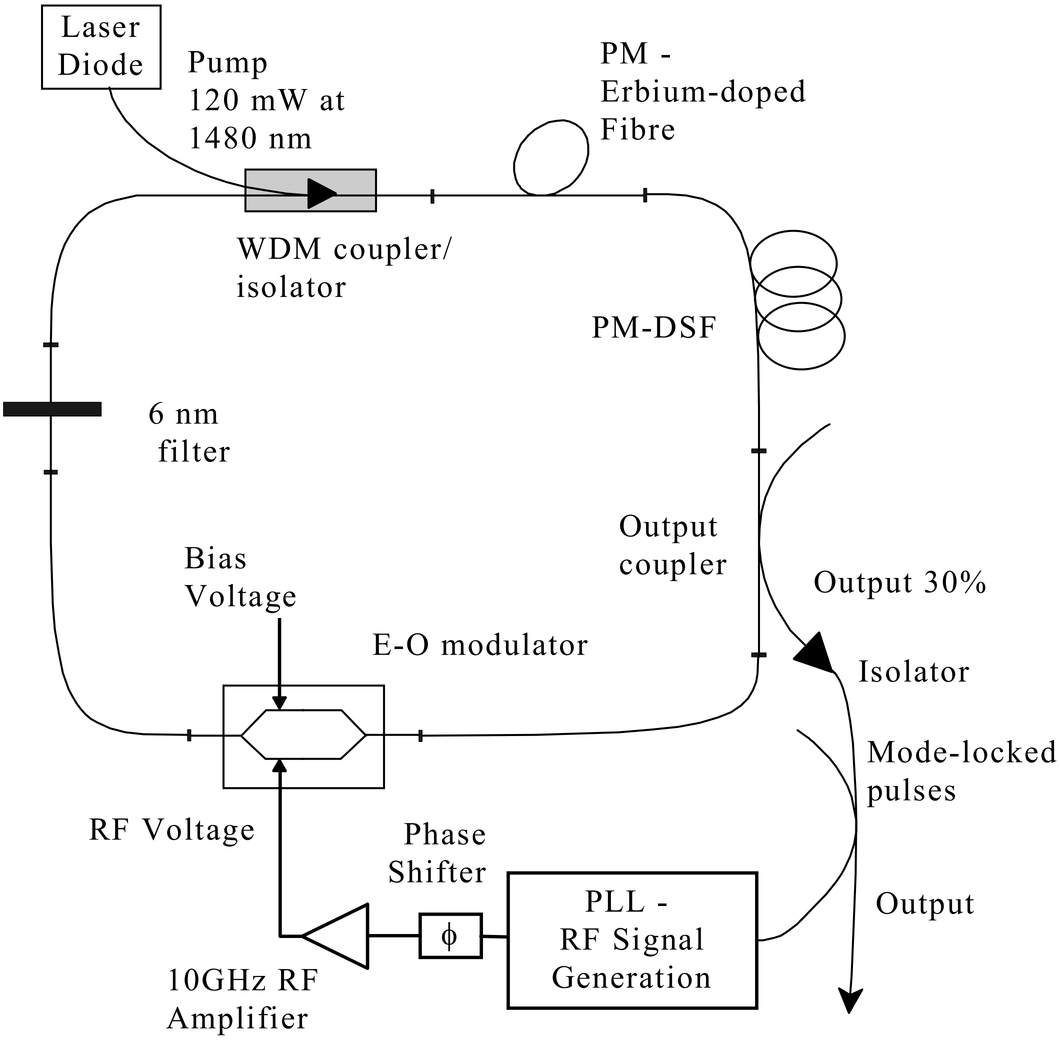

Fig. 1.1 The all polarisation-maintaining Er-doped fibre ring laser

The peak power P_o of a fundamental soliton of width T_{FWHM} is [Agrawal95]

$$P_0 = \frac{3.11 \cdot \lambda^2}{2\pi c\gamma} \frac{|D|}{T_{FWHM}^2}$$

where γ is the nonlinearity coefficient of the fibre. And since the average power P_{av} required for the formation of fundamental soliton pulses of repetition rate f_r is given by

$$P_{av} = 1.13 \cdot f_r P_0 T_{FWHM}$$

it follows that the pulse width is proportional to the ring dispersion and inversely proportional to the average power:

$$T_{FWHM} = \frac{3.51 \cdot \lambda^2 f_r}{2\pi c \gamma} \frac{|D|}{P_{av}} \qquad \text{Eq. 1.1}$$

Calculations showed that for the given dispersion and cavity length the power required to be circulated in the ring in order to meet the condition for noiseless operation suggested in [Nakazawa96] should be at least 12mW, yielding ~3ps output pulses. Furthermore, the soliton period z_0 is given by

$$z_0 = 0.322 \cdot \frac{\pi^2 c}{\lambda^2} \frac{T_{FWHM}^2}{|D|}.$$

Thus, the ratio L/z_0 for our laser was ~$2.27\,T_{FWHM}^{-2}$, where L = 520m the length of the cavity and T_{FWHM} in ps. For T_{FWHM} ~ 2 - 3ps this ratio ranges between 0.57 and 0.25, which complies with the rule suggested in [Bakhshi97], that L/z_0 should be more than 0.1 for good suppression of the supermode noise.

In order to optimise the loss modulation at the $LiNbO_3$ modulator, its full dynamic range was exploited, i.e. its loss was modulated from a minimum (~-5dB) to as high a value as possible (~-30dB). Thus, it was important that the bias voltage was controlled appropriately and the signal levels applied to drive the modulator were of a sufficient strength. The requirement for pulse phase stabilisation became clear in our earliest experiments. Without stabilisation successful mode-locking operation of the laser relative to the drive could be achieved only for a few minutes. Consequently we constructed a phase lock loop, as described in the next section. After the inclusion of the PLL stable operation of the laser over several hours was possible.

Note that the $LiNbO_3$ modulator that was initially included in the cavity (manufactured by E-TEK) was eventually proven unsuitable, due to back reflections within the device which led to noise on the output pulses. The unit was replaced by another device (supplied by Sumitomo). The BER measurements presented in section 1.5.4, as well as the coherence time analyser measurement of fig. 1.9, were carried out using the Sumitomo modulator.

1.2.1. *The Phase Lock Loop*

The PLL was an electronic control circuit responsible for driving a 10GHz VCO at exactly the mode-locking frequency of the EFRL. A block diagram of the PLL is shown in fig. 1.2. The original design belongs to BT labs, and it was slightly modified for our application. 40% of the laser output is detected by a 10GHz detector and fed to the RF input port of a high-frequency mixer. Part of the signal generated by the VCO is fed to the LO port of the mixer. The two signals are mixed and the sum and difference frequency signals are generated. The sum frequency signal is rejected by a 5MHz low-pass filter, leaving the difference frequency signal as a measure of the disagreement in phase between the signal generated by the oscillator and the exact mode-locking frequency. The further away the VCO frequency from one of the mode-locking harmonics, the higher the frequency of the difference signal. This signal vanishes once the PLL is locked. Any small perturbation from the locking frequency generates a slowly alternating signal, the phase of which indicates the direction in

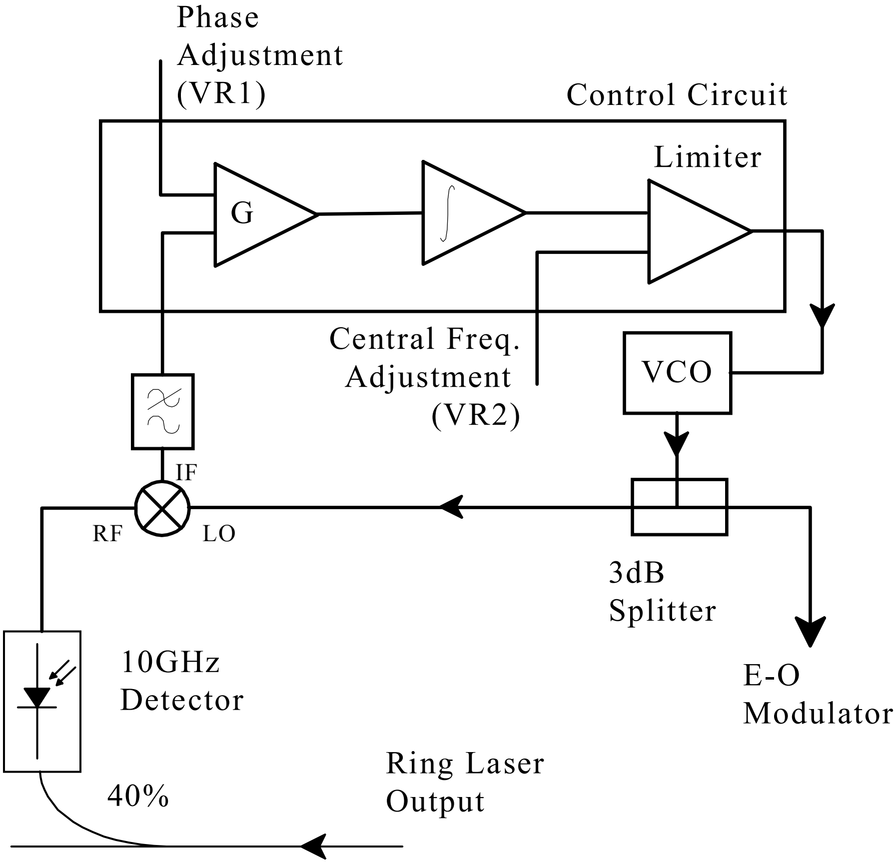

Fig. 1.2 Block diagram of the Phase Lock Loop

frequency towards which the VCO signal should shift. A simple PLL control circuit keeps the system in lock by minimising the difference frequency signal.

A detailed circuit diagram of the electronic control circuit of the PLL is given in Appendix P1.A. Note that the gain values for this circuit are selected so that they suit the voltage levels received at the output of the mixer and the ones required for the VCO. All the components values used are shown in Appendix P1.A.

The circuit, which was of a standard PLL design, can be divided into three parts. The first was a low-noise non-inverting amplification stage for the signal received at the filtered output of the mixer. At this stage also, an externally adjusted voltage, VR1, is added in the amplification process to finely adjust the phase of the generated signal. Even when the PLL is locked, the phases of the two input signals to the RF mixer are not necessarily the same, as phase matching of the generated RF signal to the actual mode-locked signal has to be achieved at the $LiNbO_3$ modulator. This implies that phase-locking can be represented by a constant dc signal at the output of the mixer. Because of the integrating nature of the second stage of the control circuit, the output of the amplification stage for the phase-locking condition has to be zero, and VR1, along with a direct phase adjustment of the VCO signal at the output of the PLL (see fig. 1.1), are used to ensure this.

The second part of the control circuit is an integrator stage, which charges its capacitor to a value dependant on the signal level at its input. While the capacitor is charging, the PLL sought to lock onto the incoming RF signal fed to the mixer. Once this is achieved the input to this stage is zero giving a constant level output. The time constant of the integrator was 0.1ms, giving the PLL a fast dynamic response. A (normally-open) switch is included in this stage to reset the integrator and restart the tracking procedure. Momentary pressing of the switch shorts, and thus discharges the capacitor, which starts charging again once the switch is opened. The last part of the control circuit is a limiter stage, which provides the driving voltage for the VCO and protects it from over-driving. A variable resistor connected to the input of this stage facilitates fine adjustment of the loop gain of the control circuit, so as to optimise its long-term stability. Also, in this stage a second input voltage VR2 is introduced to adjust the central frequency of the VCO around the frequencies of interest.

In order to verify the correct operation of the PLL, the circuit was tested with an external RF tuneable signal generator. It was found that it could easily lock and follow any changes of the input frequency once its initial free-running frequency lays within ~1MHz of the signal generator. This was satisfactory for operation with our EFRL, the mode spacing of which is only 400kHz.

1.3. Polarisation extinction measurements

We characterised all the components used in the EFRL in terms of their polarisation maintaining attributes using a special measuring set-up established in our labs. This was implemented using a combination of λ/2 waveplates, bulk polarisers and analysers (fig. 1.3). Linearly polarised light generated from a 1550nm DFB laser diode was launched into the device under test (DUT) after passing through the waveplate. At the output of the DUT the polariser enabled selection of each of the polarisation axes of the output fibre to be detected. By rotating the waveplate, and optimising the detected signal through the polariser, light was launched onto one of the axes of the PM input fibre of the DUT. Then, optical power at the axis orthogonal to the first axis was measured by suitably rotating the polariser. The polarisation extinction for each of the axes of the DUT was calculated as the ratio of the optical power coming out of the axis on which light was launched, to the optical power received from the second orthogonal axis. The polarisation extinction of the set-up itself was measured to be 32.55dB. Table 1.1 gives a list of the figures measured for

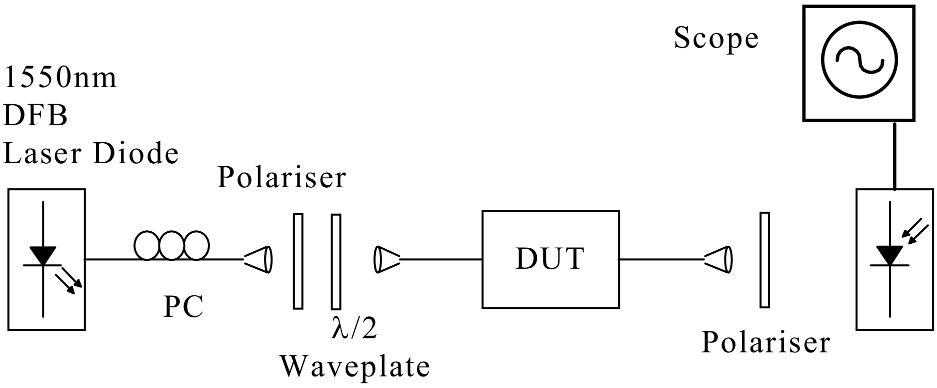

Fig. 1.3 Measurement set-up for the polarisation extinction of PM devices

each of the axes of the components used in the construction of the laser cavity.

Table 1.1 Polarisation extinction figures for the various ring components

Device	*Polarisation Extinction*
WDM coupler	34.95dB
70/30 coupler	37.80dB
LiNbO3 modulator	31.76dB
6nm in-line filter	15.2dB *

* Polarisation extinction of the measuring set-up for this measurement was 23.3dB

1.4. Dispersion measurements

One of the most critical aspects of the ring design was the inclusion of the PM-DSF. It was within the length of the DSF where the interplay between nonlinear and dispersive effects took place resulting in the formation of solitons, the narrowing of the pulses and the consequent reduction in supermode noise.

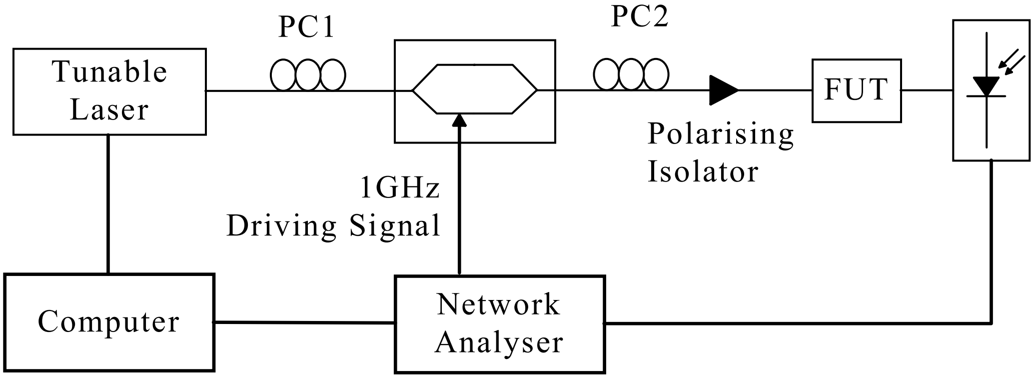

Fig. 1.4 Measurement set-up for the dispersion of PM fibres

However, PM-DSF fibres are not commercially available. A variety of bow-tie fibres of unknown dispersion, but theoretically suitable numerical aperture (NA) and cut-off wavelength, were made available to us by Fibercore plc for testing and selection. In order to characterise their dispersion the set-up shown in fig. 1.4 was implemented, which is a variation of the in-house set-up established to characterise the dispersive characteristics of gratings [Barcelos96]. The idea is based on the phase-shift technique [Costa82], which determines the delay that a modulated optical signal experiences, when it propagates along a dispersive medium. The set-up consisted of a single-frequency laser, tuneable between 1530 and 1570nm, the output of which was modulated at 1GHz by a $LiNbO_3$ intensity modulator. The first polarisation controller (PC1) was used to align the polarisation of the laser light to the correct axis of the modulator, whereas the second one (PC2) aligned the polarisation of the light output from the modulator to the axis of the polarising isolator, the output of which was PM-spliced to one end of the fibre under test (FUT). This allowed for an independent measurement of the dispersion for each of the two axes of the FUT. The modulating signal was provided by a network analyser and the detected signal was fed back to it, so that the delay of the detected signal relative to the input could be measured as a function of wavelength. The network analyser and tuneable laser were connected to a computer, which scanned the wavelength range and recorded the delay $\tau(\lambda)$. Finally, a graph of time delay versus wavelength was drawn. The slope of this graph gives the dispersion for each wavelength D_λ, as $D_\lambda = \frac{1}{L} \cdot \frac{d\tau(\lambda)}{d\lambda}$, where L is the length of the FUT.

Table 1.2 Zero-dispersion wavelength and dispersion at 1550nm for each of the polarisation axes of the PM fibres tested

Fibre Type	***Axis A***		***Axis B***	
	λ_o	***D*** D_{1550}	λ_o	D_{1550}
YD582	**1531.6nm**	**1.25ps/(nm·km)**	**1521.7nm**	**2.01ps/(nm·km)**
YD840	1611.5nm	-4.00ps/(nm·km)	1573.9nm	-2.19ps/(nm·km)
YD792	1440.5nm	6.98ps/(nm·km)	1442.5nm	7.35ps/(nm·km)
YD423	1395nm	9.15ps/(nm·km)	1389nm	9.19ps/(nm·km)

The data collected for the various PM-fibres is tabulated above. Fibre YD582 was chosen for our laser. It exhibited a dispersion of 2.01ps/(nm·km) at 1550nm and second order dispersion of 0.071ps/(nm^2·km) for the axis used in the cavity (axis B). The second axis of the fibre (axis A) had a dispersion of 1.25ps/(nm·km) at 1550nm and second order dispersion of 0.068ps/(nm^2·km). Fig. 1.5 shows the time delay versus wavelength graph for the fibre's B axis.

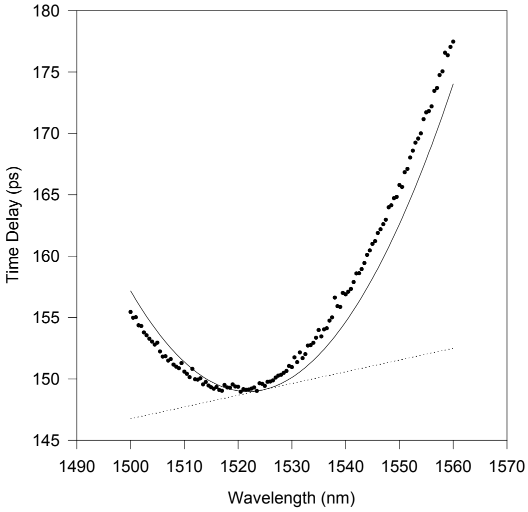

Fig. 1.5 Measurement of the time delay vs. wavelength for the polarisation axis of YD582 used in the ring (dots); dashed line represents the contribution of the measuring set-up to the measured dispersion (i.e. patchcords etc.); the corrected measurement (taking into account the system's inherent dispersion) is given with the solid line

1.5. Laser performance

Mode-locked operation requires that the driving frequency matches exactly a harmonic of the fundamental frequency of the laser; once this requirement was satisfied, stable mode-locking could be obtained giving around 2ps almost transform limited soliton pulses with an average output power of 4.6dBm (fig. 1.6). Under normal operation, with the PLL driving the RF oscillator (preferably in a temperature-stabilised environment) pulsing could be maintained for several hours without significant degradation of the laser performance. The operation wavelength could be tuned between 1546 and 1557nm. The electrical spectrum sidebands due to relaxation oscillations were suppressed by as much as 65 - 70dB, while harmonic sidebands suppression exceeded 60dB. Pulse jitter was also greatly limited.

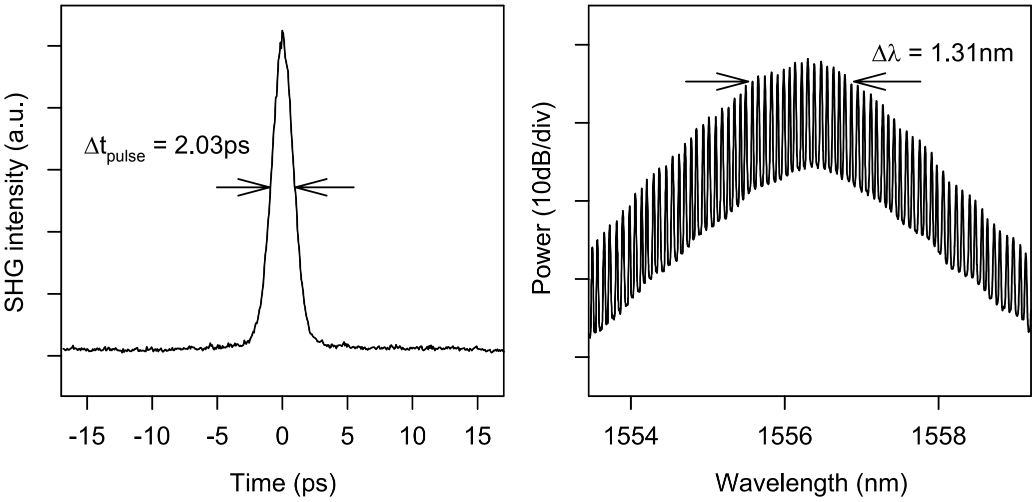

(a) (b)

Fig. 1.6 (a) Typical autocorrelation trace of the pulses and (b) their corresponding optical spectrum (resolution 25pm)

The laser characteristics presented below correspond to operation at 1557nm. The performance of the laser at other wavelengths was not significantly different and hence is not shown.

1.5.1. *General characteristics*

A laser characteristic for typical operating conditions is given in fig. 1.7, which shows a low threshold of 20mW and a quantum slope efficiency of 11.5%. In this plot the output power levels correspond to the power received just after the isolator at the 30% port of the output coupler. A typical autocorrelation trace of the output pulses for pump power 67.5mW is given in fig. 1.6a. The full width at half maximum of the pulses is 2.03ps. The corresponding optical spectrum is shown in fig. 1.6b, showing a 3dB bandwidth of 1.31nm. This corresponds to a time-bandwidth product of 0.330, indicating that the output pulses were almost transform-limited solitons. The average power at the output of the ring was 6.8dBm, leaving 4.6dBm after the power splitting for the PLL. Intracavity soliton shaping of the pulses was further verified by measuring the dependence of the pulse width on pump power (see eq. 1.1). As pump power varied from ~40 to ~70mW, the pulse width changed accordingly from ~4 to ~2ps. This dependance was more closely investigated by FROG characterisation of

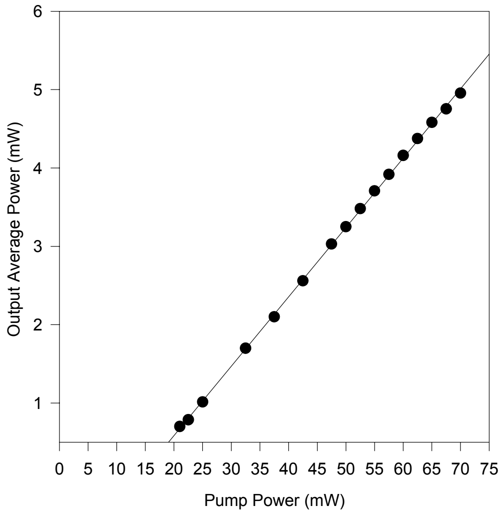

Fig. 1.7 Laser output characteristic

the pulses as described in section 1.5.2. Careful adjustment of the phase control of the PLL (VR1) and the bias voltage V_b of the $LiNbO_3$ modulator was required in order to obtain pulses of maximum stability and minimum noise and chirp.

For stable mode-locking of the laser the pump power should be kept below 70mW. At higher power levels the pulse quality starts to degrade. The autocorrelation trace of the pulse developed shoulders (fig. 1.8) and the pulses became more chirped. Also in general, in these cases locking of the PLL could not be maintained for a long time. It has been suggested elsewhere that this pulse deformation should result from departure of the soliton pulses from the N = 1 condition (i.e. first order solitons), due to the increase in the intracavity pump power [Bakhshi97, Yoshida99]. It is also to be noted that long-term operation could not be maintained for pump powers less than ~45mW, as supermode noise would build up and stable oscillation was not possible.

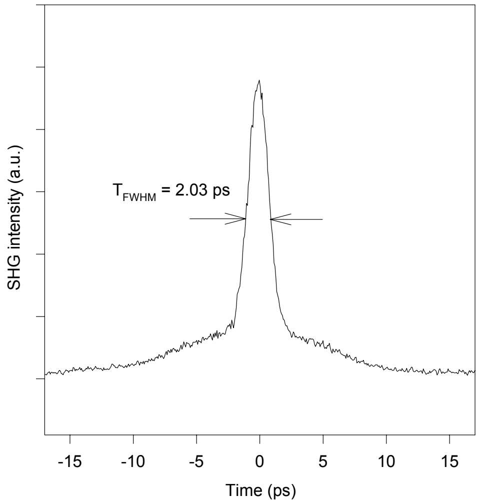

Fig. 1.8 Autocorrelation trace of the pulses for a pump power of 75mW exhibiting pronounced pedestal formation

In order to assess the interpulse noise performance of the laser, a Coherence Time Analyser (CTA) was used. The CTA was developed at BT labs, and the measurement took place in collaboration with them. The CTA was a fiberised, autocorrelation-type measuring set-up, benefiting in terms of sensitivity from the inclusion of a lock-in amplifier. It consisted of a fibre Mach-Zehnder interferometer with a variable optical delay line in one path. The optical delay line length, which could be controlled using a piezoelectric transducer, was modulated at a low frequency (~1kHz), imposing a phase modulation on the signal. The output signal was then detected with a low frequency detector and measured with the lock-in amplifier, which enhanced the dynamic range of the measurement. The measured value corresponded to the cross-correlation value of the signals in the two paths for the given time delay. The delay line was slightly offset for the next measurement, until an adequate set of measurements was taken.

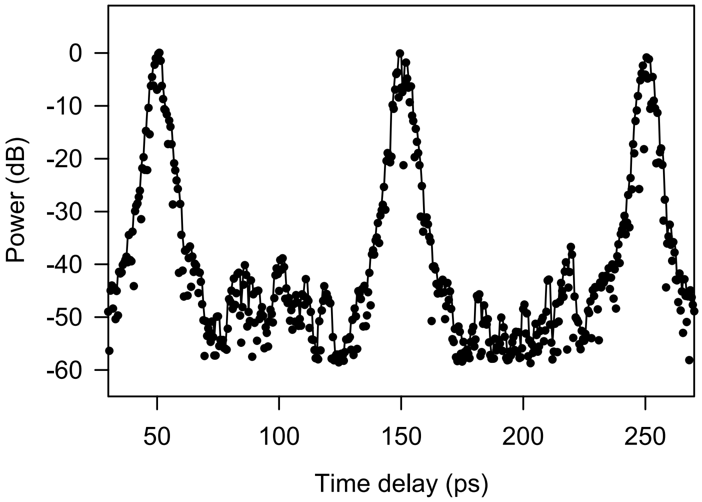

Fig. 1.9 CTA measurement of the EFRL pulses

The CTA measurement of the laser pulses is shown in fig. 1.9. The noise on this measurement should be mainly attributed to the open environment that the fibre interferometer was exposed to at the time of the measurement. The figure suggests the existence of some sub-pulses between the main 10GHz pulses. The peak power of these sub-pulses is ~40dB lower than that of the main pulses. The sub-pulses originate from light coupled on the second polarisation axis of the PM fibres in the ring, due to the imperfect, although reasonable (~20dB), polarisation extinction of the ring. Light on the second polarisation axis travels at a different velocity to that on the first, and hence the sub-pulses appear temporally offset from the main pulses. The destructive interference effects of these sub-pulses when we multiplex the 10GHz optical pulse train to 80GHz will be discussed in section 1.5.4.

Mode-locking operation of the EFRL was achieved between 1546.3 and 1557.4nm. Outside these limits mode-locking cannot be maintained for more than a few minutes, and the pulses are wider, exhibiting excessive amplitude noise and a temporally unstable spectrum.

1.5.2. *FROG characterisation of the pulses*

The bandwidth limitations of state-of-the-art electronics and photodetectors limit the characterisation of the exact shape of optical pulses to pulses with durations >10ps. The conventional approach for the characterisation of short and ultrashort optical pulses combines a crude measure of the spectral bandwidth and the width of the autocorrelation function. These independent measurements of the pulses in the frequency and time domain allow then the estimation of the time-bandwidth product. Although this indirect method has long been considered adequate for the evaluation of pulses, it does not quantify the level of chirp in an unambiguous way. The development of ultrashort pulsed laser technology has demanded novel methods for the complete characterisation of the electric field, i.e. the retrieval of both intensity and phase information.

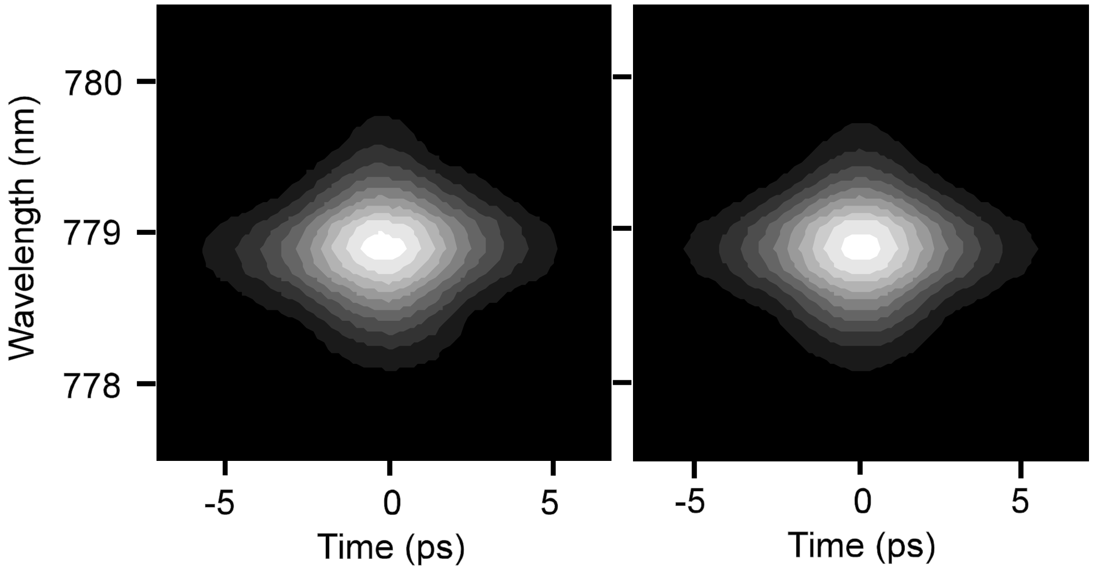

(a) (b)

Fig. 1.10 (a) Typical measured and (b) retrieved spectrograms of the FROG measurements, showing a good agreement between the two

Of the several methods that have been suggested for the complete characterisation of optical pulses (see e.g. [Iaconis98, Debeau98]) one of the most widely known is frequency-resolved optical gating (FROG) [Trebino97]. FROG is based on a spectrally resolved autocorrelation of the pulses. In second-harmonic generation FROG (SHG FROG), which was used here, the pulsed signal is mixed with its delayed replica in a $\chi^{(2)}$ nonlinear crystal. The second harmonic autocorrelation signal is spectrally resolved using a diffraction grating and a detector array. The delay of one of the two mixed signals is varied appropriately to cover the full length of the pulse, producing thereby at the output a spectrogram of the pulses as a function of the time delay. Commercially available iterative algorithms can be used to extract the exact pulse shape from the measured spectrogram.

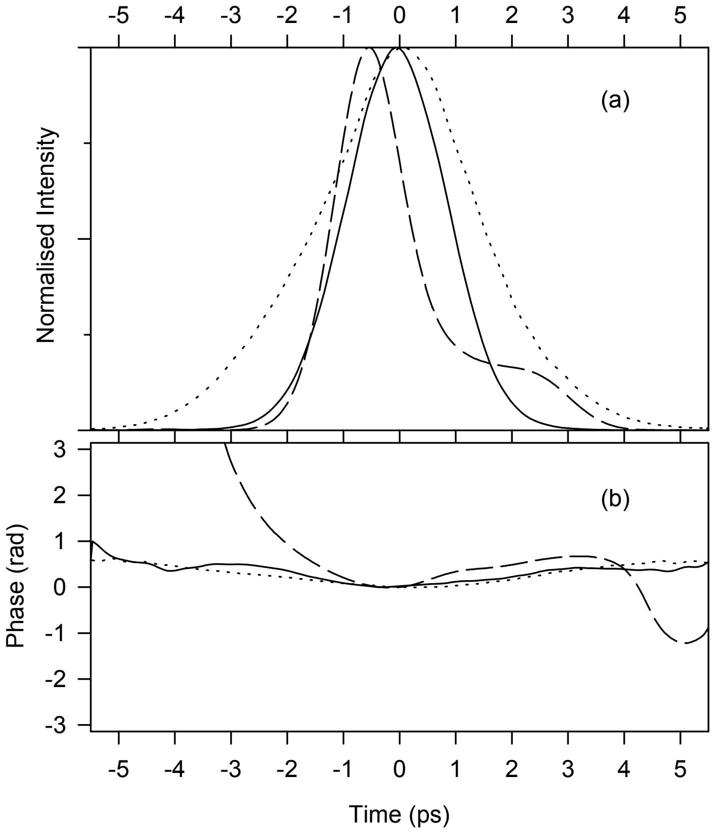

Fig. 1.11 Exact pulse shapes of the EFRL (a) and their corresponding optical phases (b) as measured with the FROG set-up. The laser pump powers are: 45mW (dotted curves), 60mW (solid curves) and 85mW (dashed curves)

The measurements we performed with the pulses from the EFRL, apart from providing invaluable information about the pulse characteristics, constituted the first demonstration that FROG can be successfully used to characterise such low-energy high repetition rate pulses suitable for telecommunications applications. In our experiment, the pulses were amplified to an average power of ~50mW, using an erbium-ytterbium amplifier, before being fed to the FROG set-up. Thus, the pulse energy was ~5pJ, significantly lower than normally used in similar measurements in the past (typically >1nJ [Kwok98]).

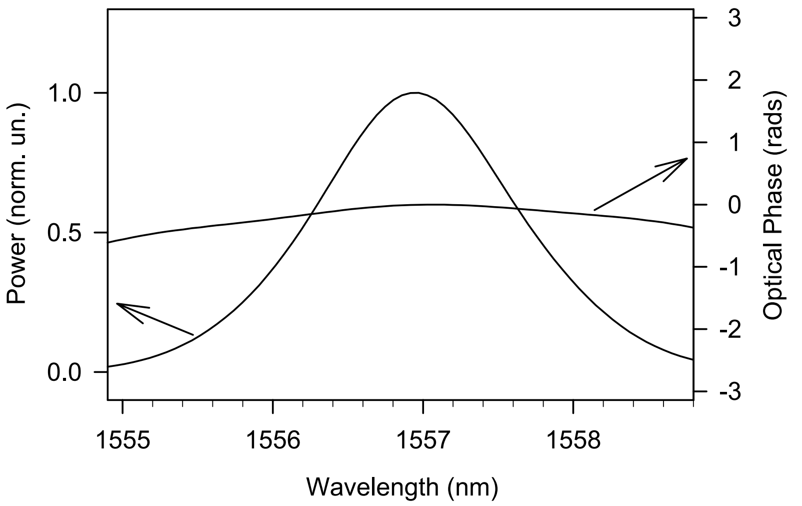

Fig. 1.12 Spectral response and optical phase of the EFRL pulses as measured with the FROG set-up (pump power 60mW)

A typical spectrogram obtained from the FROG measurement along with its retrieved version after processing of the data is shown in fig. 1.10. The laser pulses were characterised for a variety of laser pump powers. The measurements showed that as long as pump power remained lower than 65 - 70mW, the time-bandwidth product of the pulses was close to the value for transform-limited solitons, and the chirp across the pulse duration was insignificant (fig. 1.11). Fig. 1.12 shows the spectral response of the pulses obtained at a pump power of 65mW (the temporal shape of these pulses is drawn with a solid line in fig. 1.11). The asymmetry on the optical phase of the spectrum in fig. 1.12 can be attributed to the contribution of the dispersion of the amplifier at the input of the FROG system (~0.15ps/nm). At higher pump power levels than ~70mW the pulses were no longer chirp-free. As shown in fig. 1.11, they developed some pedestal on the trailing edge and the chirp became more severe (compare to fig. 1.8). It was also clearly verified with these measurements, that the pulse width decreased with increasing pump power (as previously observed from the autocorrelation traces) - a typical characteristic of soliton pulses. This dependence is given in fig. 1.13, where it is shown to follow closely the trend determined by eq. 1.1.

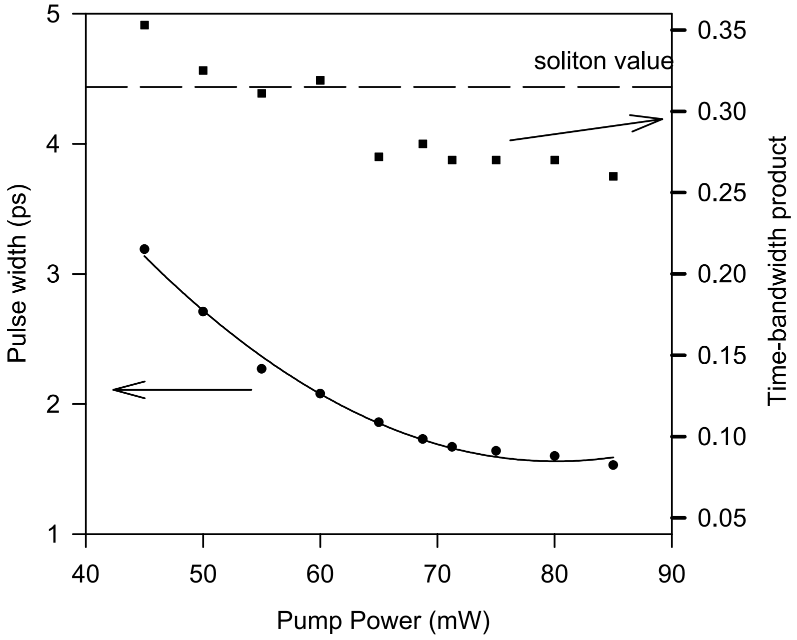

Fig. 1.13 Variation of the time-bandwidth product and the width of the EFRL pulses with pump power

1.5.3. ***Supermode noise and temporal jitter measurements***

A pulse sequence of repetition rate f_r is represented in the frequency domain by components at f_r and its multiples. A mode-locked laser cavity has a fundamental frequency of $f_m = \frac{c}{n \cdot L}$, where n is the refractive index of the fibre and L the length of the cavity. In harmonic mode-locking, all multiples of f_m except for f_r and its multiples are in the ideal case fully suppressed. The effect of supermode noise is the incomplete suppression of these multiples of f_m to the spectral profile, resulting in slowly fluctuating amplitude noise.

Supermodes in our laser were separated by ~400kHz. A typical spectral profile around the locking frequency f_r ~ 10GHz is shown in fig. 1.14, where the supermodes were suppressed almost as far down as the noise level of our detection system, ~58dB below the component at f_r. Contribution to the suppression of the supermode noise to such an extent was largely due to the long cavity, soliton formation and optical filtering, as has been mentioned before. In addition, we found that the amplifier length also played a critical role in the supermode level suppression. In particular, the supermode noise could not be reduced to less than 50 dB, when a longer length of erbium-doped fibre was included in the ring (25m instead of 19m).

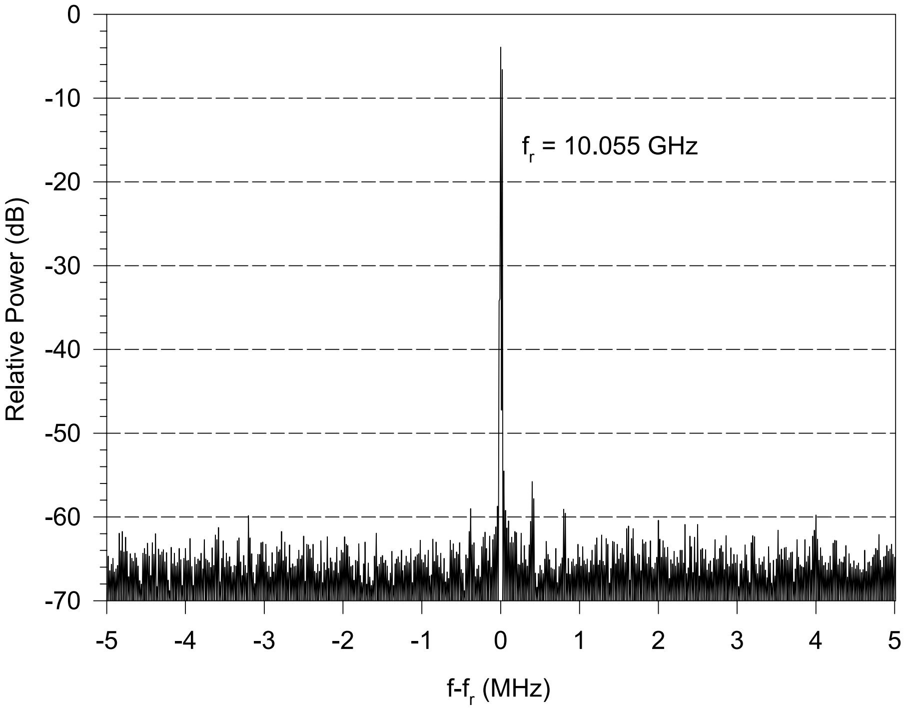

Fig. 1.14 RF spectrum around the mode-locking frequency showing supermode suppression of 58dB

In addition, the kilohertz component of the noise due to relaxation oscillations of the erbium-doped fibre was suppressed by more than 65 - 70dB, exceeding our high-resolution detection sensitivity.

The electrical spectrum of a mode-locked laser can also reveal useful information about fluctuations of the pulses position in time. Pulse jitter measurements were performed after the method described in [Linde86]. A brief description of this method is given in Appendix P1.B.

This method requires analysis of several frequency components of the pulsed signal, that is the components at several multiples nf_r of the pulse repetition rate f_r. In order to determine the temporal jitter of the pulses of our laser, the frequency components at just 10, 20 and 30GHz were analysed (i.e. $n = 1$, 2 and 3), as we were restricted from using higher harmonics by detection bandwidth limitations. The resolution bandwidths used for determination of the low and high frequency components were respectively Δf_{res} = 100Hz and $\Delta f'_{res}$ = 1kHz. The measurements showed negligible amplitude noise, and a low frequency jitter component of Δt = 0.86ps, with a time constant of 0.4ms. There is also a very small high frequency jitter $\Delta t'$ ~ 0.12ps with a time constant of ~32μs.

1.5.4. *Bit-error-rate measurements*

The ultimate test, as far as the noise performance of the laser was concerned, came with a series of BER measurements. The measurements were carried out in collaboration with BT labs. They consisted of back-to-back measurements of the laser pulses, as well as BER measurements of multiplexed 40GHz and 80GHz signals. In all cases the pulses were modulated using a $(2^{31}-1)$-bit-long pseudorandom sequence. The results of the BER tests are presented in fig. 1.15. The back-to-back measurements of the 10GHz laser pulses showed exceptional noise performance. Bit error rates less than $\sim 2\cdot 10^{-13}$ were achieved, and no noise floor was detected. The error-free operation of -18.5dBm at 10Gbit/s is essentially state-of-the-art.

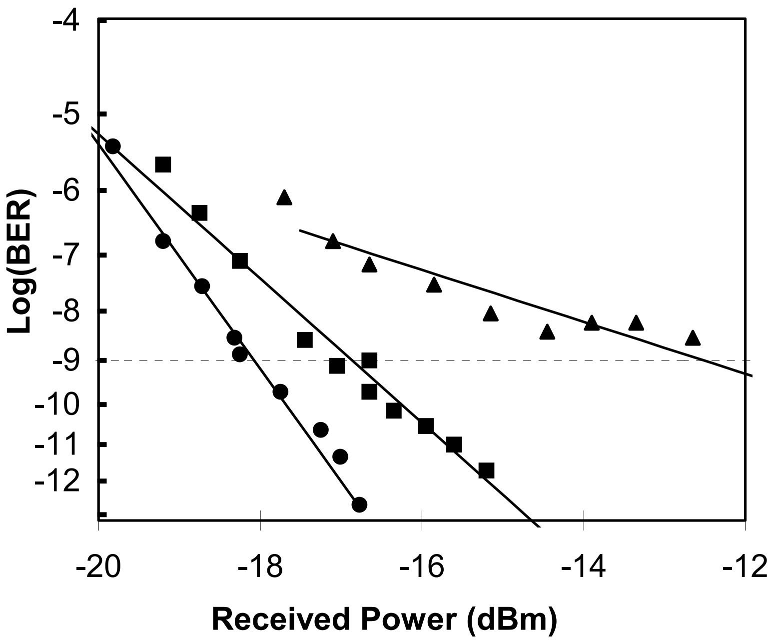

Fig. 1.15 BER measurements of the EFRL pulses (circles), 40GHz (squares) and 80GHz (triangles) multiplexed signals

The multiplexers used to form the 40 and 80GHz signals consisted of fibre delay lines. In both cases, the original 10GHz signal was modulated before being coupled onto the multiplexer. The optical length of the delay lines was much longer than the duration of the sequence itself, ensuring that any adjacent bits comprising the recombined 40GHz or 80GHz signal did not originate from the same pulse. This is important for such a test, the aim of which is to assess the immunity of the bit stream to intersymbol interference caused by adjacent bits of random values.

A power penalty of ~1.5dB arises at the 40GHz multiplexing of the signal. Some of this penalty should originate from the electro-absorption modulator used at the receiver for the demultiplexing of the signal back to 10GHz. Nevertheless, error-free operation is still readily achievable. On the other hand, the 80GHz signal experienced the most severe noise penalty. This is attributed to the contribution of the sub-pulses that were first observed in fig. 1.9. These sub-pulses were remainders of the original 10GHz pulse streams, and acted as (small) amplitude noise within the time frame of the multiplexed pulses, interfering directly with them. Their contribution is more evident on the 80GHz signal, where the pulses were spaced more closely to each other. If such a high multiplexing factor is necessary, then some method of reducing the effect of these sub-pulses has to be employed before multiplexing takes place (e.g. rejection using a polariser, since the sub-pulses are in an orthogonal polarisation axis than the main 10GHz pulses).

1.6. Conclusions

An actively and harmonically mode-locked fibre ring laser was constructed to provide short pulses at a high repetition rate. A long section of DSF was included, to ensure generation of short soliton pulses with low noise, and only polarisation maintaining components and fibres were used for greater environmental stability. Locking over long periods of time was ensured by an electronic phase lock loop circuit, which locked the driving frequency of the electro-optic modulator to an exact harmonic of the mode-locking frequency of the ring.

The laser was tuneable around 1550nm, giving almost transform-limited soliton pulses of pulse width ~2ps (which varies slightly with the pump power, as directly shown by the FROG measurements). Laser supermodes were suppressed to more than

60dB, and the pulses exhibited very small timing jitter. Error-free operation for long periods of time was verified with BER measurements. This laser constitutes a state-of-the-art source short pulse suitable for telecommunications applications. During the course of this work, it was used in applications involving pulse manipulation employing fibre Bragg gratings. These applications will be described in the following chapter.

Chapter Two

Coherent pulse manipulation using fibre Bragg gratings

Overview: The relation that exists between the spatial modulation of the refractive index of a fibre Bragg grating (FBG) and its temporal response, is used to control the shape and attributes of short pulses. Three individual pulse shaping applications are investigated: encoding and decoding of pulse sequences; reshaping of solitons into square pulses; and coherent pulse multiplication.

2.1 Shaping of short optical pulses

The tremendous progress in ultrafast laser technology in recent years has made it straightforward to generate picosecond and femtosecond pulses. Moreover, the sources are getting more and more powerful and ever more compact and less complicated to use. Lasers typically generate pulses with sech or Gaussian pulse shapes, which are not ideal for many applications. Consequently, significant research has focused on the development of techniques that allow the generation and processing of pulses with precisely controlled shapes. In general, the temporal shape of a pulse can be altered by appropriately filtering the amplitude and phase of its electric field in the frequency domain. In the most widely known and used shaping technique, filtering of the input pulse takes place in a Fourier optical 4f set-up [Weiner98]. According to this method, the frequency components of a short pulse are spatially dispersed using bulk gratings and filtered by means of amplitude and phase masks. Microlithographically fabricated spatial masks [Weiner88], segmented liquid crystal modulators [Weiner92], or acousto-optic modulators [Fetterman98] have been used as spatial filters. Other researchers have also demonstrated certain pulse shaping applications making use of the nonlinear properties of optical fibres [Halas87, Kishore99].

The considerable progress in the fabrication of FBG's raises the possibility of using such structures for novel pulse shaping applications. FBG's can be viewed as linear spectral filters, capable in principle of transforming the amplitude and phase of an incoming waveform to essentially "any" desired form. For example, based on such a concept Muriel et. al. have recently suggested the use of linearly chirped FBG's to perform real-time optical Fourier transforms, based on the duality that exists between spatial diffraction and temporal dispersion [Muriel99]. However, the requirements on the amount and linearity of the imposed chirp are quite stringent, making the fabrication of such a grating quite challenging. As far as we know, the practicality of this particular technique has not yet been experimentally verified.

In this chapter we investigate the possibility of performing pulse shaping using superstructured FBG's as passive optical spectral filters of almost arbitrary response. Superstructured FBG's represent a powerful and flexible tool, offering all the benefits of a fully fiberised system, i.e. compactness, ready integration into fibre systems and minimal coupling losses. The term superstructured FBG's generally refers to FBG's whose refractive index profile is not uniform in amplitude and/or phase along their length. The technique requires weakly written FBG's, i.e. FBG's in which the relative changes of its refractive index are small enough to allow the incident light to penetrate its whole length without significant attenuation. Thus, for such gratings, the entire structure contributes to the reflected light. In this case, the following two observations are valid: Firstly, the wavevector response $F(\kappa)$ of a (weak) fibre grating is given by the Fourier transform of the spatial refractive index modulation profile $A(x)$ used to write the grating [Hill97, Eggleton94]

$$F(\kappa) = \frac{1}{2\pi} \int_{-\infty}^{+\infty} A(x) e^{j\kappa x} dx$$

where κ is the wavevector, which is proportional to the frequency ω.

The second observation is that the impulse response $h(t)$ of a fibre grating is given by the inverse Fourier transform of its frequency response $H(\omega)$

$$h(t) = \int_{-\infty}^{+\infty} H(\omega) e^{-j\omega t} d\omega$$

It therefore follows that the impulse response *h(t)* of a weak FBG is a pulse of the same temporal profile as the spatial modulation profile *A(x*) of the grating. In other words, after reflection from a weak FBG, a short pulse is transformed to a pattern of the shape of the sampling function used to write the grating. Extending this, we conclude that the reflected signal *y(t)* is the convolution of the incident signal *x(t)* with *h(t)*

$$y(t) = x(t) * h(t) \qquad \text{Eq. 2.1}$$

or, in the frequency domain, the reflected signal *Y(ω)* is the product of the incident signal *X(ω)* with *H(ω)*

$$Y(\omega) = X(\omega)H(\omega) \qquad \text{Eq. 2.2}$$

where *Y(ω)* and *X(ω)* imply the Fourier transforms of *y(t)* and *x(t)* respectively. Thus, a FBG can be designed, such that upon reflection, a known signal *x(t)* is reshaped into the desired *y(t)*.

We note that the requirement of full penetration of the light in the FBG structure, potentially limits the strength of the FBG's. The maximum permissible change in the refractive index of the grating Δn_{eff}, depends on the overall FBG length and the shape of the superstructure function itself. The gratings used in the experiments presented here had an overall reflectivity of <10%, which is considered acceptable for the argument presented above to hold. However, recent research [Feced99] has shown that these grating strength limits can be overcome by adopting more advanced design techniques to establish the required superstructure function, rather than the simple Fourier analysis used herein.

In essence, the same principle was employed earlier in [Emplit97], where it was demonstrated that bright solitons could be transformed into dark solitons, after reflection from a FBG with a phase shift in the middle of the structure. Also, in [Geiger98] it was demonstrated that a uniform FBG can form a matched filter for rectangular pulses whose duration corresponds to the optical length of the FBG. In the experiments reported herein, we generalise the concept and demonstrate the feasibility of more complicated signal processing functions, by employing more sophisticated structures.

The implementation of such structures requires excellent control over the imposed amplitude and phase of the modulated refractive index of the grating. Fabrication of the FBG's reported in this chapter was made possible by adopting a grating plane by grating plane writing technique, which relies on moving a fibre relative to a fixed phase mask. The main concept behind this technique, which is described best in [Ibsen99], is that the UV exposure on the photosensitive fibre occurs always under the same part of the phase mask, while any amplitude or phase modulation is imposed by reducing the incident UV flux or dephasing the fibre relative to the phase mask. Thus, any errors in the writing process or imperfections in the phase mask are averaged out, as the fibre is exposed to different parts of the mask over many times during the writing process.

In the following sections three different applications are presented, through which the viability of the approach is explored. The aim of the analysis is twofold; (a) to present the particular aspects of each application, and (b) to emphasise the significance that such structures can have in future telecommunications networks. The first application concerns an elementary pulse encoder and its subsequent decoder, suitable for optical code-division multiple access (OCDMA) systems. The second experiment describes a pulse shaper that transforms 2.5ps soliton pulses into 20ps square pulses, and the third application relates to a pulse multiplier, that coherently changes the repetition rate of the 10GHz EFRL to 40GHz without altering the individual characteristics of the pulses.

2.2 OCDMA encoding/decoding

Code division multiple access (CDMA) is a broadcast transmission scheme widely used in satellite and mobile communications. In a CDMA system a separate code of a certain length is assigned to the data bits of each user. All users use the same frequency (wavelength) allocation at the same time, and the required signal is separated from the unwanted ones by knowledge of its code. Encoding can be performed either in the frequency domain (frequency-hopping CDMA) or in the time domain (direct-sequence CDMA). In the latter scheme every data symbol is represented by an encoded sequence consisting of n bits (or chips, as they are more commonly referred to, to differentiate them from the data bits), and the total duration of the sequence is equal to the time allocated for each symbol. Thus, the spectrum occupied by the transmitted signal is broadened by n times; because of this, CDMA is referred to as a spread spectrum technique and the code as a spreading sequence. The codes used in CDMA have to be pseudorandom sequences, such that minimum correlation exists between them, thereby allowing the required signal to be unambiguously detected even in the presence of a number of other signals. Detection is performed by using a matched filter, that is a filter matched to give maximal response to a signal pulse of known waveshape or, more precisely, a filter which has an impulse response which is the time reverse of the matched signal. Cross-correlation of a signal with its matched filter results in an output which maximises at one instant in time (the sampling instant).

Although CDMA might seem unattractive because it requires much more bandwidth than other schemes, it has to be appreciated that this spectrum is used simultaneously by all users. Furthermore, because of the nature of the encoding, CDMA is more immune to interference from other signals transmitted at the same time, and, unlike TDMA, each receiver has to be synchronised only to its transmitter, which is at a far lower frequency than the chip rate. Also, CDMA offers advantages in terms of reducing the impact of nonlinearities since the signal energy is distributed over the whole duration of one bit period, thus reducing the peak powers. All these reasons make CDMA an interesting alternative to other multiple access schemes even for optical communication systems, and therefore its study has attracted a lot of recent interest.

The fundamental issue for the implementation of an OCDMA system is that of waveform synthesis and recognition. The most interesting schemes that have been suggested for all-optical pattern generation and recognition are summarised below. In [Wey97] dynamic gratings in erbium-doped fibre were suggested for this purpose. The code sequence was dynamically written by modulating the gain of a doped fibre. This was achieved in a coherent manner, by launching a reference pulse at one end of the 980nm pumped fibre, and an electro-optically modulated sequence at the other end. The resulting gain grating was read from the fibre within the excited state lifetime of the erbium ions (~1ms) by launching a "readout pulse". Similarly pattern recognition was performed by launching an unknown pattern into the fibre and receiving its cross-correlation with the response of a stored gain grating at the system output. A similar idea was used in [Yu99], where a semiconductor optical amplifier consisting of several segments that were independently biased above or below threshold represented the desired code. A single control pulse encoded the corresponding spatial pattern in the time domain on a counter-propagating beam by sequential saturation of the gain or absorption in the segmented amplifier.

Other studies have focused on the implementation of OCDMA systems as a whole rather than just the encoding/decoding aspect. The most common approach is the use of parallel optical delay lines for spreading the data bits and reconstituting the encoded sequence [Pruncal86, Pendock95]. Here the main issues that arise are those of correctly tuning the individual delays and compensation of the changes in fibre lengths due to environmental conditions. These were overcome in [Lam98] by employing a multistage Mach-Zehnder interferometer chain fabricated on a silica planar waveguide, with balanced detection to enhance the data recovery. Alternative OCDMA designs have also been suggested: in [Tsuda99] the encoder and decoder consisted of a combination of arrayed waveguide gratings with a phase filter; in [Wada99] an integrated planar lightwave circuit that employed tuneable taps, optical phase shifters, delay lines and a combiner was used to produce bipolar codes (where the chip encoding is 1 and -1 rather than 1 and 0); and both [Chang98] and [Dennis99] made use of the previously described 4f pulse shaping set-up with a suitably designed spatial amplitude mask.

It is also worth mentioning three more encoding/decoding schemes that have been reported recently, and employ FBG's. In [Hunter99], an array of FBG's having the same central wavelength, caused multiple reflections from a pulsed narrowband source. The temporal delay between the distinct pulses of the generated pattern corresponded to the spatial distribution of the FBG's. The benefit of this technique is that the FBG's could be strain-tuned, shifting the Bragg wavelength away from the operating wavelength, allowing dynamically control of the reflected pattern. In [Fathallah99] it was suggested that multiple gratings of different wavelengths could be written into a single piece of fibre, thereby slicing the wide spectrum of an optical pulse into different time slots. The spectrally encoded pulse could then be re-composed at the receiver by using an identical array of gratings illuminated from the opposite direction. In order to achieve a perfect match for the encoding and decoding gratings, their exact wavelengths should be strain tuned in both the transmitter and the receiver side. Finally, in [Chen99] it was proposed that chirped Moiré fibre gratings can be employed to perform simultaneous encoding in both wavelength and time. A Moiré grating consists of the superposition of two gratings of different (but closely spaced Bragg wavelengths). Consequently, the grating pattern develops fringes - where the phase of the grating changes by π - thereby producing narrow stop bands in the reflectivity spectral response. Thus, the spectral response of the grating is divided into segments (the number of which depends on the choice of the beating Bragg wavelengths), and each segment comprises a chip of the spectral code. As before, decoding can be performed by using an identical grating illuminated from the opposite direction.

In our experiment, pulse encoding and decoding was performed using single superstructured gratings, on which the code was written directly in the form of the superstructure function $A(x)$. The code was temporally much longer than the input pulses, so that in a good approximation these could be considered to be impulses. Then the signal $y_c(t)$ reflected off the encoder is given by (see Eq. 2.1)

$$y_c(t) = \delta(t) * h(t)$$

or $y_c(t) = h(t)$, where $h(t)$ is the impulse response of the FBG, which as argued in section 2.1, is directly related to the superstructure function $A(x)$. A matched filter of the encoder was needed for the decoding. This was formed by a second FBG, identical to the first but illuminated from the opposite end, so that its impulse response was the time inverse of $h(t)$. The signal $y_d(t)$ reflected off the decoder was then

$$y_d(t) = h(t) * h(-t) = R_{xx}(\tau)$$

where $R_{xx}(\tau)$ is the autocorrelation function of $h(t)$.

The aim of the experiment was to explore the feasibility of using this technique to perform coherent, passive, direct sequence pulse encoding and decoding, suitable for application in OCDMA systems. Thus, the code used was the shortest pseudorandom sequence, which consists of 7 chips and is 0100111 [Knuth81]. In order to be able to easily detect and observe the signals, the whole experiment was designed for a symbol repetition rate of ~125MHz (8ns period), while the total code duration was much shorter, namely 1.82ns, to avoid interference between two successive signals at the reception side. Two identical superstructured gratings were prepared at the wavelength of operation of the laser source. The refractive index of the gratings was modulated using the pseudorandom pattern. Each one of the chips was 26.9mm long, resulting in an overall grating length of 188.3mm.

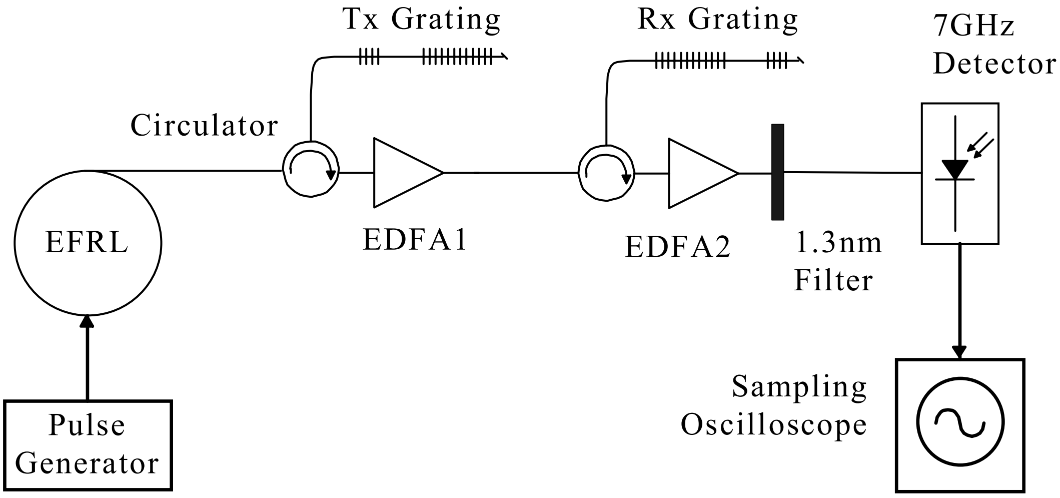

Fig. 2.1 The experimental set-up for demonstration of all-optical CDMA encoding and decoding using fibre Bragg gratings

The experimental set-up is shown in fig. 2.1. The actively mode-locked ring laser (described in Chapter One) operating at 1555.8nm was used as the short pulse source. Since we required a low pulse repetition rate from the laser (~125MHz), we had to drive the $LiNbO_3$ modulator (active mode-locking element within the ring cavity) with an external pulse source rather than the 10GHz PLL described in Chapter One. This compromised the long-term stability of the source, however its operation was still sufficiently stable in time to conduct the required experiments. Sinusoidal modulation of the cavity loss at 125MHz alone resulted in pulses that were too long for our needs, so instead we drove it with 400ps electrical pulses at ~125MHz, thereby obtaining 40ps pulses, as detected with a 7GHz detector on a suitably fast sampling oscilloscope. Although these pulses were somewhat longer than desired, they were adequate for our experiments. Two EDFA's were used to enhance the signal levels reflected back from the weak gratings (as shown in fig. 2.1), whereas excessive ASE from the amplifiers was rejected by the 1.3nm filter.

The pulses were fed into the first grating, where they were encoded with the 7-chip pattern. This code was then transmitted, and then decoded at the receiver side, using the second grating. One of the gratings (the receiver one in this case) was strain tuned to finely adjust the wavelength of its operation exactly to the wavelength of the other grating. The signal reflected back from this grating was effectively the cross-correlation of the transmitted signal and the code of the matched filter.

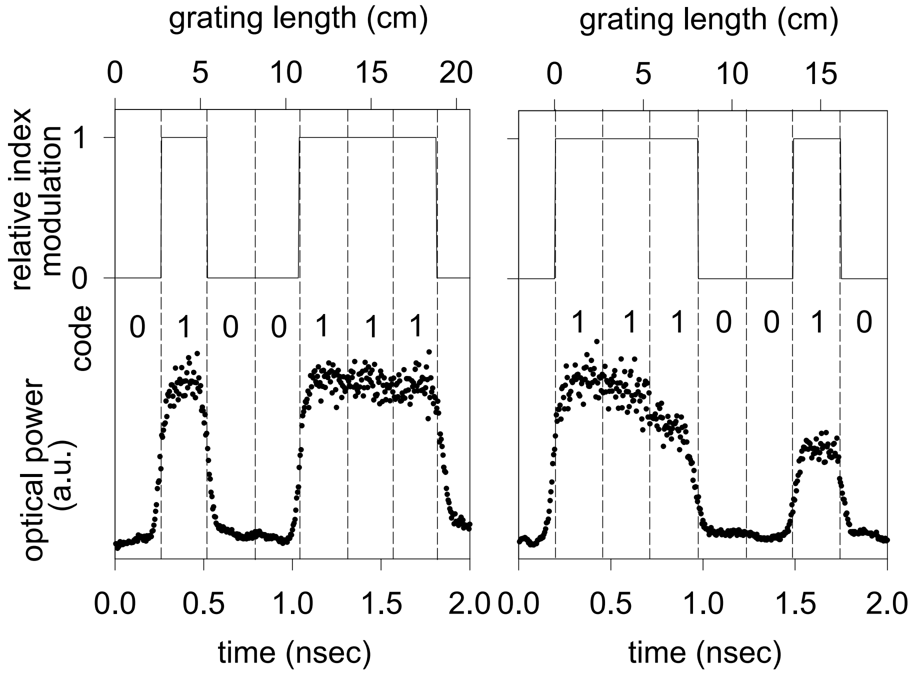

(a) (b)

Fig. 2.2 Modulation of the refractive index (top traces), the represented codes and the impulse responses (bottom traces) of (a) the transmitter and (b) receiver FBG

Initially, the impulse response of the individual gratings was examined by detecting the reflected waveforms reflected back from them, when a short pulse from the ring laser was fed onto them. The responses are shown in fig. 2.2a and 2.2b (lower traces) for the transmitter and receiver grating respectively. The upper trace of each figure shows the modulation of the refractive index of each grating versus its length. The decay towards the end of the response of the receiver grating is due to it having a stronger index modulation than required, resulting in less optical power reaching the end of the grating, and consequently less contribution from that section of the grating to the response.

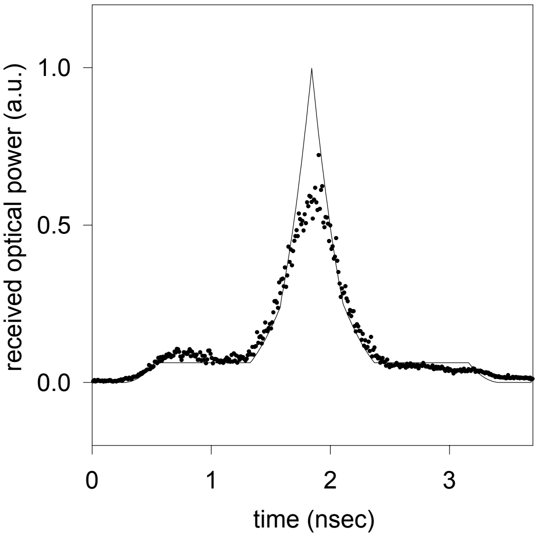

Fig. 2.3 Received autocorrelation waveform; experimental (dots) and theoretical (solid line)

A trace of the actual autocorrelation waveform acquired at the receiver end is shown in fig. 2.3. Superimposed is the predicted autocorrelation waveform as calculated from the theory (scaled appropriately). Although the acquired waveform follows the predicted one reasonably well, it differs from it in two main regards: The second (right-hand in the figure) "shoulder" is lower than the first, which can be attributed to the fact that the reflectivity of the receiver grating was slightly higher than intended and resulted in an appreciable decay in intensity along the grating length; secondly, the peak of the acquired autocorrelation trace is clearly not as pronounced as that theoretically predicted. This can be attributed partly to bandwidth limitation of the detection system and partly to the fact that the input pulses were not infinitely short, as the simplified theory requires.

It is worth mentioning that the same concept of pulse encoding and decoding using FBG's has been recently employed by [Grunnet-Jepsen99]. The initial experiments reported herein urged for a further, and more detailed investigation of the pulse encoding and decoding problem. More information about the directions that our ongoing research is taking will follow in Chapter Three.

2.3 Shaping of solitons into square pulses

In the previous experiment, the precise shape of the encoded pulses, although important, was not absolutely critical for the successful operation of the pulse encoding/decoding scheme. The critical issue was to match the characteristics of the two filters used (encoder and decoder). The grating structures written were fairly simple, consisting of a number of discrete sections (chips), on which either a uniform grating was written or no grating was written at all. This design assumed that the input pulses were infinitely narrow (impulses), and did not take the pulse duration and shape into account (other than that the pulse duration was shorter than the chip length). This simplification was well justified in our experiments, as the encoded sequence was some 45 times longer than the input pulses, and the filtered spectrum occupied only a small fraction of the input pulse spectrum. Therefore, the effect of neglecting the detailed pulse shape was minimal, and manifested itself as small discrepancies between the rising and falling edges of the encoded and decoded signal.

In the experiment described in this section on the other hand, the requirements imposed on the pulse shaper were more stringent, as the full bandwidth of the input pulses was employed, in order to produce an accurately pre-defined, temporally narrow waveform. The target of the experiment was to reshape the well-defined soliton pulses, generated from the 10GHz actively mode-locked erbium fibre ring laser (described in Chapter One), into square pulses. Such pulses are suitable for nonlinear switching applications, in which a narrow square switching window is required. For this shaping application, the spectrum of the input pulses needs to be filtered in both amplitude and phase, since the representation of the electric field of square pulses in the frequency domain is the sinc-function, which consists of alternating lobes of inverse phase.

Since the shaping procedure relies on passive filtering of the input spectrum to generate the desired output, the exact shape of the input pulses had to be taken into account while designing the grating. Thus, 2.5ps soliton pulses were assumed at the input, which can readily be obtained from the laser source. These pulses had a 3dB spectral bandwidth of 1nm, whereas their full bandwidth was restricted to 6nm due to the intracavity filter of the laser (see section 1.2). The width of the targeted pulses was chosen with respect to the input: Since the bandwidth available for shaping was that of the input signal, the output pulse duration should be sufficiently broad to ensure that all the main spectral features could be adequately formed. A full bandwidth, i.e. from the spectral peak to the first zero, of ~0.8nm (corresponding to 0.1THz) for the central lobe permitted 12 more spectral lobes to be fitted within the available bandwidth, six from either side. A narrow bandwidth corresponds to wide pulses. The width of the square pulses that corresponded to this spectrum was 20ps.

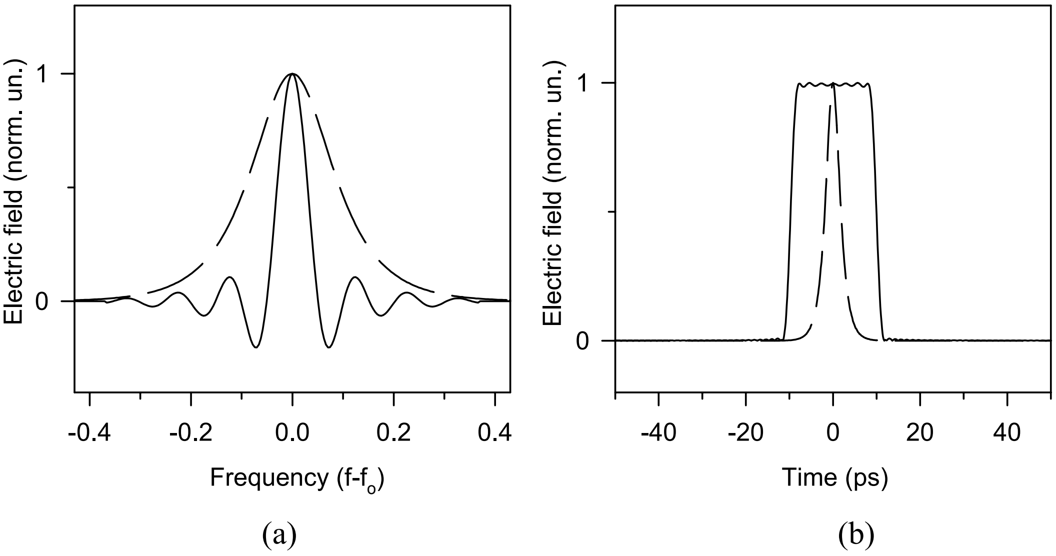

(a) (b)

Fig. 2.4 Calculated graphs of the electric field representation of the input 2.5ps soliton pulses (dashed lines) and the output 20ps square pulses (solid lines) in (a) the frequency and (b) the time domain

The truncation that was imposed on the sinc-spectrum would have resulted in the development of a ringing structure close to the edges of the square pulses in the time domain (Gibbs phenomenon). In order to reduce this ringing, Gaussian apodisation was superimposed on that sinc-shape. Hence, the equation describing the targeted signal in the frequency domain is

$$Y(\omega) = \frac{\sin(p\omega)}{p\omega} \cdot e^{-(a\omega)^2}$$

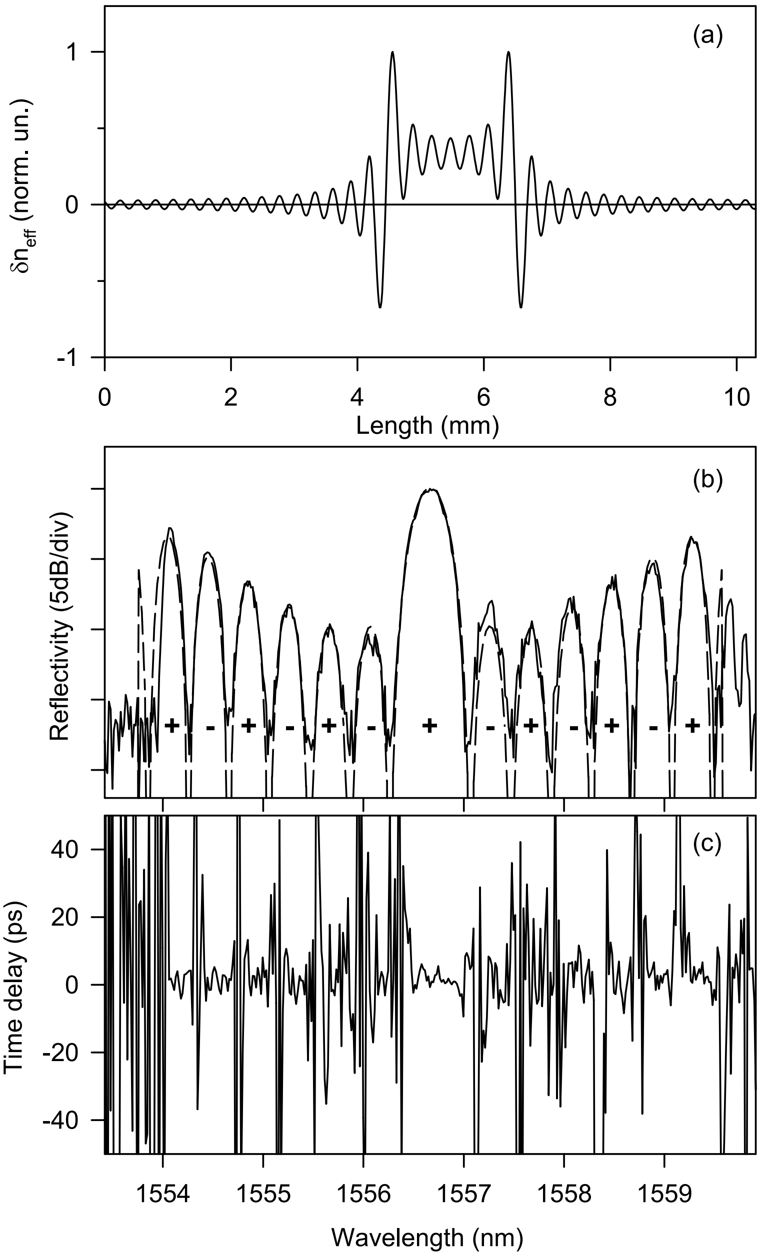

Fig. 2.5 (a) Refractive index modulation profile of the FBG performing shaping of solitons into square pulses; (b) spectral response and (c) time delay vs. wavelength of this FBG. In (b) the dashed line shows the calculated spectral response of the structure designed

The factor *p* in this equation determines the spectral width, and in our case was set to 9.87THz^{-1}. The expense of introducing apodisation comes in increasing the rise and fall times of the pulses. The apodisation factor *a* was hence kept fairly small, namely 0.55THz^{-1}, to give a satisfactory trade-off between the two effects (fig. 2.4). The response of the FBG in the frequency domain *H(ω)* could then be easily calculated from Eq. 2.2 as the quotient of the output $Y(\omega)$ (desired) to the input frequency response $X(\omega)$. This is shown in fig. 2.5b (dashed line). The inverse Fourier transform of $H(\omega)$ gave the superstructure function that was required to be written on the FBG (fig. 2.5a). Its full length in time was t = 100ps, corresponding to a grating length of $0.5 \cdot t \cdot c/n$ = 10.3mm. Note that negative values on the superstructure function imply a π phase shift of the refractive index modulation.

The FBG fabricated was rather weak, only ~10% reflective. The low reflectivity in this instance was limited by the photosensitivity of the fibre. In fact, in this particular case, the inherent weak grating requirement mentioned in section 2.1 was not imposing any practical limits on the FBG strength. This is not only due to the short length of the FBG, but due to the shape of the superstructure function as well, according to which the strongest refractive index modulation takes place over just ~3mm in the central part of the structure.

The grating was characterised across the wavelength range of interest using an optical network analyser. This consisted of a tuneable narrowband laser source externally modulated at 3GHz, which was coupled to the device under test (the FBG in this case). The amplitude and relative phase of the reflected signal from the grating was subsequently detected. The measured spectral response and the time delay graph of the FBG are presented in fig. 2.5b and 2.5c respectively. It is worth noticing that there is a π phase shift between the optical phases of any two adjacent spectral lobes shown in fig. 2.5b, producing at the output the phase shifts required to form the sinc-like spectrum of fig. 2.4a.

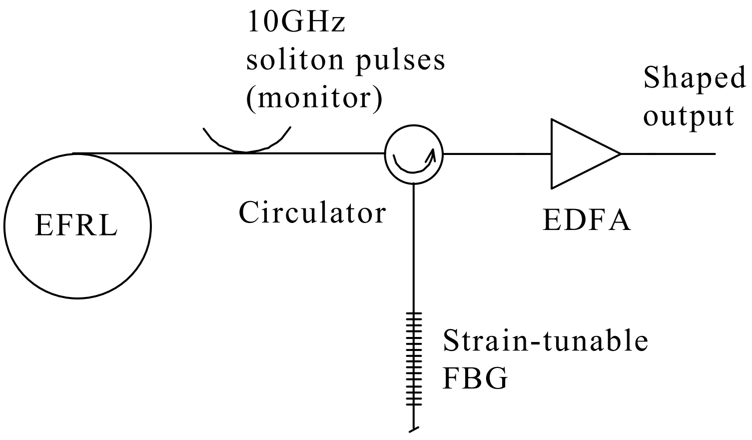

Fig. 2.6 Experimental set-up for pulse shaping applications using superstructured FBG's

The experimental set-up is fairly straightforward (fig. 2.6). The central wavelength of the soliton laser was tuned to the central wavelength of the FBG, and the pump power adjusted to ensure that the width of the output pulses was ~2.5ps. These pulses were then coupled onto the FBG by means of an optical circulator. The FBG was mounted on a rig to allow for fine tuning of its central wavelength relative to that of the source. An EDFA was used at the third port of the circulator to amplify the weak reflected pulses.

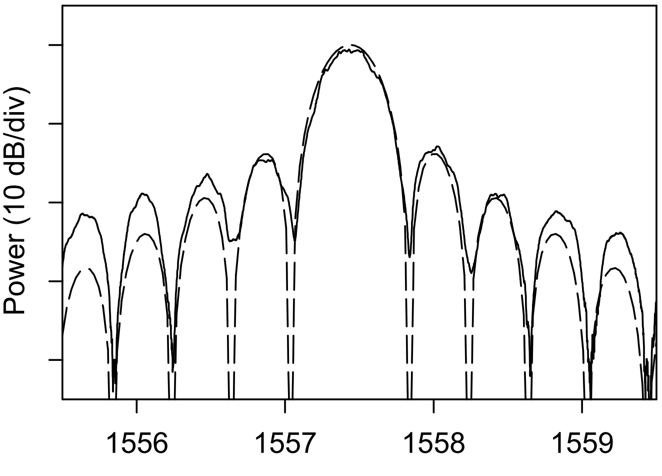

Fig. 2.7 Measured power spectrum of the reflected signal (solid line) compared to the calculated power spectrum of the 20ps square pulses of fig. 2.4a (dashed line)

The power spectrum of the pulses reflected off the FBG is shown in fig. 2.7, and is compared to that expected from the design procedure. The characteristics of this spectrum seem to match well an ideal sinc^2-spectrum. The amplitude of the first lobes is ~12.5dB lower than the central spectral lobe, close to 13.3dB, which is the corresponding figure for the sinc^2-function. The temporal shape of the reflected pulses was evaluated initially using an autocorrelator. The autocorrelation function of a square pulse of duration T is a triangular pulse of total duration 2T. An autocorrelation trace of the filtered pulses is shown in fig. 2.8, and is compared to the calculated autocorrelation function of the targeted waveform, and an autocorrelation trace of the input pulses. The shaping action of the FBG can easily be appreciated.

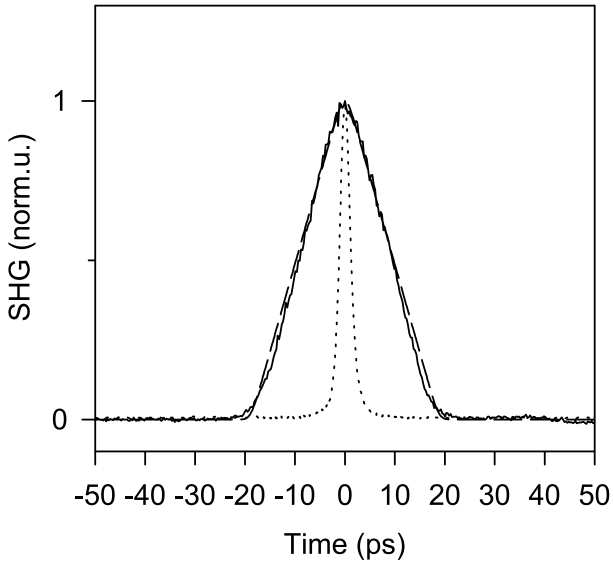

Fig. 2.8 Measured autocorrelation traces of the 2.5ps soliton pulses (dotted line) and the reflected pulses (solid line); the dashed line shows the calculated autocorrelation function of the square pulses of fig. 2.4b

To establish more directly the quality of shaping achieved, an optical sampling oscilloscope was used. These measurements were carried out in collaboration with BT labs who have developed such an instrument. The optical sampling oscilloscope used an electroabsorption modulator and an electronically driven delay circuit to sample the optical signal at several delayed instances relative to the trigger source, which was the mode-locked laser in our case [Ellis98]. The resolution of this device was ~7ps, as determined from the trace of the significantly narrower soliton pulses (fig. 2.9a). This limited resolution affects the apparent rise and fall times in the oscilloscope trace of the filtered pulses shown in fig. 2.9b. The slightly uneven top of the pulse is most probably due to a small amount of chirp introduced by the FBG during the filtering process. Some chirp is also evident in the time delay vs. wavelength graph of the grating in fig. 2.5c. Nevertheless, the main targets of the shaping operation, i.e. the generation of an almost flat top and sharp edges, are clearly demonstrated.

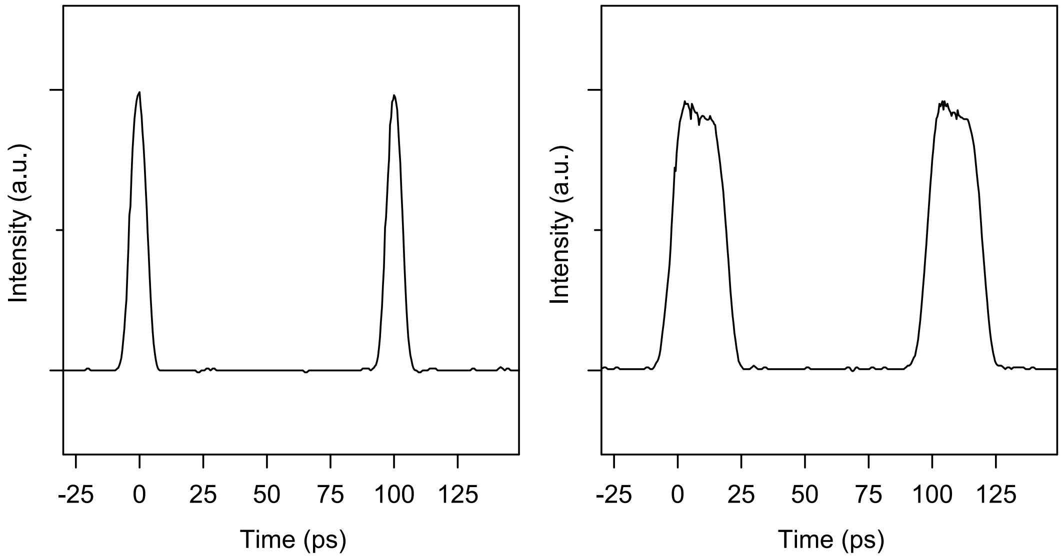

(a) (b)

Fig. 2.9 Optical sampling oscilloscope traces of (a) the input pulses and (b) the reflected off the FBG pulses

Furthermore, again in collaboration with BT labs, and in order to establish the noise properties of the shaped pulse stream, a BER measurement of the square pulses was carried out. The result of this measurement is shown in fig. 2.10, and is compared to the BER curve of the ring laser itself. The power penalty observed in the comparison of the two curves can be mainly attributed to the power loss due to the filtering process. However, the main outcome of the measurement is that the filtering is a rather noiseless operation, as error rates much lower than 10^{-9} can readily be achieved.

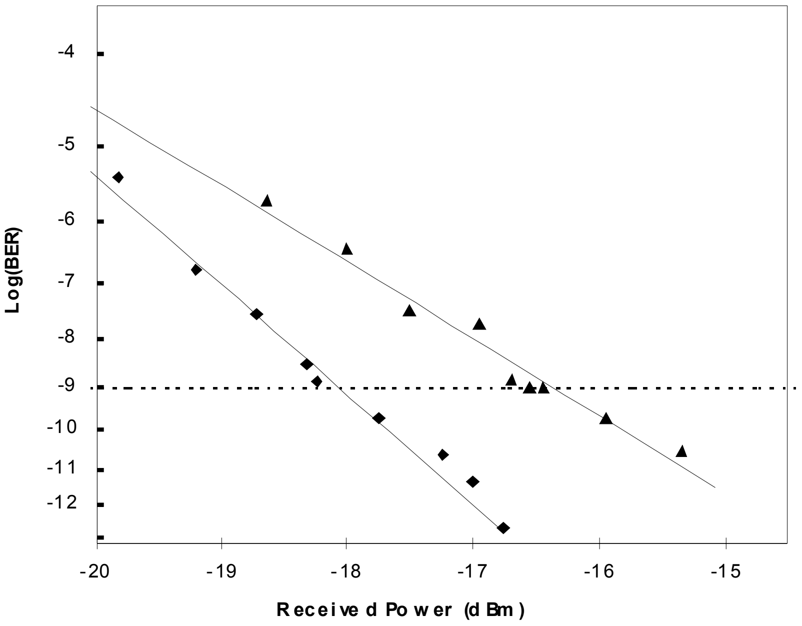

Fig. 2.10 BER curves of the input soliton pulses (diamonds) and the reflected square pulses (triangles)

2.4 Repetition rate multiplication

The applications described previously aimed at a radical change in the characteristics of individual pulses. The spectral envelope of short input pulses was manipulated and the relative optical phases across the spectrum were rearranged to produce reflected waveforms with radically different pulse shapes. The aim of the experiment that will be described next is somewhat different. Rather than focusing on altering the shape of the individual pulses, the pulse stream produced from the mode-locked laser is viewed as a whole. While the individual characteristics of the pulses are maintained, the repetition rate of the stream itself is altered by sampling appropriate spectral features in the pulse spectrum.

In [Azaña99] a pulse multiplication scheme based on the equivalent of the spatial self-imaging effect and making use of linearly chirped FBG's was suggested. Its practicality and the achievable quality of shaping however, is yet to be proven. On the other hand, the concept of pulse multiplication that we use lies in basic Fourier theory. The frequency representation of an infinitely long periodic pulse source with period T consists of infinitely narrow spectral lines separated by 1/T from each other.

The phases of these lines are locked relative to each other, and in the case of transform limited pulses the lines are all in phase. The shape of the envelope formed by these lines corresponds to the exact shape of the individual pulses in time, being broader for shorter pulses and vice versa. Multiplication of the repetition rate can then be performed by a filter that will selectively filter out certain spectral lines, thereby changing their periodicity. At the same time, the phase coherence of the remaining spectral lines has to be retained. This concept has been demonstrated before, using a carefully tuned Fabry-Perot filter in the cavity of an actively mode locked laser, to permit only certain of the cavity's longitudinal modes to contribute to the output [Abedin98]. In our experiment however, we have placed the filter outside the laser cavity, performing true all-optical multiplication of the repetition rate, rather than intracavity mode selection. The approach is thus independent of the nature of the source used and is thus of more general applicability.

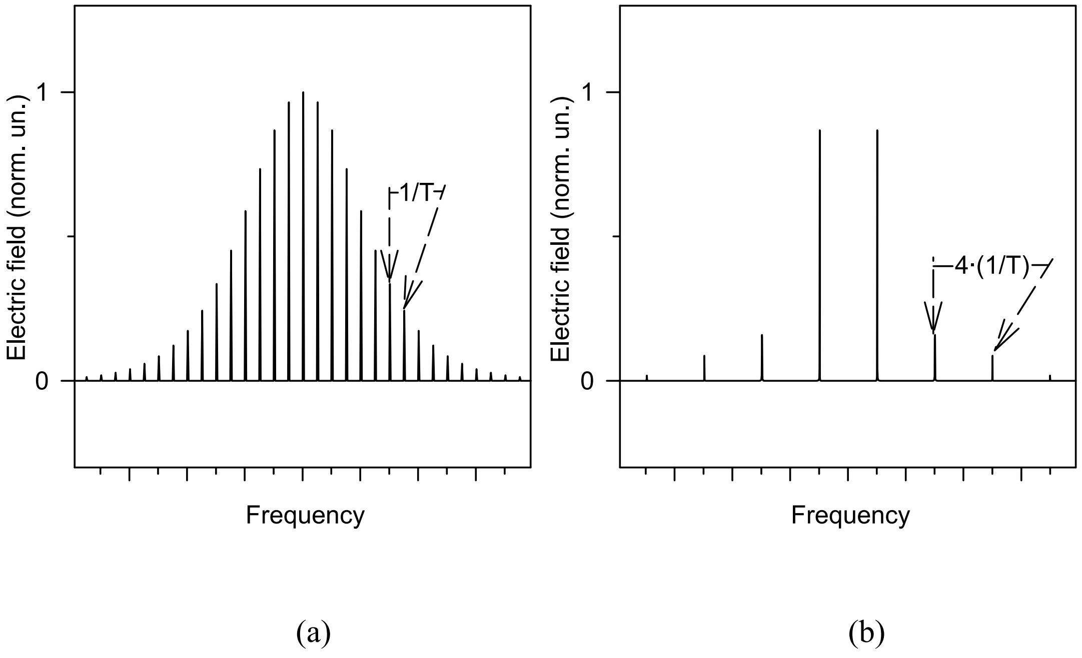

Fig. 2.11 Calculated electric field representations in the frequency domain of (a) the 10GHz and (b) the 40GHz pulse stream

The target of our experiment was to multiply the repetition rate of the 10GHz pulses generated from our erbium-fibre mode-locked laser by four times, to yield a 40GHz pulse stream at the output. The spectrum of the filtered pulses should differ from that of the input only by the spacing between the lines that comprise it (fig. 2.11). The spectral envelope and the phase relation between the remaining lines should be retained, in order to ensure that the shape of the individual pulses remains unaltered. These requirements suggest that the spectral response of the FBG should exhibit narrow channels across the full bandwidth of the original pulses, separated from each other by exactly 40GHz. The optical phases of the channels should all be the same. Also, the FBG should have a square overall envelope, so that the spectral envelope of the incoming signal is not affected by the filtering action.

Superstructured FBG’s exhibiting multiple channels have been demonstrated in the past [see e.g. Eggleton94], and are known as sampled gratings. In general, the name sampled gratings is used for superstructured gratings in which the refractive index modulation profile is some periodic function. Very similar designs of sampled FBG’s to those used in our experiment were first reported in [Ibsen98], where the capability to fabricate FBG’s with a predictable number of channels of identical characteristics was most impressively demonstrated. The sampling function used in the paper followed a sinc-profile, which ensured a square overall spectral envelope, i.e. identical strength for all channels. The channel separation was inversely proportional to the period of appearance of the sampling function in the grating structure, whereas the number of channels was determined by the width (in space) of the sinc-function.

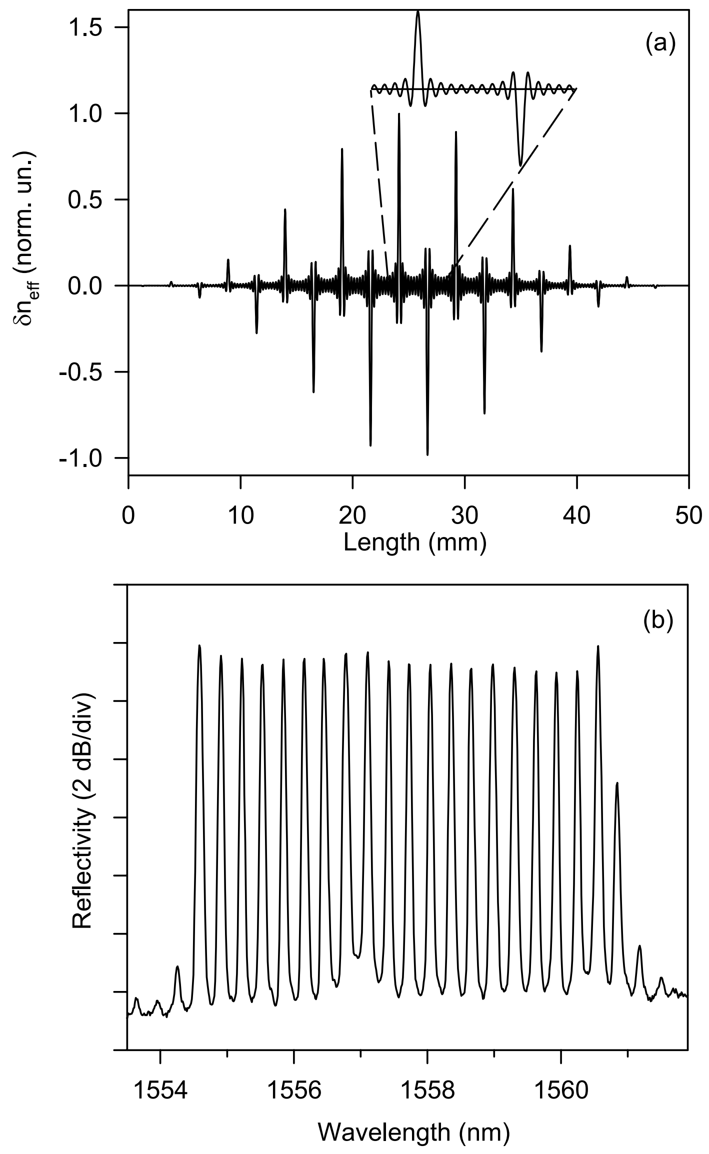

Fig. 2.12 (a) The superstructure function used for the pulse multiplication FBG; inset shows a detail of the refractive index modulation profile; (b) measured spectral response of the pulse multiplication FBG

The length of the FBG used in our experiment was 50mm. The superstructure function used to write it is shown in fig. 2.12a. The overall structure followed the Blackman apodisation profile for optimum extinction of the channels' sidelobes. The spectral response of this grating is shown in fig. 2.12b. The strength of the FBG was, as in the previous experiment, also ~10%. This was again due to lack of a photosensitive enough fibre rather than an inherent limit of the technique. The linewidth of each of the channels of the FBG, which was determined by the length and shape of the envelope of the total structure, was ~5GHz. This ensured good extinction of the adjacent undesirable 10GHz spectral lines whilst allowing for good tunability. In fact, the performance of this FBG was compared to a second one that was fabricated and exhibited a 10GHz linewidth. The comparison showed that the two FBG's performed similarly, as far as tunability was concerned. The filtering quality however, of the second FBG was much inferior to the first, as the filtered pulses exhibited substantial background noise. The inferior filtering quality of this FBG was also verified numerically (fig. 2.13).

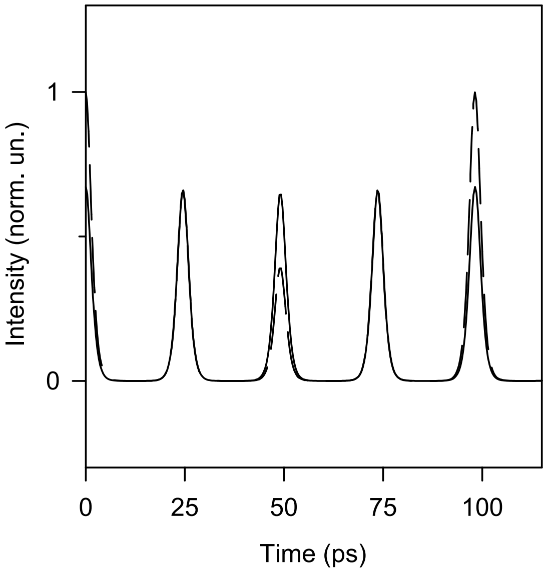

Fig. 2.13 Calculated 40GHz pulse streams resulting from pulse multiplication filters having a channel linewidth of 5GHz (solid line) or 10GHz (dashed line)

Characterisation of the FBG in terms of the optical phase properties of the channels revealed that they exhibited a small amount of chirp (fig. 2.14). This infers that unless the channel separation of the FBG is an exact multiple of the repetition rate of the input signal, the spectral lines at the filtered output will experience a slightly different phase relation to those at the input. This will obviously affect the chirp of the pulses. A numerical study of the problem however, showed that this small amount of chirp had minimal effect on the pulse shape. In fact, the greater distortion observed was due to the uneven level of filtering imposed on the various 40GHz spectral lines, because of their non-symmetric distribution about the grating channels. Effectively, a detuning of the repetition rate of the source by ~0.3GHz relative to the channel spacing was required to cause a significant distortion on the pulse shapes, manifesting itself as a loss in peak power and a slight pulse broadening (fig. 2.15a).

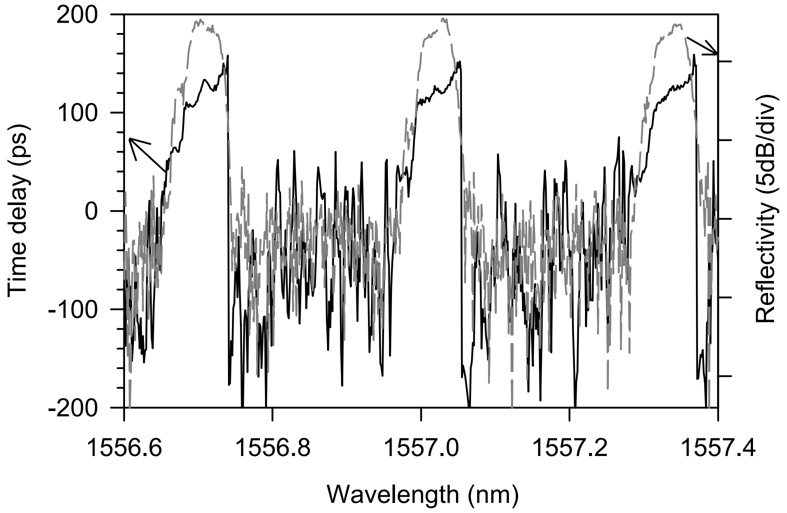

Fig. 2.14 Time delay measurement for three of the channels of the sampled FBG (solid line); dashed line shows the spectral response of these channels

Another problem that was studied numerically was that of imperfect matching of the central wavelength of the source to that of the FBG. This case was simpler and its

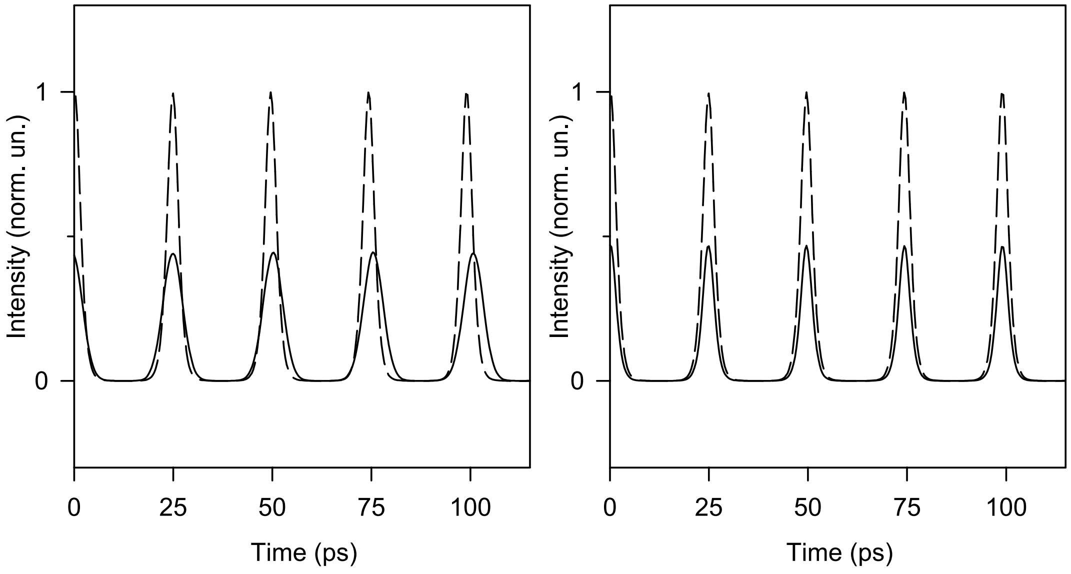

(a) (b)

Fig. 2.15 Simulation of the effect of imperfect tuning in the pulse multiplication operation (solid lines): (a) the repetition rate of the source is detuned by 0.3GHz from the exact FBG channel spacing; (b) the central wavelength of the source is detuned by 1.3GHz from the central wavelength of the FBG. Dashed lines represent the reflected pulses for the case of correct tuning of the FBG effect less destructive. If the pulse repetition rate is exactly matched on the channel spacing, then all 40GHz spectral lines experience the same attenuation and the same phase shift from the filter, as they "sit" on exactly the same point of each channel. The chirp of the pulses is not affected, and only their peak power drops as the detuning becomes more severe. Fig. 2.15b shows the pulse form obtained for a detuning of the input spectral lines by 1.3GHz from the centre of the FBG channels. Of course, in the case where extreme detuning is considered, the undesired adjacent spectral line of the input may become significant and clear distortion in the pulse shape can also be observed.

The experimental set-up was similar to that presented in fig. 2.6. Mounting the FBG on a stretching clamp was essential for the tuning procedure and to ensure stable operation. The spectrum of the input pulses had a 3dB bandwidth of 0.85nm, while the pulse width was 3.4ps, as measured with an autocorrelator. The repetition rate of the source was adjusted to 10GHz, and its central wavelength was tuned to the central wavelength of the FBG. The spectra of the original and shaped pulses are compared in fig. 2.16, where the resultant 40GHz spectrum is evident. It is also worth noticing that the envelopes of the two spectra are the same, due to the square envelope of the FBG. The shapes of the two signals in the time domain are compared in fig. 2.17. The width of the output pulses is the same as that of the input, i.e. 3.4ps, leading to the conclusion that the shaping action has not significantly altered the pulse shape. As

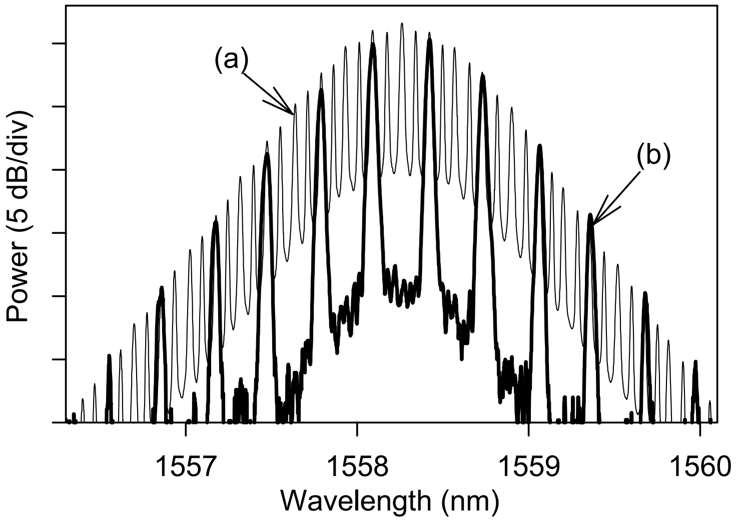

Fig. 2.16 Power spectra of (a) the 10GHz input and (b) the 40GHz reflected pulses

with the previous experiment, the pulses were also observed in real time with an optical sampling oscilloscope. The result of this measurement is shown in fig. 2.18. Note however, that as before, the measurement was limited by the resolution of the oscilloscope.

The experiment operated for long periods of time with no significant degradation in the performance, and without any need for active stabilisation of the grating length. Finally, we have currently not identified any other limiting factors on the repetition rates or multiplication factors achievable using such FBG's, other than the pulse width of the incoming pulses. This limitation can be viewed either as intersymbol interference between adjacent pulses, or as lack of a sufficient number of spectral lines to construct a coherent pulsed signal as one moves to higher repetition rates, i.e. wider spacing between adjacent spectral lines.

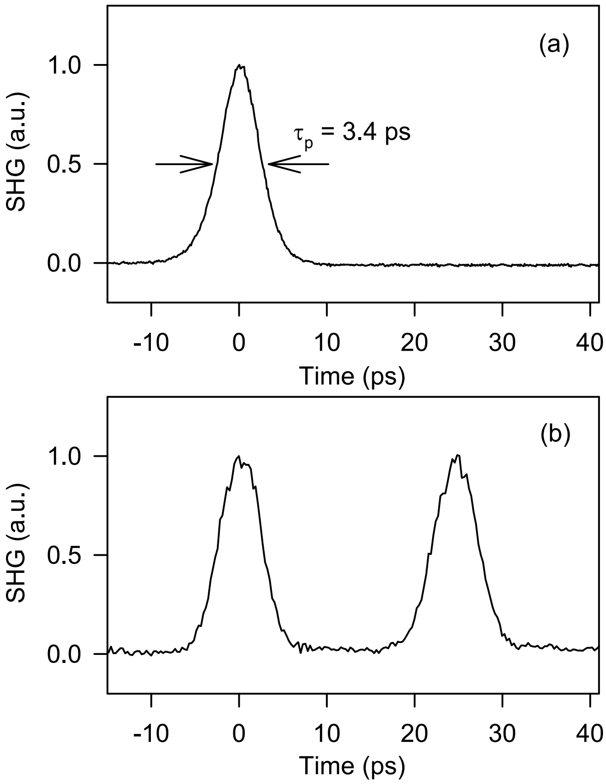

Fig. 2.17 Autocorrelation traces of (a) the 10GHz input and (b) the 40GHz output pulses. The pulse width has remained unaffected

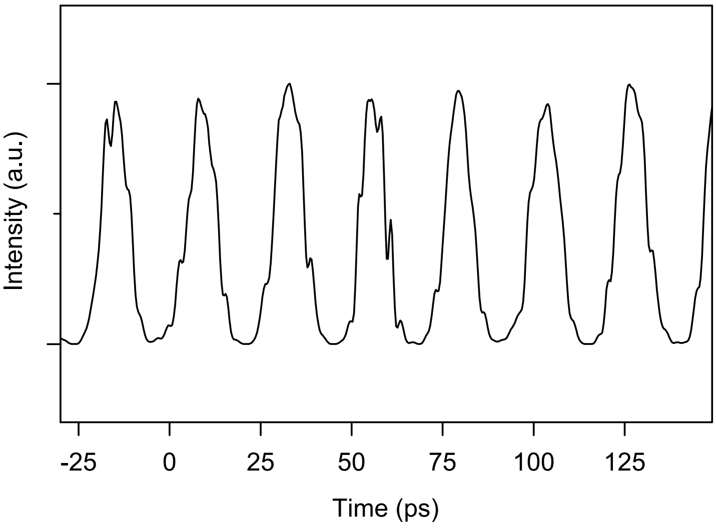

Fig. 2.18 Optical sampling oscilloscope trace of the 40GHz pulse train (to be compared to trace of input pulses of fig. 2.9a)

2.5 Conclusions

The advent of FBG's fabrication technology in the recent years has allowed the implementation of sophisticated filters, suitable for a broad range of operations in optical processing. In this chapter we have demonstrated the capability to implement complex grating structures, the realisation of which required precise control over their amplitude and phase properties. Furthermore, we have used these FBG's for coherent manipulation of short pulses. Such demanding control over the properties of optical signals would not have been possible with conventional approaches that use electronically driven devices. In addition, unlike most other all-optical methods that have been applied to pulse shaping, this one is fully fiberised, offering automatic compatibility with optical telecommunications systems.

We have explored the technique with three independent experiments. The pulse encoding/decoding scheme was effectively a direct demonstration of the basic principle, i.e. that the refractive index profile of a FBG is related directly to its impulse response. The feasibility of employing such encoders and decoders for CDMA systems was also illustrated. The two other experiments, which achieved reshaping of solitons into square pulses and multiplication of the repetition rate of a pulse stream, were examples of precise filtering in both the amplitude and phase characteristics of the incoming signal. We believe that the experiments described herein are only few examples of applications where such filtering could find use.

Chapter Three

Future Directions

Overview: Some of the research possibilities offered by the work presented in this part of the thesis are reviewed.

The activities presented in the previous two chapters can be used as the starting point for numerous other experiments investigating suitable sources and pulse shaping applications for the future fibre-optic telecommunications networks. Some examples are given below.

Chapter One: The 10GHz mode-locked EFRL presented in Chapter One is already an excellent source of short pulses. Further actions to enhance its performance would be to optimise its intracavity dispersion map to give a shorter pulse option and higher pulse energy. In addition, we would like to incorporate a control scheme which locks the cavity length to a given frequency reference, to facilitate synchronisation to a second pulsed source. Finally, to extend the operating wavelength range it should be possible to use the source to generate a broad supercontinuum. This can be readily achieved by subsequent amplification and propagation of the signal through a nonlinear medium of low dispersion, such as a DSF [Morioka95]. Such a broadband output can then be used for a number of different applications. For example, the spectrum can be sliced using FBG’s to produce multiple (phase locked) high bit-rate WDM sources.

Chapter Two: Availability of the supercontinuum of the 10GHz source would enable the use of a much broader spectrum for the pulse shaping applications. For example, in the same fashion as that was described in section 2.3, FBG's could be used to generate ultrashort square pulses. In the experiment described in that section, the width of the output pulses was clearly limited by the available bandwidth for the shaping operation. Exploitation of a wider bandwidth will allow the shaping of the signal into shorter pulses.

The coding/decoding work presented in Chapter Two can also be further extended. Preliminary experiments have already been carried out to utilise the phase of the pulses. This provides the potential for bipolar encoding, offering significant improvement in the contrast in the received autocorrelation waveform [Teh00]. These experiments took place at 10GHz, demonstrating its potential for use in a 10Gbit/s OCDMA transmission system. Pattern recognition using superstructured FBG's can also be applied in other cases, where, for example the encoding is realised in the electrical domain, enhancing thus the flexibility and functionality of the approach. The use of such concept in OTDM networks as well as OCDMA systems should also be considered.

The repetition rate multiplication concept presented in section 2.4 can also be further extended. The obvious direction is to attempt the use of higher multiplication factors to generate even higher bit-rates. Also, the components of the 10GHz signal transmitted through the FBG, and which have so far been wasted, can be further filtered by subsequent arrays of similar FBG's (with appropriately offset central wavelengths), so as to generate additional pulse multiplied channels. This can provide a power-efficient means of generating several phase-locked high-bit-rate sources from a single source of a lower bit rate.

Appendix P1.A

Diagram of the electronic control circuit of the Phase-Lock Loop

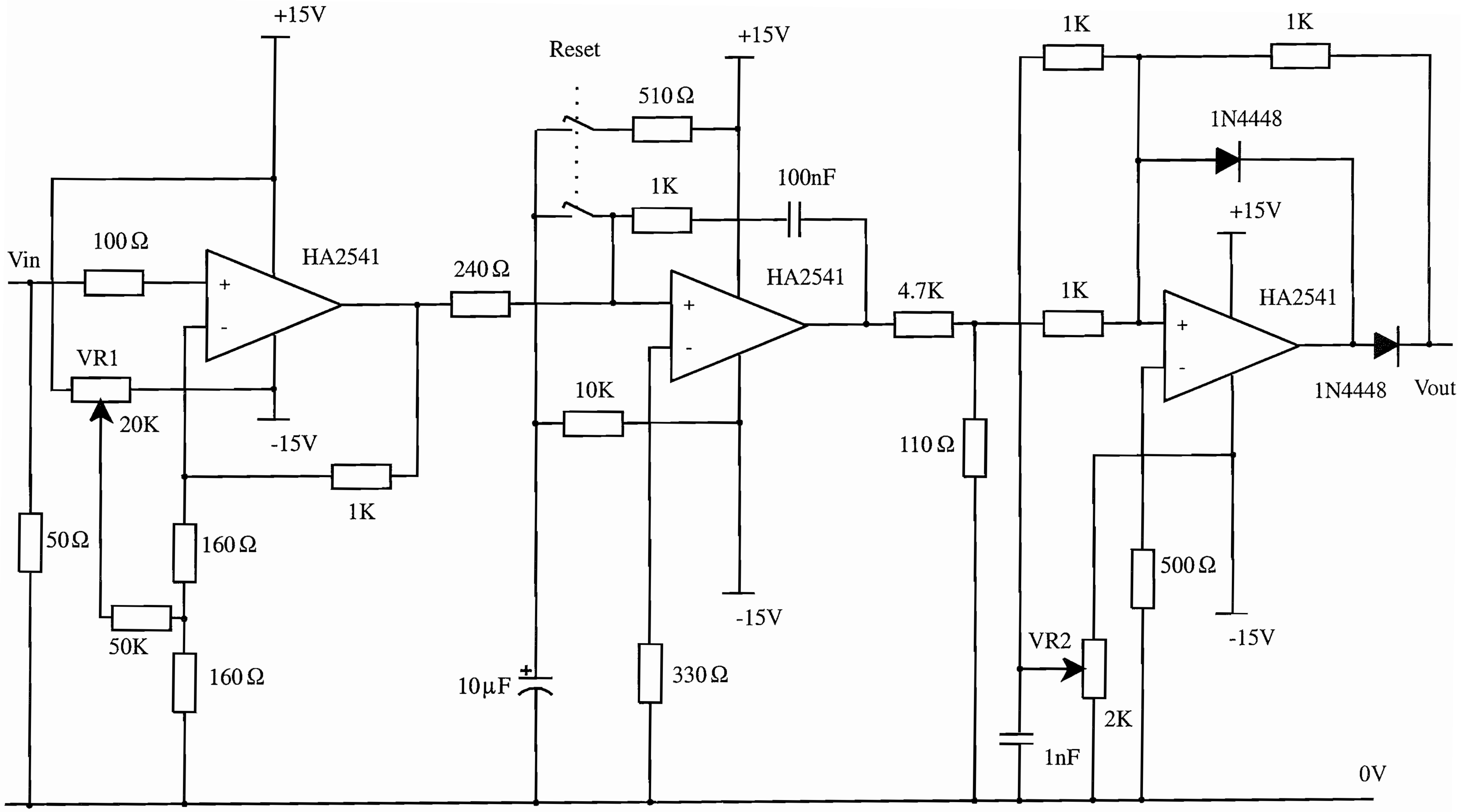
+15V
Reset
+15V
1K
1K
510Ω
1N4448
1K
100nF
+15V
100Ω
Vin
HA2541
240Ω
HA2541
4.7K
1K
HA2541
+
-
+
-
+
-
VR1
10K
1N4448
Vout
20K
-15V
110Ω
1K
50Ω
160Ω
500Ω
-15V
-15V
50K
VR2
160Ω
10μF
330Ω
2K
1nF
0V

Appendix P1.B

Measurement of amplitude noise and temporal jitter in cw mode-locked lasers

An extended discussion on the characterisation of the noise in cw mode-locked lasers is given in [Linde86]. A summary of this discussion is presented below.

The noisy laser intensity *F(t)* can be written as

$$F(t) = F_0(t) + F_0(t)A(t) + \dot{F}_0(t)TJ(t) \qquad \text{(B1)}$$

where $T = 1/f_r$ is the period of the pulses and $F_0(t)$ the output intensity of the perfectly mode-locked laser. The second term in eq. B1 represents amplitude fluctuations characterised by a random function *A(t)*, which gives the relative deviation from the average pulse amplitude. The third term represents fluctuations of the repetition rate, i.e. the temporal jitter of the pulses, and is characterised by a random function *J(t)*, which represents the relative deviation from the average pulse repetition time *T*. The power spectrum $P_F(\omega)$ of the laser intensity is given by the Fourier transform of the autocorrelation function of *F(t)* and can be expressed as

$$P_F(\omega) = (\Delta\omega)^2 \,|\, f(\omega) \,|^2 \sum_n [\delta(\omega_n) + P_A(\omega_n) + (2\pi n)^2 P_J(\omega_n)] \qquad \text{(B2).}$$

In eq. B2 $P_A(\omega)$ and $P_J(\omega)$ are the power spectra of *A(t)* and *J(t)* respectively, $\Delta\omega = 2\pi f_r$ is the spacing between the frequency bands f_r, $f(\omega)$ is the Fourier-transform of the intensity profile of the individual ideal pulses, which is considered to remain constant, n is an integer running from minus to plus infinity, and $\omega_n = (\omega - \frac{2\pi n}{T})$ labels the individual frequency bands. Simply put, eq. B2 shows that the power spectrum of the pulses consists of a constant envelope representing an ideal pulse sequence of repetition rate $\omega = 2\pi f_r$, and a rapidly varying component represented by the two last terms in the sum. Thus, the noise added to the δ-function of the power spectrum around a harmonic of the repetition frequency f_r can be distinguished in two bands of different origin (fig. P1.B.1). The band denoted as P_3 is the frequency shifted power spectrum of the amplitude noise, and P_2 is the band that corresponds to the frequency jitter. It is important to notice in eq. B2 that the jitter term is proportional to n^2. This fact permits one to distinguish between the two different kinds of noise and thus determine the two individual components $P_A(\omega)$ and $P_J(\omega)$, by analysing the noise bands that exist in different harmonics. Then the amplitude fluctuations and temporal jitter of the pulses, which are characterised respectively as the rms. deviation ΔE from the pulse energy E and the rms. deviation Δt from the repetition time T, can be determined as

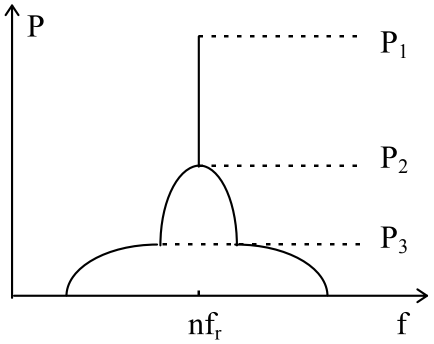

Fig. P1.B.1 Noise bands around the n-th harmonic of a mode-locked laser, indicating amplitude fluctuations (P_3) and temporal jitter (P_2) around the ideal value (P_1)

$$(\Delta E / E)^2 = \int_{-\infty}^{+\infty} P_A(\omega)d\omega$$

and
$$(\Delta t / T)^2 = \int_{-\infty}^{+\infty} P_J(\omega)d\omega \, .$$

These integrals can be approximated by the product of frequency width Δf times maximum power density $P(0)$:

$$\int_{-\infty}^{+\infty} P(\omega)d\omega \approx 2\pi\Delta f P(0) .$$

Therefore, a high resolution Δf_{res} frequency span with the spectrum analyser around the n-th order component can help determine the low frequency jitter contribution $P_J(\omega)$, since the power ratio can be expressed as

$$(P_2 / P_1)_n = 2\pi\Delta f_{res}[P_A(0) + (2\pi n)^2 P_J(0)] .$$

On the other hand, a lower resolution $\Delta f'_{res}$ frequency span will reveal a higher frequency component $P'_J(\omega)$ of the temporal jitter:

$$(P_3' / P_1)_n = 2\pi\Delta f_{res}'[P_A(0) + (2\pi n)^2 P_J'(0)] .$$

References (Part One)

[Abedin98] K.S. Abedin, N. Onodera, M. Hyodo, “Repetition-rate multiplication in actively mode-locked fiber lasers by higher-order FM mode locking using a high-finesse Fabry-Perot filter”, Applied Physics Letters, Vol. 73, pp.1311-3, 1998.

[Andrekson91] P.A. Andrekson, “Picosecond optical sampling using four-wave mixing in fibre”, Electronics Letters, Vol. 27, pp. 1440-1, 1991.

[Agrawal95] G.P. Agrawal, “Nonlinear fiber optics”, 2nd Edition, Academic Press Inc., 1995.

[Azaña99] J. Azaña, M.A. Muriel, “Technique for multiplying the repetition rates of periodic trains of pulses by means of a temporal self-imaging effect in chirped fiber gratings”, Optics Letters, Vol. 24, pp. 1672-4, 1999.

[Bakhshi97] B. Bakhshi, J.Hansryd, P.A. Andrekson, “Report on 40Gbit/s data and clock generation with ML-EFRL”, Deliverable No 11 (D104), ACTS Project AC053 MIDAS, 1997.

[Barcelos96] S. Barcelos, “Development and characterization of fibre devices for optical communications”, PhD Thesis, University of Southampton, 1996.

[Chang98] C.C. Chang, H.P. Sardesai, A.M. Weiner, “Code-division multiple-access encoding and decoding of femtosecond optical pulses over a 2.5-km fiber link”, IEEE Photonics Technology Letters, Vol. 10, pp. 171-3, 1998.

[Chen99] L.R. Chen, P.W.E. Smith, C.M. de Sterke, “Wavelength-encoding/temporal-spreading optical code division multiple-access system with in-fiber chirped moiré gratings”, Applied Optics, Vol. 38, pp. 4500-7, 1999.

[Costa82] Costa, Mazzoni, Puleo, Vezzoni, “Phase shift technique for the measurement of chromatic dispersion in optical fibres using LEDs”, IEEE Journal of Quantum Electronics, Vol. QE-18, pp. 1509-15, 1982.

[Debeau98] J. Debeau, B. Kowalski, R. Boittin, "Simple method for the complete characterization of an optical pulse", Optics Letters, Vol. 23, pp. 1784-6, 1998.

[Dennis99] T. Dennis, J.F. Young, "Optical implementation of bipolar codes", IEEE Journal of Quantum Electronics, Vol. 35, pp. 287-91, 1999.

[Eggleton94] B.J. Eggleton, P.A. Krug, L. Poladian, F. Ouellette, "Long periodic superstructure Bragg gratings in optical fibres", Electronics Letters, Vol. 30, pp.1620-2, 1994.

[Ellis98] A.D. Ellis, J.K. Lucek, D. Pitcher, D.G. Moodie, D. Cotter, "Full 10x10Gbit/s OTDM data generation and demultiplexing using electroabsorption modulators", Electronics Letters, Vol. 34, pp.1766-7, 1998.

[Ellis99] A.D. Ellis, R.J. Manning, I.D. Phillips, D. Nesset, "1.6ps pulse generation at 40GHz in phaselocked ring laser incorporating highly nonlinear fibre for application to 160Gbit/s OTDM networks", Electronics Letters, Vol. 35, pp. 645-6, 1999.

[Emplit97] P. Emplit, M. Haelterman, R. Kashyap, M. DeLathouwer, "Fiber Bragg grating for optical dark soliton generation", IEEE Photonics Technology Letters, Vol. 9, pp. 1122-4, 1997.

[Fathallah99] H. Fathallah, L.A. Rusch, S. LaRochelle, "Passive optical fast frequency-hop CDMA communications system", Journal of Lightwave Technology, Vol. 17, pp. 397-405, 1999.

[Feced99] R.Feced, M.N.Zervas, M.A.Muriel, "An efficient inverse scattering algorithm for the design of nonuniform fiber Bragg gratings", IEEE Journal of Quantum Electronics, Vol.35, pp.1105-11, 1999.

[Fetterman98] M.R. Fetterman, D. Goswami, D. Keusters, W. Yang, J.-K. Rhee, W.S. Warren, "Ultrafast pulse shaping: amplification and characterization", Optics Express, Vol. 3, pp. 366-75, 1998.

[Geiger98] H. Geiger, M. Ibsen, R.I. Laming, "Optimum receivers with fibre gratings", Technical Digest OFC'98, paper WI2, p. 152, 1998.

[Grunnet-Jepsen99] A. Grunnet-Jepsen, A.E. Johnson, E.S. Maniloff, T.W. Mossberg, M.J. Munroe, J.N. Sweetser, “Demonstration of all-fiber sparse lightwave CDMA based on temporal phase encoding”, IEEE Photonics Technology Letters, Vol. 11, pp. 1283-5, 1999.

[Halas87] N.J. Halas, D. Krökel, D. Grischkowsky, “Ultrafast light-controlled optical-fiber modulator”, Applied Physics Letters, Vol. 50, pp. 886-8, 1987.

[Hill97] K.O. Hill, G. Meltz, “Fiber Bragg grating technology fundamentals and overview”, Journal of Lightwave Technology, Vol. 15, pp. 1263-76, 1997.

[Hunter99] D.B. Hunter, R.A. Minasian, “Programmable high-speed optical code recognition using fiber Bragg grating arrays”, Electronics Letters, Vol. 35, pp. 412-4, 1999.

[Iaconis98] C. Iaconis, I.A. Walmsley, “Spectral phase interferometry for direct electric-field reconstruction of ultrashort optical pulses”, Optics Letters, Vol. 23, pp. 792-4, 1998.

[Ibsen98] M. Ibsen, M.K. Durkin, M.J. Cole, R.I. Laming, “Sinc-sampled fiber Bragg gratings for identical multiple wavelength operation”, IEEE Photonics Technology Letters, Vol. 10, pp. 842-4, 1998.

[Ibsen99] M. Ibsen, M.K. Durkin, M.J. Cole, M.N. Zervas, R.I. Laming, “Recent advances in long dispersion compensating fibre Bragg gratings”, IEE Colloquium on Optical Fibre Gratings, paper 6, Aston University, UK ISSN 0963-3308, 1999.

[Kafka89] J.D. Kafka, T. Baer, D.W. Hall, “Mode-locked erbium-doped fiber laser with soliton pulse shaping”, Optics Letters, Vol. 14, No. 22, pp. 1269-71, 1989.

[Kishore99] K. Kishore, C. Lowry, C.H. Lee, “Header recognition by use of soliton interaction in fibers”, Optics Letters, Vol. 24, pp. 445-7, 1999.

[Kiyan98] R. Kiyan, O. Deparis, O. Pottiez, P. Mégret, M. Blondel, “Stabilisation of actively modelocked Er-doped fibre laser by minimising interpulse noise power”, Electronics Letters, Vol. 34, pp. 2410-11, 1998.

[Knuth81] D.E. Knuth, “The art of computer programming”, 2nd Edition, Addison - Wesley, 1981.

[Kwok98] A. Kwok, L. Jusinski, M.A. Krumbügel, J.N. Sweetser, D.N. Fittinghoff, R. Trebino, "Frequency-resolved optical gating using cascaded second-order nonlinearities", IEEE Journal of Selected Topics in Quantum Electronics, Vol. 4, pp. 271-6, 1998.

[Lam98] C.F. Lam, D.T.K. Tong, M.C. Wu, E. Yablonovitch, "Experimental demonstration of bipolar optical CDMA system using a balanced transmitter and complementary spectral encoding", IEEE Photonics Technology Letters, Vol. 10, pp. 1504-6, 1998.

[Linde86] D. von der Linde, "Characterization of the noise in continuously operating mode-locked lasers", Applied Physics B: Photophysics and Laser Chemistry, Vol. 39, pp. 201-17, 1986.

[Morioka95] T. Morioka, K. Uchiyama, S. Kawanishi, S. Suzuki, M. Saruwatari, "Multiwavelength picosecond pulse source with low jitter and high optical frequency stability based on 200nm supercontinuum filtering", Electronics Letters, Vol.31, pp.1064-6, 1995.

[Muriel99] M.A. Muriel, J. Azaña, A. Carballar, "Real-time Fourier transformer based on fiber gratings", Optics Letters, Vol. 24, pp. 1-3, 1999.

[Nakazawa94] M. Nakazawa, E. Yosida, Y. Kimura, "Ultrastable harmonically and regeneratively modelocked polarisation-maintaining erbium fibre ring laser", Electronics Letters, Vol. 30, No. 19, pp. 1603-5, 1994.

[Nakazawa96] M. Nakazawa, K. Tamura, E. Yosida, "Supermode noise suppression in a harmonically modelocked fibre laser by selfphase modulation and spectral filtering", Electronics Letters, Vol. 32, No. 5, pp. 461-3, 1996.

[Pendock95] G.J. Pendock, M.J.L. Cahill, D.D. Sampson, "Multi-gigabit per second demonstration of photonic code-division multiplexing", Electronics Letters, Vol. 31, pp. 819-20, 1995.

[Pfeiffer94] Th. Pfeiffer, G. Veith, "Tuneable fibre source for picosecond pulses around 1.55 μm with repetition rates up to 20 GHz", Optical and Quantum Electronics, Vol. 26, pp. 547-557, 1994.

[Pruncal86] P.R. Pruncal, M.A. Santoro, T.R. Fan, “Spread spectrum fiber-optic local area network using optical processing”, Journal of Lightwave Technology, Vol. 4, pp. 547-54, 1986.

[Shan92] X. Shan, D. Cleland, A. Ellis, “Stabilising Er fibre soliton laser with pulse phase locking”, Electronics Letters, Vol. 28, No. 2, pp. 182-4, 1992.

[Siegman86] A.E. Siegman, “Lasers”, University Science Books, California, 1986.

[Takada90] A. Takada, H. Miyazawa, “30 GHz picosecond pulse generation from actively mode-locked erbium-doped fibre laser”, Electronics Letters, Vol. 26, No. 3, pp. 216-7, 1990.

[Takara92] H. Takara, S. Kawanishi, M. Saruwatari, K. Noguchi, “Generation of highly stable 20 GHz transform-limited optical pulses from actively mode-locked Er-doped fibre lasers with an all-polarisation maintaining ring cavity”, Electronics Letters, Vol. 28, No. 22, pp. 2095-6, 1992.

[Takara95] H. Takara, S. Kawanishi, M. Saruwatari, “Stabilisation of a modelocked Er-doped fibre laser by suppressing the relaxation oscillation frequency component”, Electronics Letters, Vol. 31, No. 4, pp. 292-3, 1995.

[Teh00] P.C. Teh, P. Petropoulos, M. Ibsen, D.J. Richardson, “A 10Gbit/s, 160Gchip/s OCDMA system based on superstructured fiber gratings”, Technical Digest OFC’2000, Baltimore, postdeadline paper PD9.

[Trebino97] R. Trebino, K.W. deLong, D.N. Fittinghoff, J.N. Sweetser, M.A. Krumbügel, B.A. Richman, D.J. Kane, “Measuring ultrashort laser pulses in the time-frequency domain using frequency-resolved optical gating”, Review of Scientific Instruments, Vol. 68, pp. 3277-95, 1997.

[Tsuda99] H. Tsuda, H. Takenouchi, T. Ishii, K. Okamoto, T. Goh, K. Sato, A. Hirano, T. Kurokawa, C. Amano, “Spectral encoding and decoding of 10Gbit/s femtosecond pulses using high resolution arrayed-waveguide grating”, Electronics Letters, Vol. 35, pp. 1186-88, 1999.

[Wada99] N. Wada, K.I. Kitayama, “A 10Gb/s optical code division multiplexing using 8-chip optical bipolar code and coherent detection”, Journal of Lightwave Technology, Vol. 17, pp. 1758-65, 1999.

[Weiner88] A.M. Weiner, J.P. Heritage, E.M. Kirschner, “High-resolution femtosecond pulse shaping”, Journal of Optical Society of America B, Vol. 5, pp. 1563-72, 1988.

[Weiner92] A.M. Weiner, D.E. Leaird, J.S. Patel, J.R. Wullert, “Programmable shaping of femtosecond pulses by use of a 128-element liquid-crystal phase modulator”, IEEE Journal of Quantum Electronics, Vol. 28, pp. 908-20, 1992.

[Weiner98] A.M. Weiner, A.M. Kan’an, “Femtosecond pulse shaping for synthesis, processing, and time-to-space conversion of ulatrafast optical waveforms”, IEEE Journal of Selected Topics in Quantum Electronics, Vol. 4, pp. 317-31, 1998.

[Wey97] J.S. Wey, D.L. Butler, N.W. Rush, G.L. Burdge, J. Goldhar, “Optical bit pattern recognition by use of dynamic grating in erbium-doped fiber”, Optics Letters, Vol. 22, pp. 1757-9, 1997.

[Widdowson94] T. Widdowson, D.J. Malyon, X. Shan, P.J. Watkinson, “Soliton propagation without transmission control using a phase-locked erbium fibre ring laser”, Electronics Letters, Vol. 30, No. 8, pp. 661-3, 1994.

[Yoshida99] E. Yoshida, N. Shimizu, M. Nakazawa, “A 40-GHz 0.9-ps regeneratively mode-locked fiber laser with a tuning range of 1530-1560nm”, IEEE Photonics Technology Letters, Vol. 11, pp. 1587-9, 1999.

[Yu99] H.Y. Yu, P. Heim, F.G. Johnson, P.S. Cho, H. Mandelberg, D.R. Stone, M. Dagenais, J. Goldhar, “Programmable high-bit-rate pattern generator with a segmented optical amplifier”, Optics Letters, Vol. 24, pp. 324-6, 1999.

PART TWO

Chapter Four

Investigation of gallium as a nonlinear material

Overview: Mirrors formed at the interface of a temperature-controlled gallium bead and a cleaved fibre tip are shown to be highly nonlinear. Reflectivity changes from ~50% to ~67% are observed with the application of just a few milliwatts of optical power. The dependence of this nonlinearity on temperature and pump power is examined. The dynamics of the nonlinear effects are studied, as well as the nonlinear phase response associated with the reflectivity change. The chapter also includes a study of the reproducibility of the nonlinear effect, under continuous application of pump power.

4.1 Optical nonlinearities in metals

Over the past few years a nonlinear optical materials requirement has emerged in optics for a number of applications, including optical switching, routing and data processing. Materials like $LiNbO_3$ and $BaTiO_3$ are well known for their nonlinear properties [Boyd92]. Research in this field has predominantly concentrated on dielectrics and semiconductors, for which the response to light becomes nonlinear for intense electromagnetic fields [Klingshirn95]. Bulk metals on the other hand, have not been extensively explored in terms of their cubic nonlinearities. This is mainly because the potential contribution of free electrons, able to allow the generation of such effects is generally too small [Bennett98a].

However, it has been recently discovered that the cubic optical nonlinearities in metals such as gold and nickel reach remarkably high values. Due to the spectrally broad reflectivity properties of metals, these nonlinearities are present over a broad region of the spectrum. They were measured at the wavelength of 1260nm, using 76fs pulses, employing a technique based on the incoherent specular inverse Faraday effect, according to which specific information about the $\chi^{(3)}$ tensor can be provided by the pump-induced rotation of the polarisation azimuth of a probe wave [Bennett98a, Bennett98b, Bennett98c, Zheludev95]. In particular, by measuring the alteration of the polarisation of a probe beam reflected from the surface of a nickel sample, on which a strong, circularly polarised pump beam was applied, it was calculated that the frequency-degenerate cubic nonlinearity of nickel was $1.4 \cdot 10^{-17}$ $m^2 \cdot V^{-2}$. Interband-spin- in combination with free-electron-related mechanisms are believed to be behind the effect. Correspondingly, the nonlinearity in gold was measured to be $\sim 2.1 \cdot 10^{-16} m^2 \cdot V^{-2}$ [Zheludev95]. In this case, the nonlinearity was attributed to the saturation of a light-stimulated spin-flipping process of the free electrons of the metal.

Similar measurements were performed in indium as well. Indium melts at ~157^{o}C, and since solid and liquid phases in metals are characterised by different dielectric coefficients, resistivities and magnetic susceptibilities, the optical nonlinearity that occurs with melting was studied as well, using the same method described before. It was found that for the solid phase the cubic nonlinearity was $\sim 5.3 \cdot 10^{-17} m^2 \cdot V^{-2}$, whereas in liquid it increased to as much as $\sim 1.4 \cdot 10^{-16} m^2 \cdot V^{-2}$. Furthermore, near the melting point the magnitude of the nonlinearity increases by approximately one order of magnitude, approaching $1 \cdot 10^{-15} m^2 \cdot V^{-2}$. As in gold, the nonlinearities in the solid and liquid phase were ascribed to a spin-flipping mechanism, whereas the increase of nonlinearity on melting was attributed to the contribution of weakly bound, highly anharmonic electrons [Dhanjal97a].

However, due to the small penetration depth of light into metals the interaction length is small, and although the nonlinear coefficients of the materials mentioned above are significant, the total nonlinear response remains small. Thus, materials with even higher nonlinear coefficient are needed. In the same course of studies, gallium, which is however characterised by a peculiar structure that differentiates it from most common metals, was studied next. It appeared indeed as a good candidate, exhibiting a highly nonlinear reflectivity in the solid phase. As in indium, this nonlinearity was enhanced near its melting point of 30^{o}C, but appeared to be bigger than that of indium by several orders of magnitude [Dhanjal97b]. Encouraged by the apparently huge nonlinearity and the easily attainable melting temperature of this commonly available elemental material, and with the prospect of a new technology, we investigated the nonlinear properties of liquefying gallium mirrors extensively. Of particular interest were its integration with, and its potential applications in fibre systems.

4.2 Structural characteristics of gallium

Gallium is known to show several stable and metastable phases with different crystalline arrangements. The only stable solid phase at room temperature though, is the orthorhombic α phase. α-Ga is highly anisotropic, and has eight atoms per unit cell. It is well studied and described in [Schnering91] and [Gong91] and its lattice is based on a short distance covalent bond between two atoms. The other six gallium atoms lie further away, thus forming a stacking of strongly deformed hexagonal nets that constitute parallel planes connected by the short bonds between the first neighbour atoms (fig. 4.1). The existence of this bond is accompanied by a deep minimum in the electronic density of states (DOS) at the Fermi energy. Because of its peculiar structure it can be described either as a “metallic molecular crystal” [Gong91] or as an “inorganic polymer” [Schnering91].

Other important crystal structures are Ga-II and β-Ga, both of which are very close energetically to α-Ga and to each other. Ga-II can be obtained from α-Ga by application of external pressure. β-Ga is a metastable metallic phase, which is obtained by supercooling of liquid gallium. In both these phases the covalent bond and the DOS minimum at the Fermi energy do not exist any more, instead they exhibit a nearly free-electron behaviour [Gong91, Wolny86].

Gallium melts at 30^{o}C and can be easily supercooled to ~3^{o}C below the melting point. On melting, the covalent bond and the well-defined lattice of α-Ga are destroyed and the DOS minimum disappears, resulting in more metallic properties and free-electron behaviour for the liquid [Hafner90]. Gallium’s behaviour does not seem to change after subsequent meltings and solidifications, but does depend on the annealing temperature that it is heated to. That is, the liquid seems to have a memory of the α phase in its structure, but annealing it above 45^{o}C changes this structure towards a more β-like one, resulting in a significant decrease in the temperature at which it solidifies [Kofman79, Wolny86].

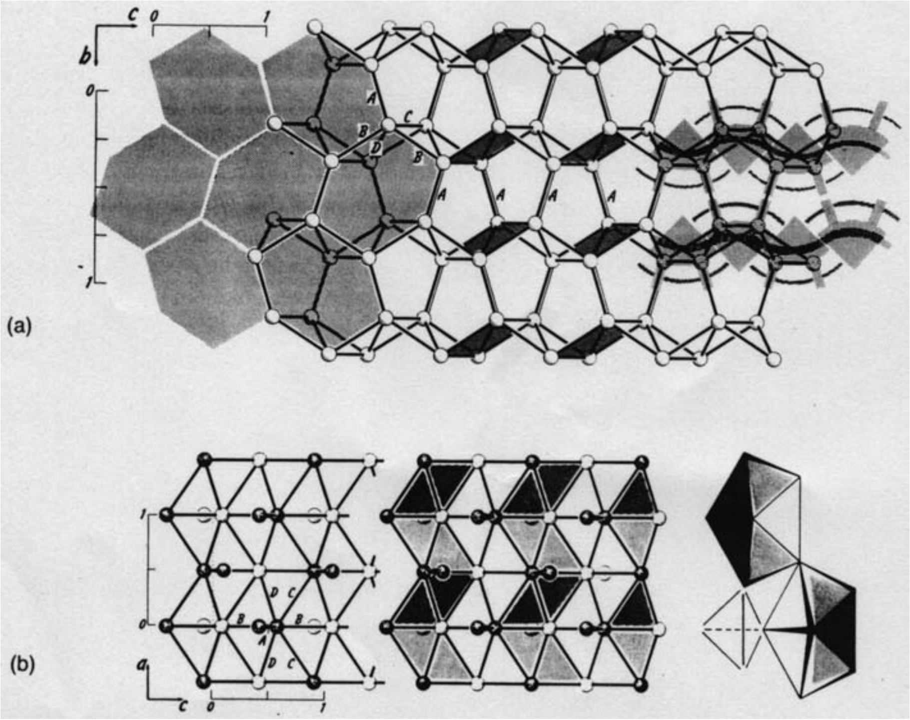

Fig. 4.1 The α-gallium structure parallel to[100] (a) and parallel to [010] (b); the strong Ga_2 covalent bonds are indicated as A (after [Schnering91])

Extensive measurements of the reflectivity of gallium and its dependence on temperature were reported in [Kofman79] and [Kofman77]. It was shown that gallium's reflectivity drastically increases on melting (decreases on solidification), and as gallium is supercooled below its melting point, the reflectivity exhibits hysteresis behaviour with temperature. These measurements were made in the spectral range 300 - 900nm.

However, it was not until recently that gallium attracted some interest as a nonlinear material. The first observation of the nonlinearity in gallium's reflectivity was reported in [Dhanjal97b]. Nonlinearities of as much as $\sim 10^{-10} m^2 \cdot V^{-2}$ ($\sim$0.01esu) were measured on a gallium:glass interface at temperatures close to the melting point, and demanded a more detailed investigation.

4.3 Optical nonlinearity in gallium

The early observations of the nonlinear reflectivity of gallium were performed at 1260nm. Changes in the reflectivity as experienced by a weak probe beam at a gallium:glass interface due to the application of a stronger pump beam, were measured as a function of the temperature. These measurements gave encouraging results, as far as the magnitude of the nonlinearity observed was concerned. However, as they were performed using continuous-wave beams, they did not allow conclusions to be drawn on the reversibility or the response time of the effect. Since nonlinearities in metals are in general broadband, the question immediately arose as to how this metal behaves at the telecommunications wavelengths. If this nonlinearity extended to 1550nm, it was argued that it could be used as the basis for a number of telecommunications applications that involve control of light by light, such as all-optical switching or routing. Moreover, the fact that the previous observations were made on a gallium:glass interface suggested that an optical fibre could be used to couple light onto the gallium sample, so as to form with it a nonlinear mirror; a possibility which if proven, would greatly enhance the range and practicality of potential applications.

A series of systematic experiments was undertaken to establish the compatibility of the material with optical fibres, to test the reversibility of the effect and to determine its speed of response. Through these experiments, a more complete characterisation and understanding of gallium's optical reflectivity near its melting point was achieved. More specifically, the parameters that were examined were the magnitude, the time response (nanosecond resolution), and the phase response of the nonlinear effect. The characterisation experiments were performed around 1550nm employing a pump-probe configuration. The implementation of this configuration constituted a fully fiberised optical switch and is described in the following section.

4.4 Experimental set-up for the investigation of the magnitude and dynamics of the nonlinearity

All of our experiments to examine and evaluate the nonlinear properties of the mirrors formed at a gallium:glass interface used a pump-probe configuration. In this configuration pump induced changes in the reflectivity of the interface were detected by a weak probe beam at a different wavelength. For this to be achieved in an all-fiberised system, a strong optical beam (pump) and a second weaker one of a different wavelength (probe) had to be combined in a single fibre and coupled onto the mirror formed at the surface of a gallium sample. On reflection the pump beam had to be filtered out completely, so that only the probe beam would be detected.

It was shown early in our experiments that liquefying gallium mirrors can indeed be fully integrated with conventional optical fibre technology. We formed the mirrors used in our experiments on the tip of a single mode fibre simply by inserting the freshly cleaved end of the fibre into a ~1mm diameter bead of initially molten high purity (nominally 99.9999% pure) gallium. Both the fibre end and the gallium bead were placed on separate translation stages, to allow precision positioning of the fibre relative to the gallium bead's surface when forming the mirror. The mirror/gallium bead was placed on top of a miniature Peltier heat pump, allowing for active control and monitoring of its temperature with a precision of ~0.01°C in the temperature range of interest 0 - 40°C. Light was coupled onto and off the gallium mirror using an optical circulator.

The complete set-up developed to examine the magnitude and dynamics of the gallium mirrors is shown in fig. 4.2. It operates as an optical switch for the probe signal λ_2, the intensity of which varies at the output, depending on the presence (or not) of the pump signal. The source used for the probe signal was a continuous wave DFB laser with 70MHz linewidth, operating at 1549nm. The power of this beam at the mirror surface was 60μW.

The pump source λ_1 was an amplified continuous-wave, narrow linewidth (~10kHz) external cavity laser operating at 1536nm. For the investigation of the magnitude of the nonlinearity, the pump beam was externally modulated using an acousto-optic Bragg cell, giving square pulses with rise/fall times of ~200ns, at any frequency up to 1MHz with controllable modulation depth and duty cycle. The peak power of the pump pulses at the mirror surface could be varied between 0 and 8mW. The fibre mode field diameter was ~12μm, allowing for a maximum pump intensity of ~7kW/cm^2 at the mirror surface. Since the modulation frequencies used in the experiments were rather low, 500Hz in many cases, the cw pump beam had to be amplified first before being modulated, to avoid any deformation of the pulse shape due to the long relaxation time of the erbium-doped amplifier. However, this method of modulating the pump proved unsuitable when the dynamics of the nonlinear effect were examined, as the slow rise/fall times of the modulator restricted the time resolution of the experiment. In order to increase the measurement resolution, the current of the pump source was modulated directly. This allowed the generation of intense square pulses, with a FWHM as short as 15ns, and at the same time avoided the excess loss of 4.5dB introduced by the modulator, allowing for higher peak intensities at the sample.

The pump beam was filtered with a temperature tuned, 3GHz fibre Bragg grating of ~90% reflectivity before being combined with the probe beam, to eliminate any amplified spontaneous emission generated by the amplifier that could extend out to the probe wavelength, thereby eliminating any cross-talk between pump and probe beams. This filtered signal was combined into a single fibre with the continuous wave probe beam by means of a 60/40 fibre coupler. Polarisation controllers were included in both input ports of the coupler to allow independent control of the polarisation for each of the beams, allowing us to determine the polarisation dependence of the effect. A fast detector was employed at the fourth port of the coupler to monitor the pump pulses.

The probe was separated from the pump beam at the circulator's third port using a 2nm bandpass filter, resulting in suppression of the pump by >30dB relative to the probe at the filter output. At the receiver end there was a choice of either an InGaAs detector with a transimpedance amplifier of a 3dB bandwidth of ~250kHz, or a faster detector of lower sensitivity with an overall detection bandwidth of 200MHz, limited

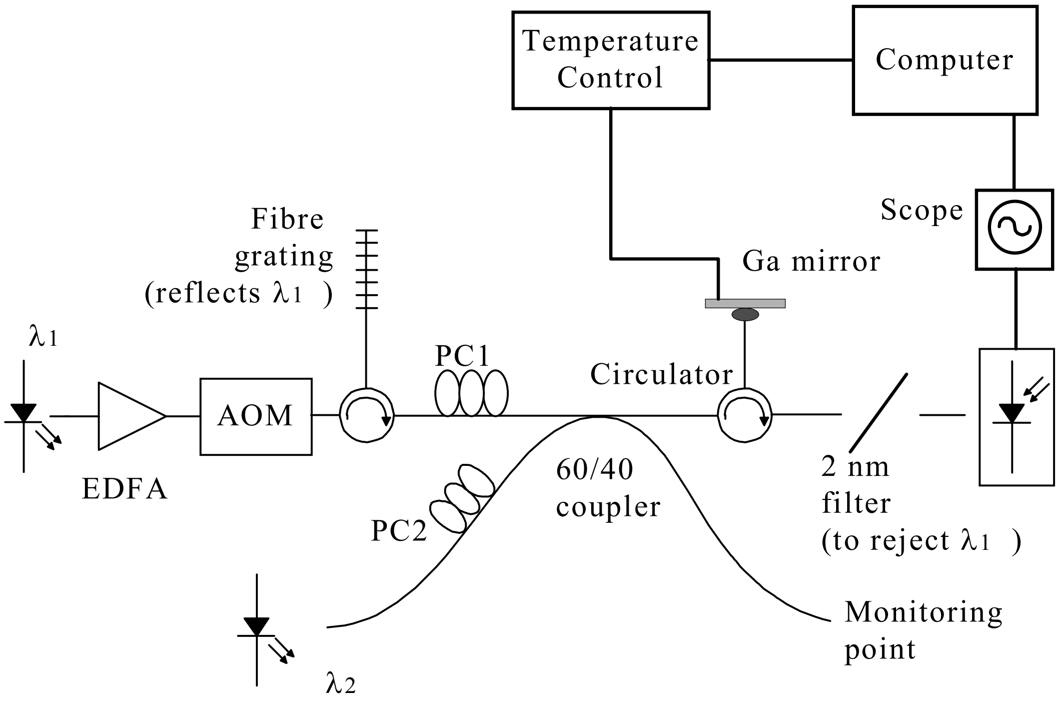

Fig. 4.2 All-optical fiberised switch for investigation of the nonlinear properties of reflectivity in gallium

mainly by the oscilloscope used. The faster detection system was used for measurements looking at the temporal dynamics of the nonlinearities. Care was taken to ensure that the measurement set-up itself (excluding the gallium mirror) was insensitive to changes in the state of polarisation of the two incident light beams. Scanning the polarisation of either of the beams and monitoring the reflection of the bare fibre end at the reception point yielded maximum variations of only ±2% of the received signal, i.e. a polarisation sensitivity of 0.09dB was achieved.

The temperature controller and digital oscilloscope were connected to a computer. Special software was developed to provide automatic temperature control and data acquisition. The program allowed us to gradually ramp the temperature up and down in user-defined steps and within user-specified limits. For every temperature, a set of measurements (rise/fall times and reflectivity levels) - and optionally a waveform - was acquired from the scope and written to a file. Full automation of the system greatly enhanced our measurement capability, making acquisition and processing of the data less time consuming, less laborious and more reliable.

4.5 Linear regime

The dependence of the reflectivity of gallium on temperature was first examined in the linear regime, i.e. when only the low intensity probe beam was applied to the mirror (no pump). To achieve this, the set-up shown in fig. 4.2 was used with the pump signal λ_1 turned off. The power of the probe beam at the fibre tip where the mirror was formed was ~60μW, which corresponds to a field intensity of the order of 10^2W/cm^2. Measurements were carried out for mirror temperatures around gallium's melting point (~30^{o}C), in the range between 19 and 32^{o}C. Calibration of the measured figures to absolute reflectivity levels was performed by replacing the gallium mirror with a conventional 100% reflector (dielectric mirror) with the fibre end butted to it. The results are presented in fig. 4.3.

The reflectivity of gallium in the solid phase remains constant with changing temperature, until the melting point is reached. On melting, a sudden increase in the reflectivity level is observed, due to the strong change in the electronic density of states. Gallium supercools at around 3 degrees below its melting point, and at solidification a similar drastic change is observed, resulting in a hysteresis curve of reflectivity versus temperature, like those shown in fig. 4.3a. This effect had been observed by earlier workers in [Kofman79] and [Dhanjal97b], who used wavelengths in the range 300 - 900nm and 1260nm respectively. It has now also been verified that the same hysteresis behaviour can be observed over the whole spectral range from 550 to 1650nm at least [Albanis99a].

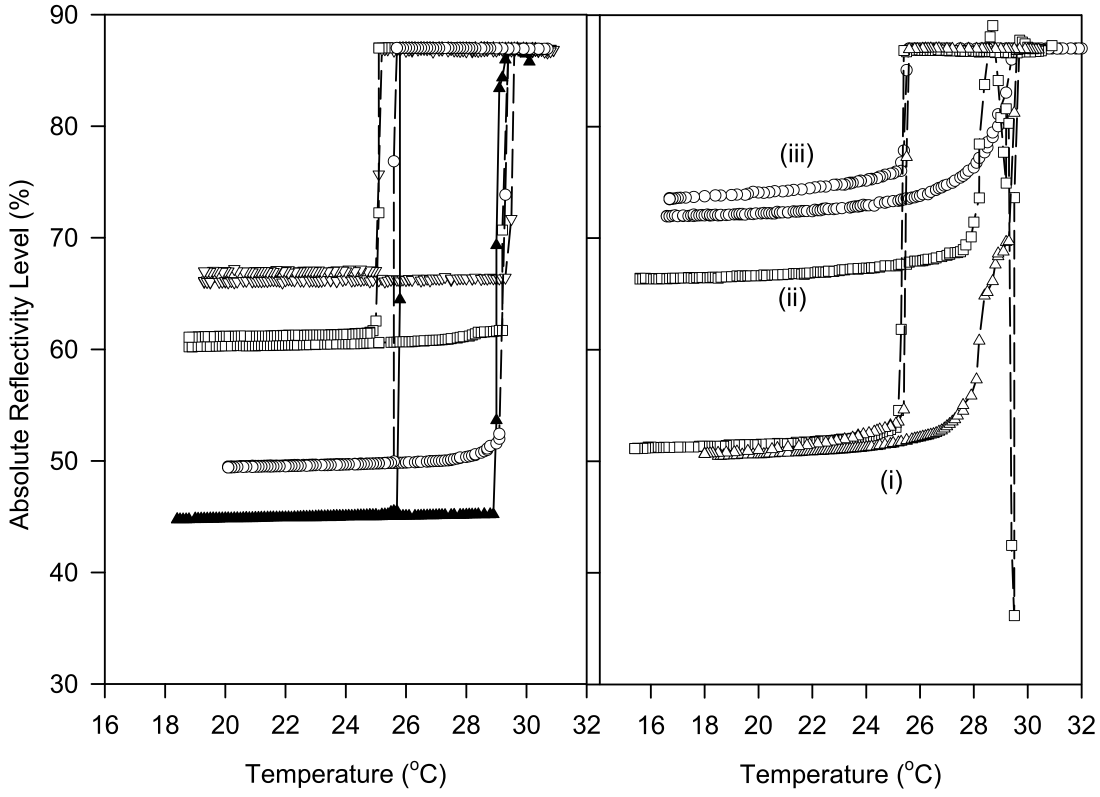

(a) (b)

Fig. 4.3 Linear reflectivity in gallium against temperature, showing (a) variation of the solid reflectivity levels from ~45% to ~68% for incident beams of different states of polarisation, and (b) reflectivity profiles of contaminated samples; a two-stage transition from solid to liquid phase (i), an abrupt drop of the absolute reflectivity just before melting (ii), and a smooth, continuous transition (iii) are shown

The reflectivity of liquid gallium at 1.55µm was measured to be approximately 87%, regardless of the state of polarisation of the incident beam. However, in the solid phase, since α-gallium is anisotropic, the reflectivity depends on the orientation of the gallium crystallite at the interface and the polarisation of the incident beam. The reflectivity in solid α-gallium phase was found to vary from ~47% to as much as 70% depending on the polarisation (see fig. 4.3a). During the course of our nonlinear experiments we always adjusted the probe beam polarisation to give minimum reflectivity in the solid phase. Although some variation in the reflectivity level was observed from solidification to solidification for fixed probe polarisation, in most cases it would return to the previous level. This is in accordance with the observation made in [Wolny86], that after melting gallium seems to retain a memory of the phase and orientation it was previously in.

It should be noted that not all mirrors that were tested exhibited such a well-defined behaviour. In particular, there were cases where the transition from low to high reflectivity level was not as sharp or showed unusual features such as a two-stage transition from solid to liquid reflectivity level (see e.g. fig. 4.3b). This was mainly observed when the gallium samples had been removed from their original container for a rather long period before being used, and hence was attributed to contamination of the gallium bead. Such samples had a poor nonlinear response, both in terms of magnitude and speed, and thus care was taken to ensure that we used only fresh, uncontaminated samples for the switching experiments.

4.6 Magnitude of the nonlinearity

The magnitude of the optically induced nonlinearity on gallium mirrors was studied next. Changes in the reflectivity level of the probe beam under excitation of a pump signal of constant average power were monitored at temperatures approaching gallium's melting point. Also, the dependence of the magnitude of the induced reflectivity change on pump intensity was explored. These are described in the following subsections.

4.6.1 Variations of optically induced nonlinearity with temperature

When a higher power beam is applied to gallium, its reflectivity profile changes significantly from that described earlier. Fig. 4.4 shows how the hysteresis curve is deformed (as monitored by a weak probe beam) in the presence of a continuous wave pump beam of power 5mW (corresponding to pump intensity of 4.5kW/cm^2). The transition from a low to high reflectivity level near the melting point is no longer as sharp, but occurs in a smoother manner across a wider range of temperatures. A smoother transition from high to low reflectivity level can be observed at solidification as well, though it is usually not as pronounced there as at melting. The effect is often followed by a drop in the absolute reflectivity to very low values, at a few tenths of a degree below the melting point (fig.4.4b).

Fig. 4.5a shows the reflected probe intensity as a function of time for a temperature of ~27°C, i.e. ~3°C below melting, in the presence of the 500Hz square wave modulated 7mW peak power pump beam shown in fig. 4.5b. It is important to note here that the induced changes in reflectivity are fully reversible and occur only when the optical

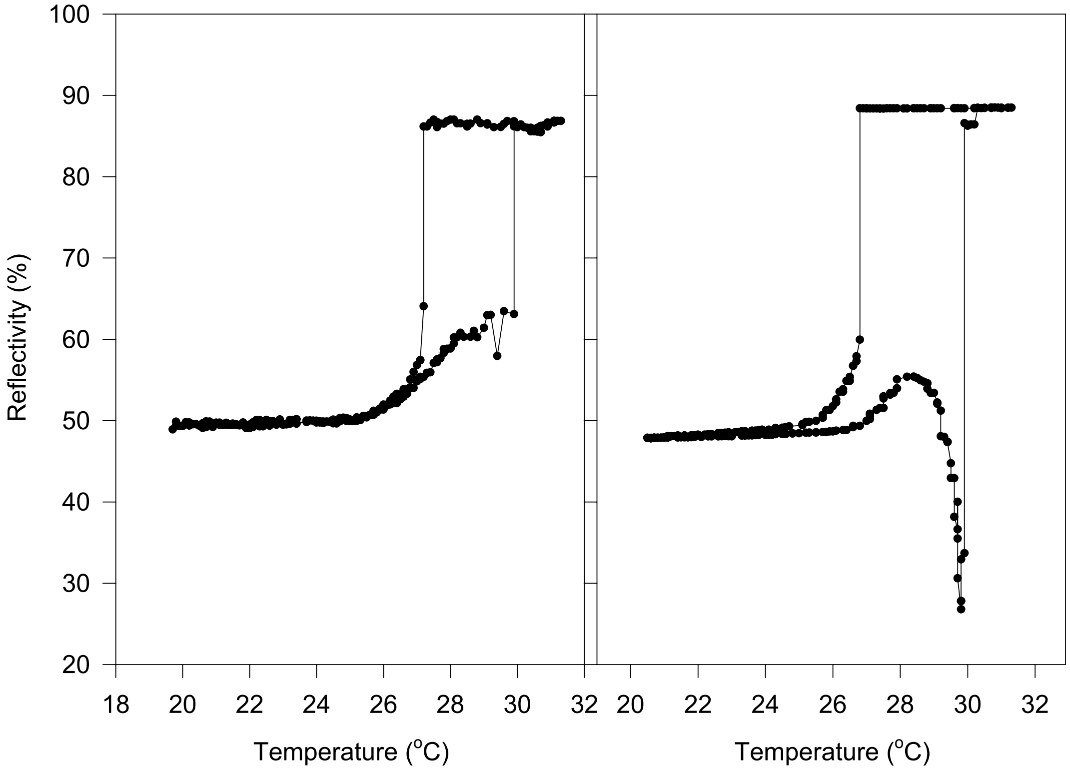

(a) *(b)*

Fig. 4.4 Typical reflectivity of gallium against temperature in presence of a 5mW pump signal; (b) shows a trough in the absolute reflectivity, that is often observed at temperatures just below the melting point excitation is applied, rapidly returning to the original level, when excitation is removed and suggesting a high-speed response. This fact is extremely important for potential applications of the nonlinearity. Note that this set-up exhibits the basic operation of an all-optical switch, where an optical signal - the pump in this case - is used to control the intensity of another beam, i.e. the probe. Ignoring for the moment the constant reflectivity level of solid-phase gallium, the probe signal can be considered to be switched on when pump excitation is present, and off when it is absent.

The nonlinearity results in changes of the reflected light intensity by as much as 30% relative to the reflected light intensity in the solid phase, as shown in fig. 4.5. Given that the pump intensity is of the order of just a few kW/cm^2 and the effective interaction length within the gallium bead is estimated to be only ~25nm (the skin depth), this represents a remarkable amount of nonlinearity (see Section 4.10).

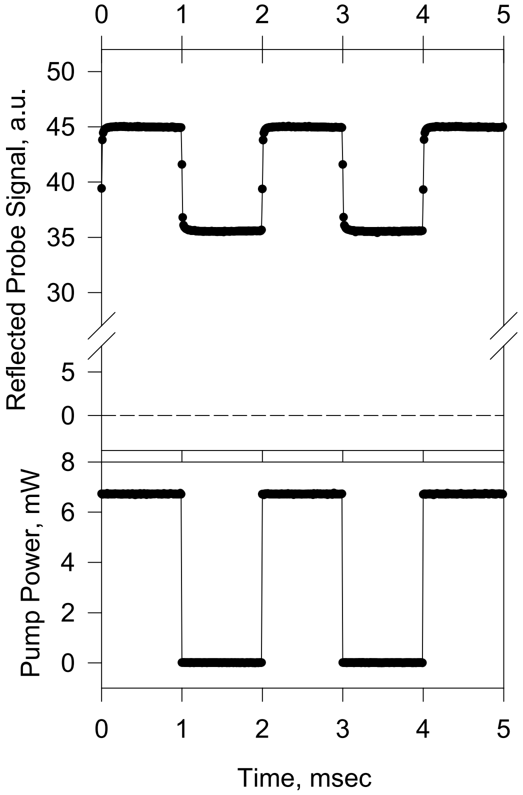

Fig. 4.5 (a) Reflected probe power as a function of time in the presence of the (b) 7mW peak power pump pulses; The pump pulse frequency was 500Hz and the pulses were of 50% duty cycle and 100% modulation depth

The strength of the nonlinearity was next investigated as a function of temperature (for a fixed pump power). The nonlinear response is fairly small for temperatures below 20 - 22°C, but increases significantly in the fashion shown in fig. 4.6 for higher temperatures until ~1°C below the melting point. Note in fig. 4.6, that output modulation depth is defined as the ratio of the change in the level of reflectivity of the excited state to the reflectivity level of the non-excited state and represents an objective measure of the induced change due to the nonlinearity. This definition will be used throughout.

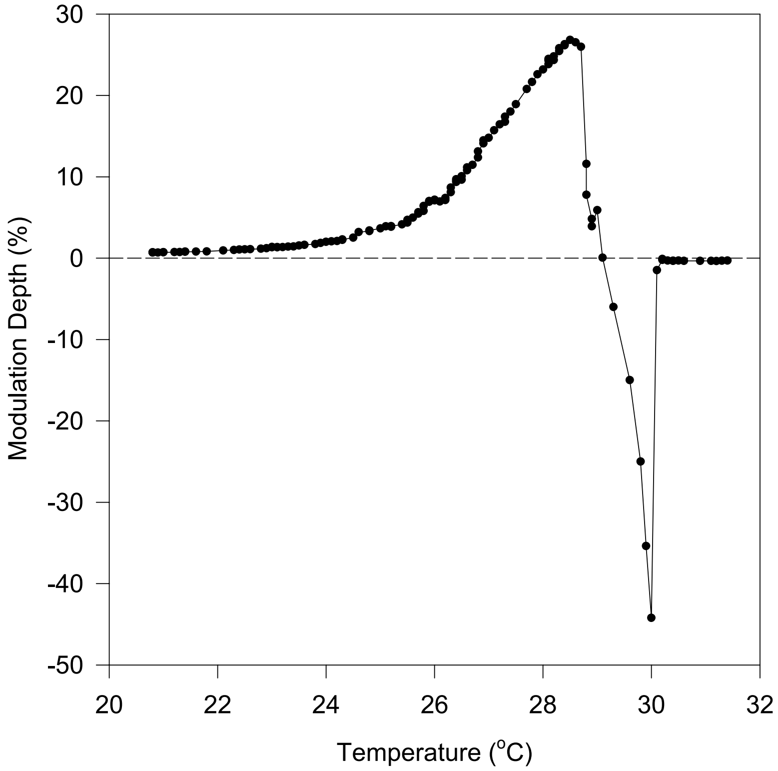

Fig. 4.6 Typical output probe modulation depth as a function of temperature for a pump with 50% duty cycle, frequency of 500Hz and 4.7mW peak power

At temperatures very close to (within ~1°C) and below the melting point, the induced reflectivity becomes complicated; it seems that two nonlinear components with opposing effects and different response times are competing each other, resulting in a complex pulse response. In fig. 4.7 we show the induced response within this regime, where it is seen that the reflectivity initially increases rapidly as at lower temperatures, before falling away as the slower, stronger component of the response of opposite sign takes over effect. This eventually leads to reversal of the sign of nonlinearity as the melting point is further approached, i.e. the reflectivity is reduced as pump power is applied (see fig. 4.6). The magnitude of these changes is usually very large, but has a much slower response time than the fast component, of the order of 10^{-4}s. This inverted nonlinearity could prove very useful in applications such as optical noise reduction or power limiting. However, this effect tends to disappear after the mirror has been exposed to high optical power for several hours.

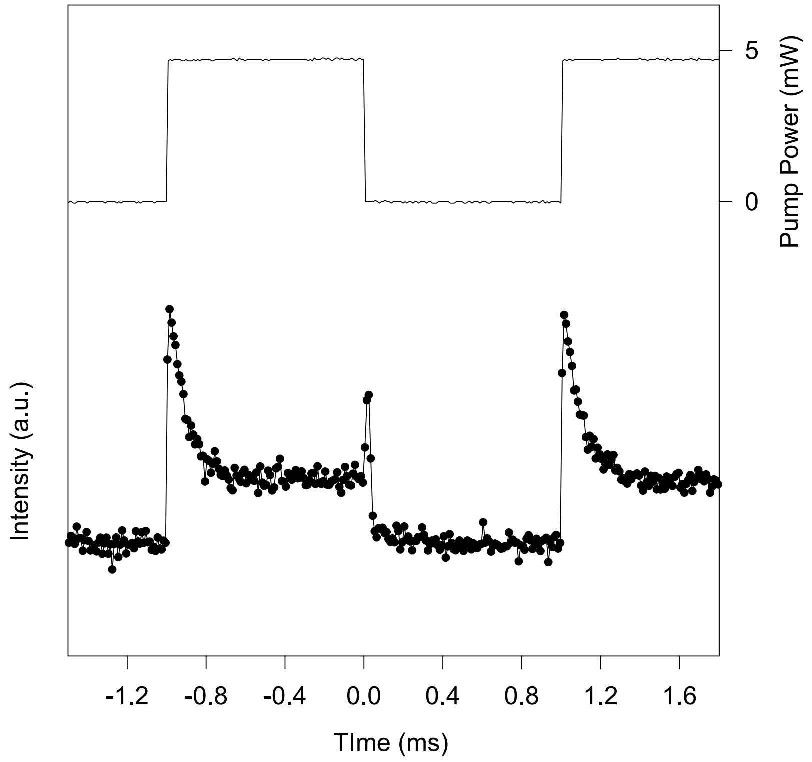

Fig. 4.7 Nonlinear response at a mirror temperature of 29.0^{o}C (bottom trace) induced by a square wave modulated pump of 4.7mW peak power (top trace)

Finally, we note that all nonlinear effects vanish abruptly once the sample melts and absolute reflectivity increases up to ~87% regardless of the pump power. On subsequent recooling nonlinear behaviour is fully restored after solidification.

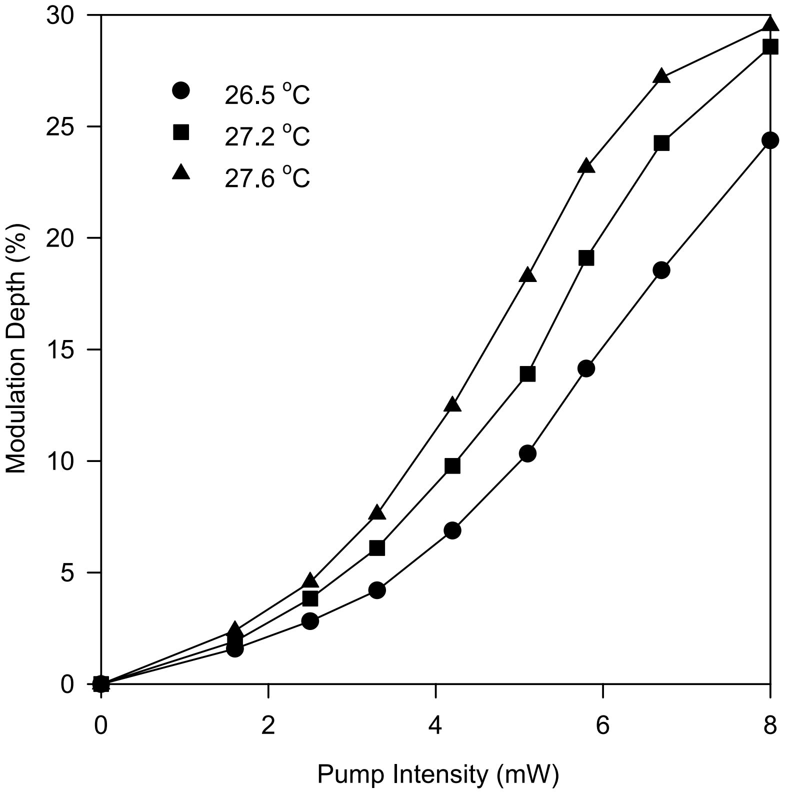

Fig. 4.8 Output probe modulation depth as a function of peak pump power for pump pulses at a modulation frequency of 500Hz, 100% modulation depth and 50% duty cycle for a number of different mirror temperatures

4.6.2 Pump intensity dependence

The induced modulation depth was also measured as a function of the pump intensity applied to the gallium mirror for a number of different mirror temperatures. Square-wave pump signals of a peak power varying from 0 to 8mW were used. The measurements were performed by gradually heating the gallium mirror from 23°C up to just above the melting point, under application of a pump beam of a certain intensity. The induced modulation depth was measured at several temperatures. Then, the mirror was taken back to the initial temperature of 23°C, and the procedure repeated for a higher power pump beam – and so on. The results of the measurements are shown in fig. 4.8. As one would expect, as the melting point is approached the nonlinearity builds up and the amount of power required to achieve a certain modulation depth decreases. The dependence on pump power is not linear and the induced modulation depths tend to saturate for higher powers. At powers significantly higher than those required to reach the maximum nonlinear response, some distortion of the switched signal could be observed. This was particularly apparent close to the melting point. Fig. 4.9 shows such a distorted signal acquired for a mirror temperature of 28.2^{o}C and a pump signal of peak power 8mW. A second, slower component seems to become dominant in this regime, resulting in a rather deformed pulse shape.

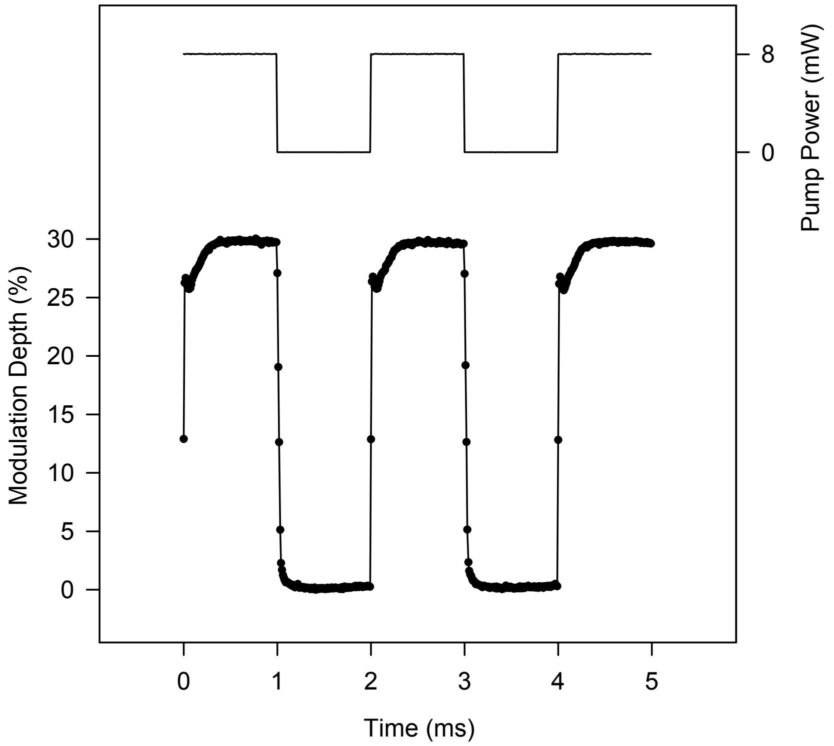

Fig. 4.9 Typical modulated probe signal (bottom trace) under square wave modulated pump of 8.0mW peak power (top trace) at 28.2oC; pulses are distorted due to high pump power

Additional experiments were performed, in which the pump signal was externally modulated to follow a slowly varying triangular (fig. 4.10a) or sinusoidal waveform (fig. 4.10b). Comparison between the rising and falling edges of the switched signal revealed that the nonlinearity exhibits bistable behaviour: the material has some kind of memory of whether the optical power is rising or falling, which results in the shape of the power dependence being different for increasing and decreasing pump power. This is shown in fig. 4.11 for the case of a sinusoidal pump signal, where the induced modulation depth versus pump power is plotted for a mirror temperature of 25^{o}C.

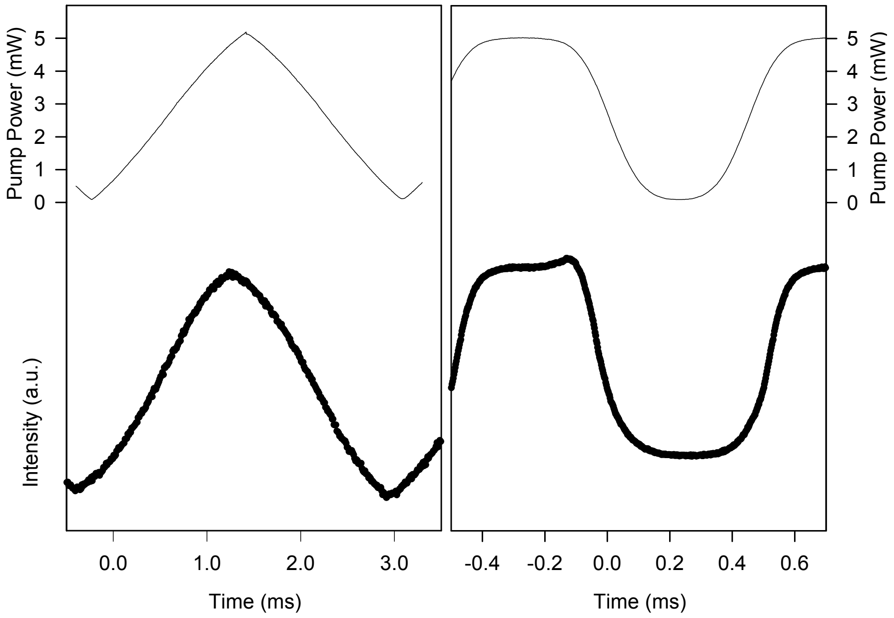

(a) (b)

Fig. 4.10 Induced modulation of the reflectivity of the probe signal (bottom traces) in presence of a pump beam which follows (a) a triangular or (b) an approximately sinusoidal waveform (top traces);the mirror temperature is 25°C in both cases

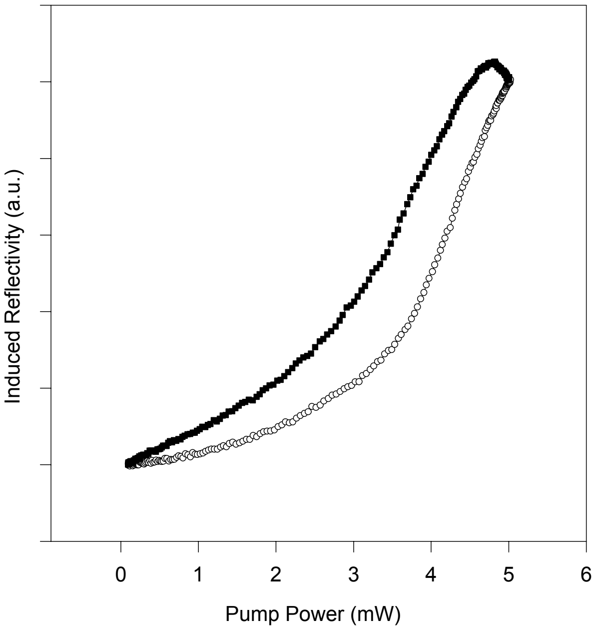

Fig. 4.11 Induced reflectivity against pump power for a pump signal modulated to follow a sinusoidal waveform for a mirror temperature of 25°C; circles indicate increasing pump power and squares indicate decreasing pump power

4.7 Dynamics of the nonlinearity

The response time of the nonlinearity was first examined using square pulses, similar to those used in the experiments reported in the previous section. More detailed analysis followed, which used short (15-100ns), more intense pulses. The dynamics of the nonlinearity was examined in this regime for various temperatures, pulse peak powers and widths, revealing the energy-dependent nature of the nonlinearity.

4.7.1 Frequency response

Initially, in order to determine the time dependence of the observed nonlinear effect, the rise and fall times of the response to the long square pump pulses of 200ns turn-on/turn-off times were measured. This was done using an 1 GHz detector with a 200MHz sampling oscilloscope (see section 4.3). The measurements were carried out ~3°C below the melting point, where the nonlinearity peaks in terms of induced reflectivity change. Fig. 4.12 shows the rising and falling edges of the response to pulses with 5mW peak pump power. Analysis shows that the time constant of the rising edge is approximately ~4.7μs. Correspondingly, the falling edge shows a

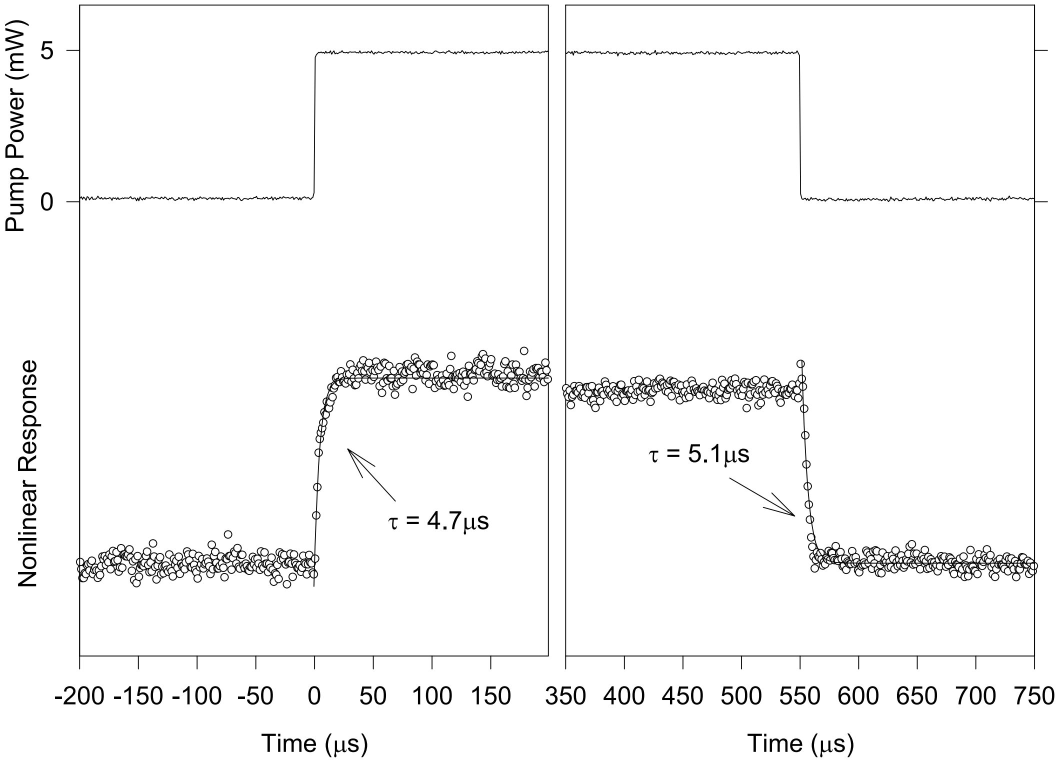

Fig. 4.12 Switching effect in gallium sample at ~3°C below the melting point induced by 5mW of pump power (top: pump signal - bottom: nonlinear response at probe signal)

response time of ~5.1μs. However, at lower temperatures, where the magnitude of nonlinearity is reduced, these figures are also reduced. For example, at 25.5°C the response time for the rising edge is ~3.8μs, and for the falling edge ~1.3μs.

In addition, further frequency response information was obtained by varying the repetition frequency of a square wave pump and monitoring the resulting induced response. These measurements were performed over the same temperature range as previously, and for a number of peak pump powers, spanning the range 3 to 8mW. They showed a 3dB bandwidth of ~200kHz (fig. 4.13), independent of the pump power, and only dependent on the mirror temperature. The effect had a somewhat higher bandwidth at lower temperatures.

These figures were indicative of the magnitude of the achievable response times and though they might be a limiting factor for applications in fast optical switching, they do indicate a reasonably fast effect, particularly once the size of the nonlinearity is

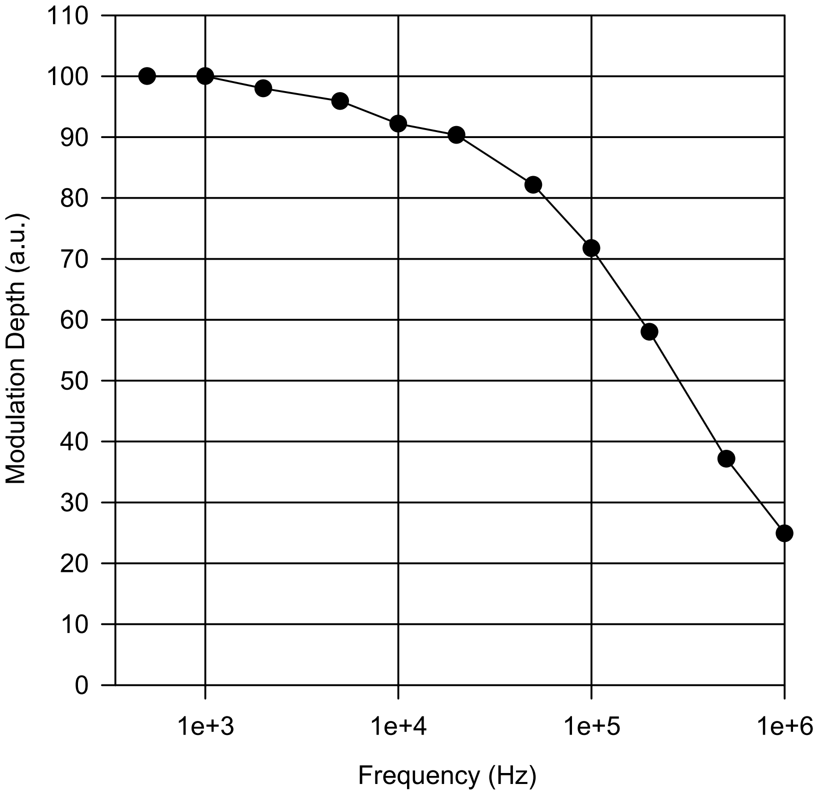

Fig. 4.13 Output probe modulation depth as a function of pump modulation frequency at a fixed pump power of 8.0mW, 100% modulation depth and 50% duty cycle; the mirror temperature is 27.5°C

considered.

4.7.2 Study of the nonlinear response in the nanosecond regime

In order to gain further information, a more detailed study dedicated to understanding the dynamics of the observed nonlinearity in liquefying gallium was necessary. These experiments were needed both from a characterisation standpoint and to assist our understanding of the origin of the effect. For this purpose, the response to short pulses was examined. The limiting factors for executing such an experiment were in our case, a finite speed source and a limited bandwidth detection system. Thus, square pulses of 15 to 100ns width were used to study the nonlinearity dynamics in the nanosecond regime. These pulses were obtained by directly modulating the current of the DFB laser used to seed the pump beam (see section 4.4). A low repetition rate was necessary to ensure that the nonlinearity induced by a single pump pulse had relaxed completely before the appearance of another pulse on the mirror. The repetition rate used in our experiments was 10kHz. The use of a lower repetition rate was restricted by the electrical signal generators available with nanosecond resolution, and the bias tee used to interface to the diode. However, it was proven in the course of the experiments that this was acceptable for our purposes. Pulses of a peak power as high as 80mW with a duty cycle as low as 0.1% were achievable at the gallium mirror. The 200MHz detection set-up was used to measure the induced reflectivity changes.

Fig. 4.14 shows the temporal response dynamics at a given temperature for different pump pulse characteristics: Fig. 4.14a shows responses to 100ns pulses of different peak powers and fig. 4.14b shows responses to pulses of the same peak power, namely 50mW, but of different durations. The induced reflectivity change increases with the pulse duration. One should notice that the rate at which reflectivity increases depends directly on the pulse peak power; the positive slope is the same for pulses of the same peak power (fig. 4.14b), whereas the duration (and amplitude) of the reflectivity increase corresponds to the pulse duration, i.e. in proportion to the energy delivered to the surface. It can thus be inferred that the rise time of the effect is of the order of ~1ns, at most. Actually more recent experiments conducted with even narrower pulses have confirmed these findings, and carried on to show a rise time as little as ~2ps ([Luther-Davies00], see also Chapter Six).

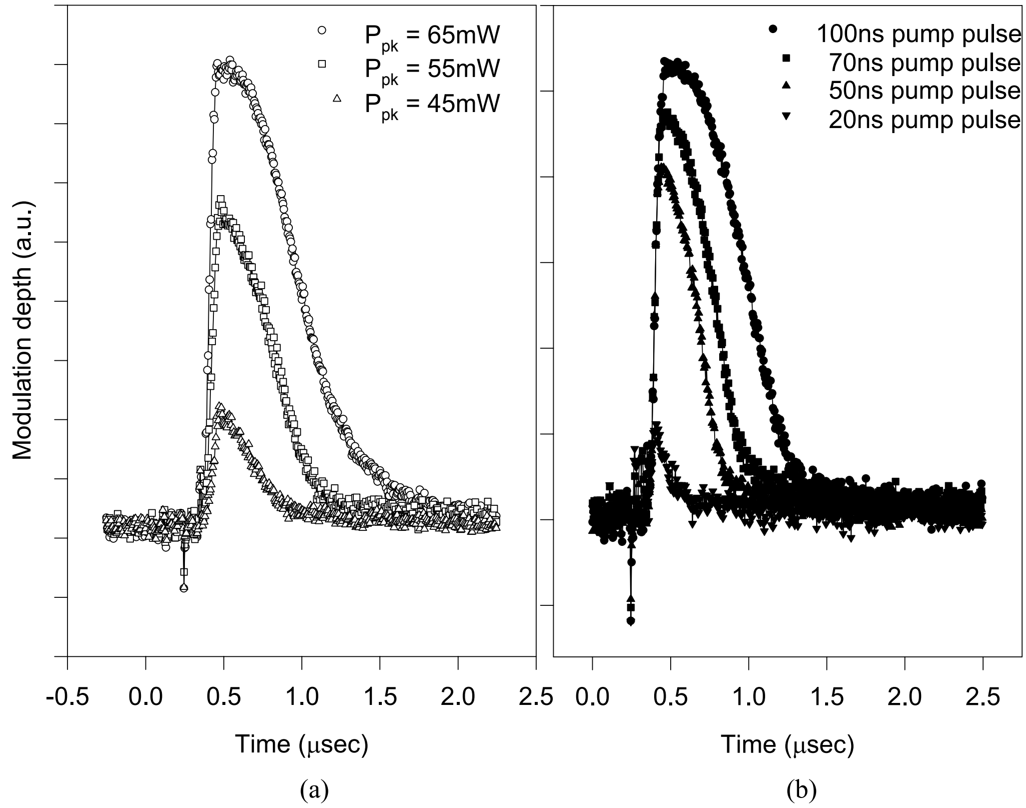

Fig. 4.14 (a) Nonlinear response to a 100ns square pump pulse for various pulse peak powers; (b) nonlinear response to a square pump pulse of 50mW peak power for various pulse durations; both cases correspond to a mirror temperature of 26.8^{o}C

The relaxation curves in fig. 4.14 seem to consist of more than one component and cannot be approximated by a single exponential decay curve. The relaxation time changes significantly with temperature, varying from a few tens of nanoseconds for temperatures 10 - 15^{o}C below the melting point T_m to as much as 3μs just below it (fig. 4.15a). This dependence of the relaxation time on temperature is shown in fig. 4.15b, where responses to pulses of variable durations are shown. In every case, the relaxation times are proportional to $1/(T_m - T)$. The significance of this observation for the understanding of the process behind gallium's nonlinearity is discussed in section 4.10.

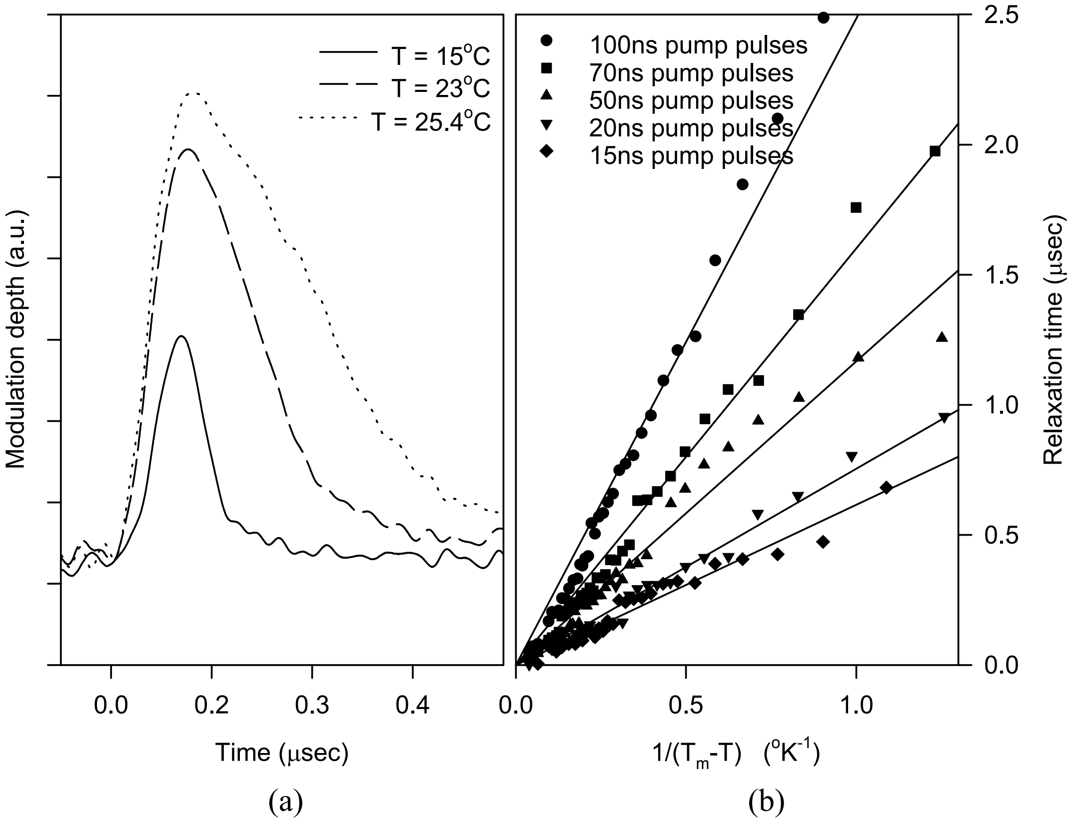

Fig. 4.15 (a) Nonlinear response to a 100ns square pump pulse of 70mW peak power at various temperatures; (b) induced reflectivity recovery time as a function of temperature near the melting point for square pump pulses of 50mW peak power of different pulse durations

4.8 Phase response of the nonlinearity

The discussion on the nonlinearities that have been observed at the interface of bulk gallium with glass has so far been engaged with the investigation of the nonlinear refractive index as a real entity only. However, a complete characterisation of the nonlinearity at the given wavelength (1550nm) should investigate the induced changes in the complex refractive index as a whole, i.e. it needs to account for the nonlinear change in the optical phase on reflection from the interface.

In order to achieve this experimentally, the basic fiberised pump-probe configuration of fig. 4.2 was employed, but adapted into an interferometric configuration as shown in fig. 4.16. The Mach-Zehnder fibre interferometer was formed with fused tapered couplers between the couplers 1 and 4. The source to the interferometer was a continuous wave DFB laser probe operating at λ_2 = 1549nm (same as in fig. 4.2). The

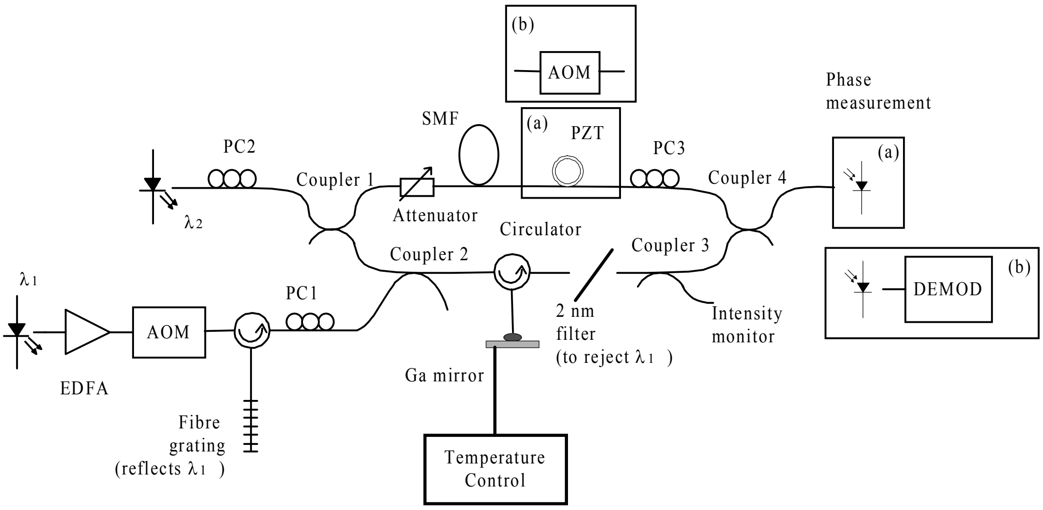

Fig. 4.16 Schematic of the Mach-Zehnder fibre interferometer, showing (a) the set-up for homodyne signal processing, and (b) heterodyne signal processing

pump source, as in the optical switch of fig. 4.2, was an amplified, externally modulated (with an acousto-optic modulator) DFB laser diode operating at λ_1 = 1536nm. Excess noise due to ASE of the amplifier was filtered out using a strong 3GHz fibre Bragg grating. The pump was introduced (via coupler 2) and extracted (from the 2nm bandpass filter) within the signal arm of the interferometer. This enabled the simultaneous monitoring of the intensity of the reflected nonlinear signal together with the measurement of the phase at the interferometer output. Monitoring of the probe signal intensity reflected off the mirror was facilitated by the use of coupler 3, which was placed just before the output of the interferometer.

Initially, a homodyne signal processing technique was chosen for the measurement of the optical phase. This involved the introduction of a length of fibre coiled around a piezoelectric phase controller (PZT) in the reference path of the interferometer (fig. 4.16a). The PZT was suitably modulated at a certain frequency close to one of its resonances. Consequently the fibre coiled around it was stretched periodically, and caused a modulation of the phase of the detected signal at the interferometer output between -π and π. The phase changes due to the nonlinearity of the gallium mirror were then added upon this modulation signal (see section 4.7.1 below). Unfortunately, these measurements showed that the nonlinear phase response was rather small, close to the sensitivity limit of the set-up, necessitating the use of a more sensitive technique. Subsequently, these measurements were only used as a pilot study for the characterisation of the phase response of the nonlinear gallium mirrors. For a more detailed study, the PZT was substituted by an acousto-optic modulator, which modulated the phase of the optical beam in the reference path (heterodyne processing, see fig. 4.16b). This modulation occurred in a linear rather than a harmonic fashion now, hence producing a more sensitive output with respect to small changes of the phase. In this case, the detected signal was fed into a demodulator (DEMOD), which directly produced an analogue output that corresponded to the detected phase (see Section 4.7.2 below).

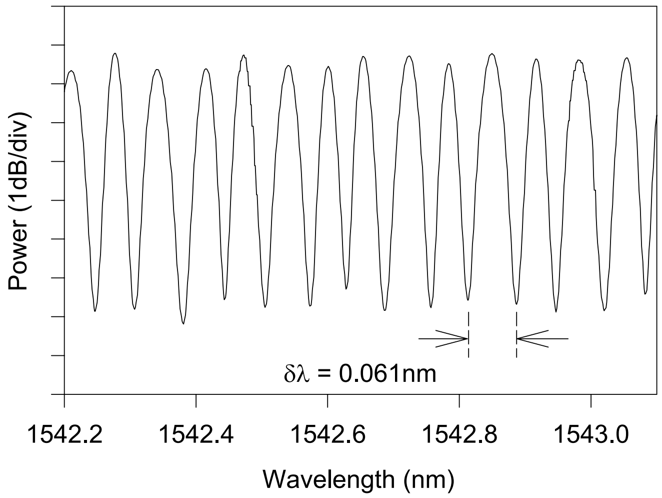

Fig. 4.17 Evaluation of the imbalance in length of the two arms of the interferometer with an optical spectrum analyser

The linewidth of the source of the interferometer (probe) was 70MHz. This corresponds to a coherence length of $\Delta l_c = \frac{c}{\pi \cdot \Delta \nu} = 1.4m$, and the imbalance between the lengths of the two paths of the interferometer has to be a small fraction of that, in order to ensure that the beat noise of the source does not give any significant contribution to the detected signal. For this purpose an extra length of fibre, the length of which was carefully chosen to balance the interferometer, was introduced in the reference path. The imbalance between the two paths was evaluated by measuring the periodicity of the spectral fringes at the output of the interferometer, when an incoherent wideband source was used at its input. This wideband source in our case was an ASE source, filtered with a 0.5nm fibre Bragg grating and amplified with a second EDFA. For the case of the homodyne detection scheme the fringes were detected with a high resolution optical spectrum analyser, and had a periodicity of

0.061nm (fig. 4.17). This corresponds to a length imbalance of [Hecht98] $\Delta L = \dfrac{\lambda^2}{n \cdot \delta\lambda} = 26mm$. Such a measurement could not be performed in the case of the heterodyne detection scheme. This was for the practical reason that the acousto-optic modulator had to be modulated during the measurement, thereby distorting the measurement in the optical domain. Instead, a known length of fibre was temporarily introduced in one arm of the interferometer, and the imbalance was determined by measuring the spectral fringes (which occurred at a much higher periodicity now) with an RF spectrum analyser. The departure of the measured length difference from the extra length of fibre would give then the imbalance in the interferometer. This measurement eventually showed an imbalance of 14mm.

Finally, it is worth mentioning that the splitting ratios of the couplers were chosen, such that the power in the two arms was balanced, and hence the visibility at the output was optimised. The attenuator was introduced in the reference path for the same reason. The splitting ratios for the couplers 1,2,3 and 4 were 90:10, 70:30, 60:40 and 99:1 respectively. The polarisation controller in the reference arm (PC3) was used to align the polarisations of the combined fields.

It has to be appreciated that due to the particularities of our interferometer design each of the arms of the interferometer was ~16.5m long. This fact increases the contribution of any temperature fluctuations to the phase measurement, resulting from an imbalanced change in the optical length of the two paths. This manifests itself in the phase detection as a low frequency noise drift. Mechanical vibrations are also another potential source of noise. In order to minimise these factors, an isolating enclosure was set-up for the whole arrangement, providing a homogeneous environment for the interferometer and greatly improving the system stability.

In the following sections, detection issues for the two configurations (homodyne and heterodyne processing) are more closely examined and the results that were obtained with each processing scheme are presented.

4.8.1 *Homodyne* detection

The simplest of the interferometric processing techniques, in terms of implementation, are the homodyne schemes [Jackson89]. In these schemes, the optical frequencies in the interferometer arms are always equal, and any phase modulation applied on the reference signal of the interferometer originates from modulation of the optical length. Such a scheme was implemented in our set-up by introducing a PZT in the reference arm of the Mach-Zehnder interferometer (fig. 4.16a). In our case, and in order to minimise the effect of any low frequency noise signals, the reference signal was modulated at a carrier frequency of $\omega_m = 24.1\text{kHz}$. This frequency was chosen, as it was close to a resonance of the particular PZT that was used. Then, the induced phase modulation $\Delta\phi(t)$ and the power P_o received at the output of the interferometer can be expressed as [Jackson89]

$$\begin{aligned}\Delta\phi(t) &= \pi\cdot R\cdot\cos(\omega_m\cdot t)\\ P_o &= P\cdot(1+V\cdot\cos(\Delta\phi(t)+\phi_S(t)+\phi_N(t))\end{aligned} \qquad \text{Eq. 4.1}$$

where the factor πR represents the modulation depth applied to the PZT and P is a power factor; $\phi_S(t)$ is the desirable phase signal arising from the nonlinearity of the gallium mirror, and $\phi_N(t)$ is the contribution of any noise sources, which is interpreted at the output as a phase bias. V is the visibility of the interferometer, and defined as

$$V = \frac{P_{\max} - P_{\min}}{P_{\max} + P_{\min}},$$

where $P_{\max}$ and $P_{\min}$ are the maximum and minimum values respectively that the output power can take as the relative phase difference between the two paths of the interferometer changes. For our measurements this number was optimised, for the case that the gallium mirror was in solid phase, to 0.91, by adjusting the attenuation within the reference path. It has to be appreciated though, that this number decreases as the reflectivity of the mirror increases due to the nonlinearity. Going back to first principles, one can easily calculate that the visibility decreases to 0.86 for a reflectivity change of 30%.

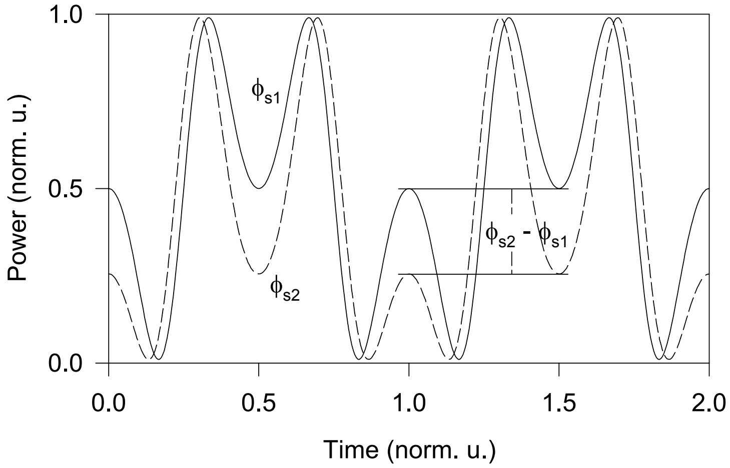

Fig. 4.18 Calculated plots showing the response of the homodyne interferometer to $\phi_{s1} = \pi/2$ rad (solid line) and $\phi_{s2} = \pi/3$ rad (dashed line)

Calculated plots showing the evolution of P_o with time for two values of ϕ_S are presented in fig. 4.18, for a phase modulation between $-\pi$ and π. It can be seen that ϕ_S can be determined from a measurement of the intensity level of the local minima or maxima, which for the case of a 2π phase modulation, coincide. It is also worth noticing that this technique gives maximum sensitivity for a phase bias of $\pi/2$ [Jackson89] and care was taken that all our measurements were taken around that point.

In order to assess the resolution limit of our measurements, the circulator and gallium mirror at the signal path were replaced by a second PZT, with the length of fibre wound around it made equal to the total length of the fibre on the three arms of the circulator, i.e. same path length mismatch. This showed that the minimum detectable phase change was 0.056rad (3.2^o). Also, measurements of some known phase change imposed on this second PZT gave a measurement uncertainty of 0.026rad (1.5^o) - see fig. 4.19.

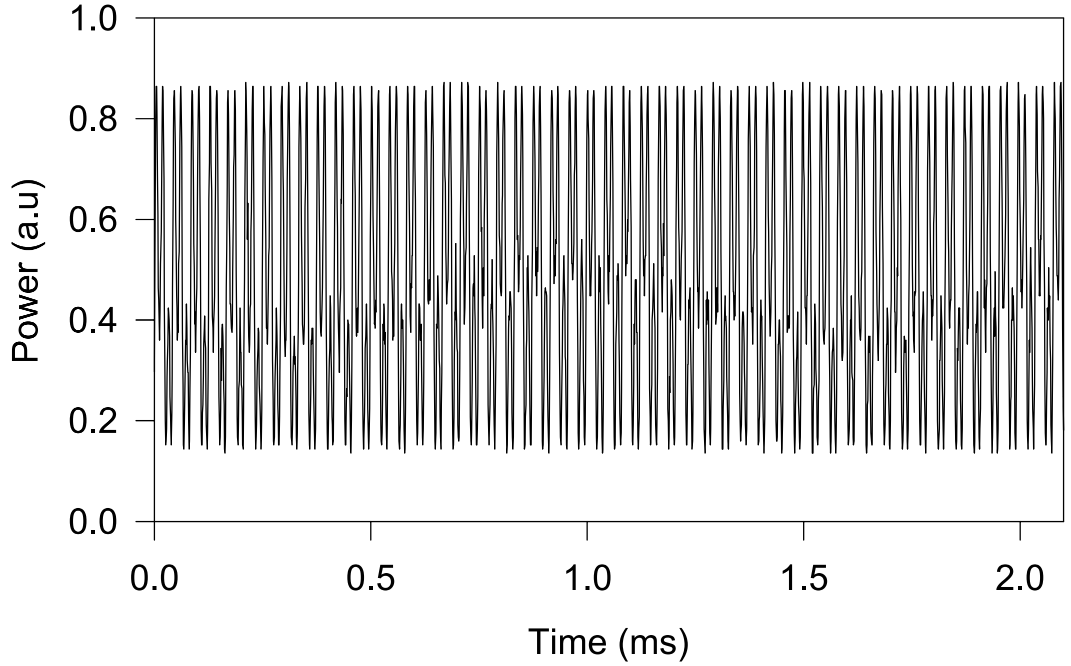

Fig. 4.19 Response of the homodyne interferometer to a sinusoidal signal imposing a phase change of +/- 0.175rad with a repetition rate of 500Hz

For the assessment of the phase response of the nonlinearity, ϕ_S was evaluated as the relative optical phase difference between two time intervals, one with and the other without optical excitation on the gallium mirror. This was achieved in the same manner as that described in Section 4.5, i.e. by applying 500Hz square pump pulses of peak power ~ 5mW to the mirror. The power of the cw probe beam was held at ~ 100μW (too low to give rise to any nonlinear effects). The probe signal received at the output of the interferometer is shown in fig. 4.20b for a mirror temperature of 27.0°C, and is compared to the reading of the probe intensity monitor (fig. 4.20a). The region of nonlinear reflectivity can be easily distinguished by the change in visibility (due to the change of the intensity at the signal path) and the change of the level of the local minima and maxima. The slight continuous slope on this level is noise introduced by a slow change in the relative length difference of the two arms of the interferometer, due to temperature drift.

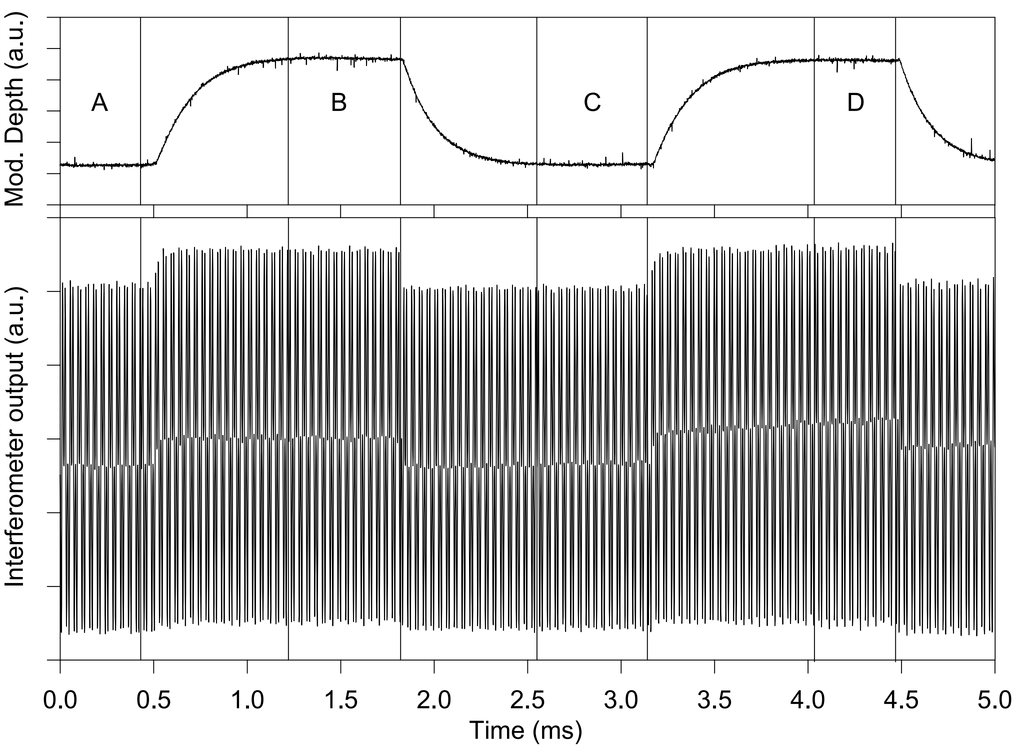

Fig. 4.20 Corresponding reflectivity (top trace) and phase measurements (lower trace) for peak pump power 5mW and temperature 27.0°C; the square wave modulated pump pulses have an 100% modulation depth; the slow edges at the reflectivity measurement are due to the slow response of the detector used

The phase ϕ_S was then acquired by fitting eq. 4.1 to short portions of this signal, for which the nonlinearity has relaxed (e.g. sections A, B, C and D in fig. 4.20). In the fitting process the drift contribution ϕ_N was approximated by a linearly varying signal with time. Examples of the fitted data for the sections B and C of fig. 4.20 are shown in fig. 4.21. Then, ϕ_S was calculated as $\phi_S = \frac{\phi_B + \phi_D}{2} - \frac{\phi_A + \phi_C}{2}$, where ϕ_A, ϕ_B, ϕ_C and ϕ_D are the figures of phase bias calculated for each of the sections A, B, C and D. Note that mean values of the calculated phases were used in order to reduce the uncertainty of the measurement.

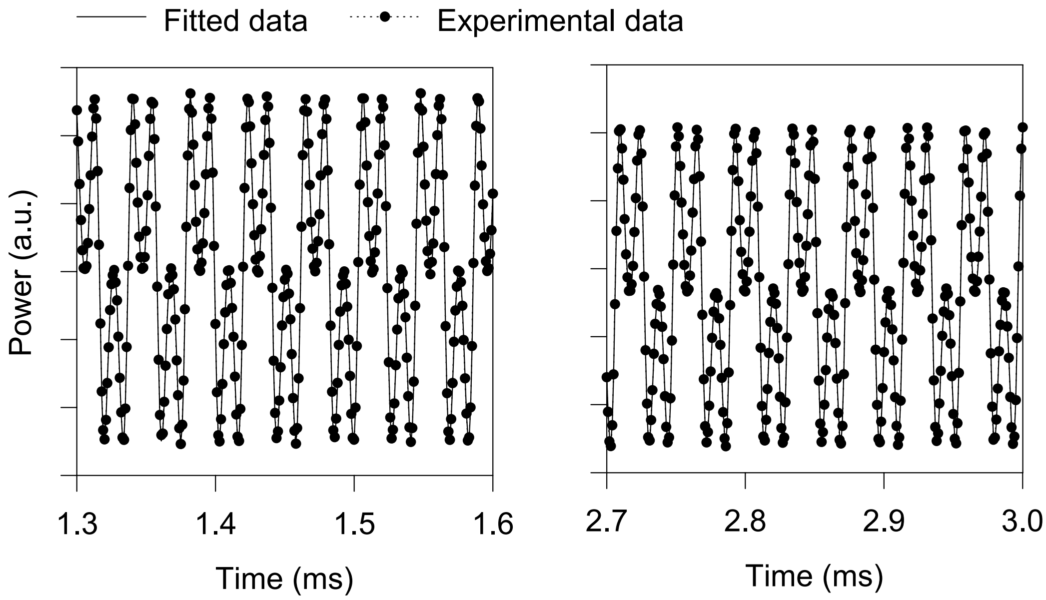

(a) *(b)*

Fig. 4.21 Comparison of the fitted and experimental data for the regions B (a) and C (b) of fig. 4.20

The dependence of nonlinear phase response on temperature, obtained for a pump peak power of 5mW is shown in fig. 4.22. As the nonlinearity builds up with increasing temperature, the phase response remains quite small, always less than 0.14 rads (8^o). Clearly, the phase changes observed are quite small compared with the sensitivity limit of the set-up, and no clear conclusions can be drawn. Thus, a more sensitive heterodyne detection system was necessary, as described in the following section.

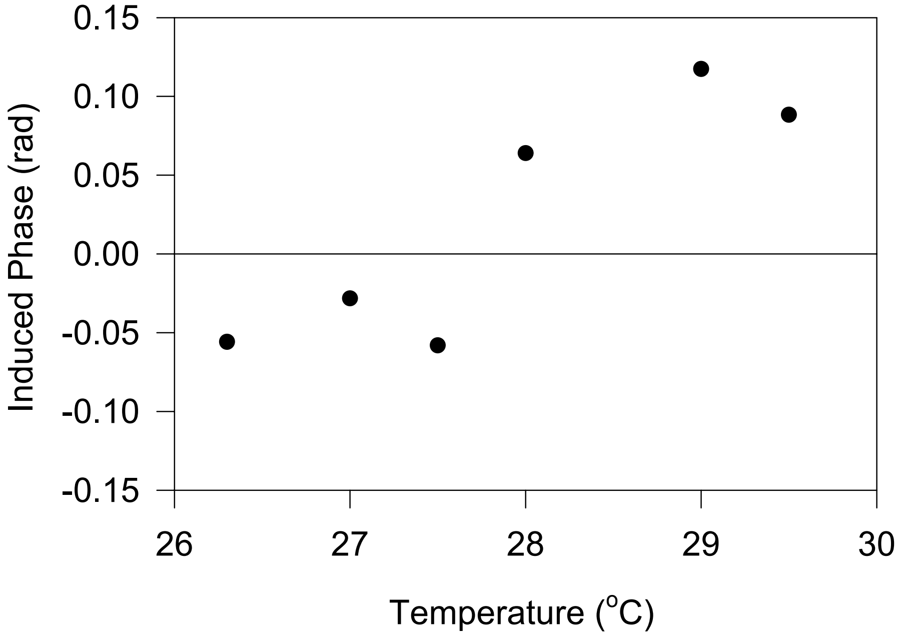

Fig. 4.22 Nonlinear phase response vs. temperature for peak pump power 5mW, as measured with the homodyne processing technique

4.8.2 Heterodyne detection

The difference between the homodyne and heterodyne techniques lies in the fact that for the latter the optical frequencies in the two arms of the interferometer are unequal. This can readily be achieved by introducing a frequency shifter in the reference arm. Apart from this difference, the main principles governing the two techniques remain of course, the same. However, the phase modulation imposed on the reference arm is now $\Delta\phi(t) = \omega_m t$, and consequently the detected signal at the output of the interferometer is

$$P_o = P \cdot (1 + V \cdot \cos(\omega_m \cdot t + \phi_S(t) + \phi_N(t)) \qquad \text{Eq. 4.2}$$

A standard phase demodulator can then be used to obtain the phase response ϕ_S of the detected signal. Such a demodulator compares the detected signal to the carrier and produces a third signal, the profile of which is a function of the time delay between the two. This signal contains the baseband information, which is then extracted by low-pass filtering. Calibration of the demodulator output to real phase changes was performed as before, by temporarily substituting the circulator and gallium mirror by a PZT, applying a known phase change on it, and relating the reading obtained from the demodulator to this change. The sensitivity limit was defined by the minimum detectable phase change, which was measured to be as little as 3.5mrad (0.2^o), a major improvement from the previous, homodyne detection system.

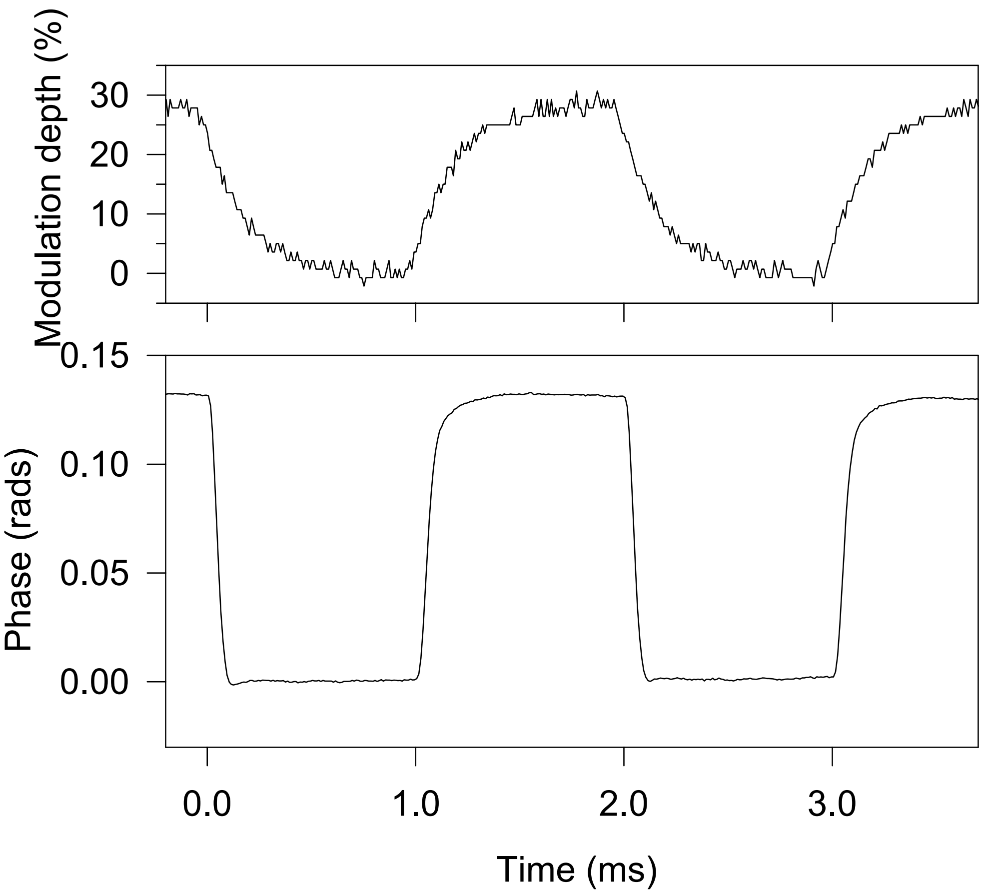

Fig. 4.23 Corresponding reflectivity (top trace) and phase measurements (lower trace) for peak pump power 5mW and temperature 26.8^{o}C; the square wave modulated pump pulses have an 100% modulation depth; the slow edges at the reflectivity measurement are due to the slow response of the detector used

The experimental procedure was the same as before: The changes in the phase and magnitude of the reflectivity of the weak probe beam were monitored at various temperatures close to gallium's melting point under optical stimulation of the pump (fig. 4.16b). As before, the pump signal consisted of 500Hz square pulses, and had a peak power which could be varied from 0 to ~ 5mW. The carrier frequency ω_m was 27.1MHz, the resonance frequency of the acousto-optic modulator used. Data acquisition from the received signal was more direct (compared to the homodyne system) after the use of the demodulator. Fig. 4.23 shows some oscilloscope traces obtained at a mirror temperature of 26.8^{o}C and for 5mW peak pump power.

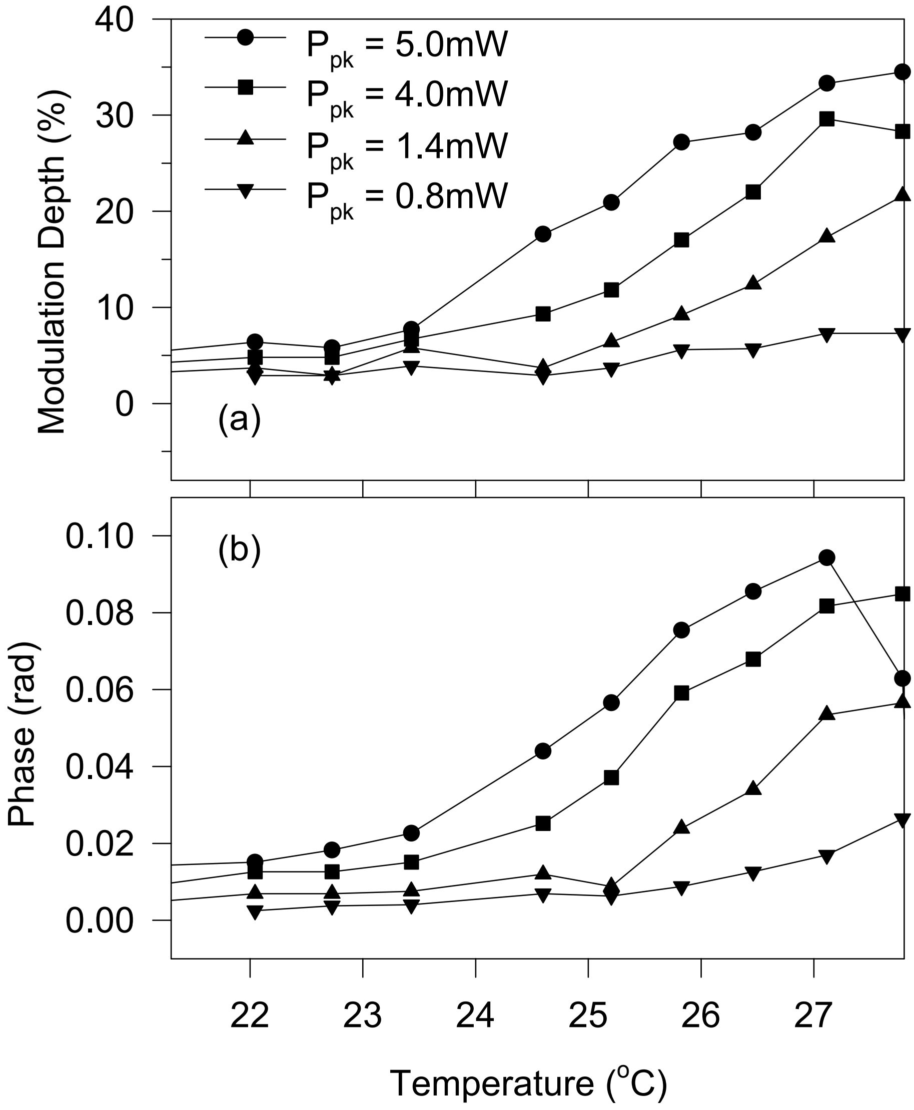

Fig. 4.24 Dependence of the modulation depth (a) and phase shift (b) on temperature for different levels of pump power

These measurements have allowed a closer investigation of the dependence of optical phase on pump power and temperature. Fig. 4.24 shows simultaneous measurements of the modulation depth and the induced phase for various pump powers and temperatures. As the temperature approaches ~ 28°C, the phase response of the nonlinearity increases up to ~ 0.1rad (~ 5.5°). As the temperature increases further, the phenomenon of decreasing reflectivity under optical excitation, which had been described before in fig. 4.7 takes effect. The optical phase change accompanying these reflectivity changes is shown in fig. 4.25. Sharp changes in the induced phase are observed at the instances of rapid pump power changes. Then, as pump power remains to a constant high value, the induced phase relaxes slowly (dominated apparently by a second, counter-acting nonlinear component). However, once the gallium bead melts, the reflectivity increases to ~ 87%, and no other nonlinearities arise in the reflected power or optical phase of the signal, for as long as the mirror remains molten.

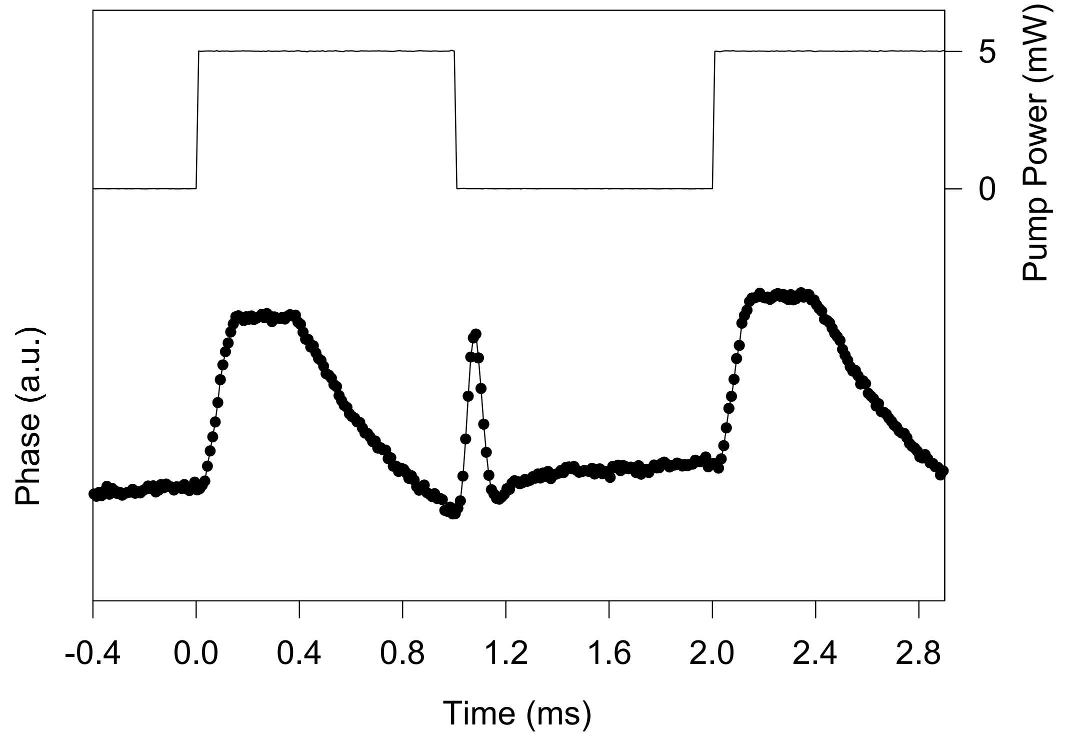

Fig. 4.25 Nonlinear phase shift at a mirror temperature of 28.2^{o}C (bottom trace) induced by a square wave modulated pump of 5mW pump power

Once both magnitude and phase of the reflectivity have been determined, the dependence of the nonlinear reflectivity on temperature and pump power as a complex entity has been characterised. If $\overline{E}_{nl} = E_{nl}e^{-j\phi_{nl}}$ and $\overline{E}_l = E_l e^{-j\phi_l}$ are the reflected electric fields with and without optical excitation respectively for a given temperature, then $\overline{E}_{nl}$ can be expressed in terms of $\overline{E}_l$ as follows:

$$\frac{\overline{E}_{nl}}{\overline{E}_l} = \frac{E_{nl}}{E_l} e^{-j(\phi_{nl}-\phi_l)} = \sqrt{1+\frac{\Delta R}{R_l}} \cdot e^{-j\Delta\phi}$$

where Δϕ is the phase shift that we have measured, ΔR the difference in reflectivity of the excited and non-excited states, and R_l the reflectivity of solid gallium under conditions of no optical excitation. Then $\Delta R/R_l$ is what we have defined as modulation depth (see section 4.5.1). Thus, the results presented in fig. 4.24 can be expressed as changes in the complex electric field, as shown in fig. 4.26 for a peak pump power of 5mW.

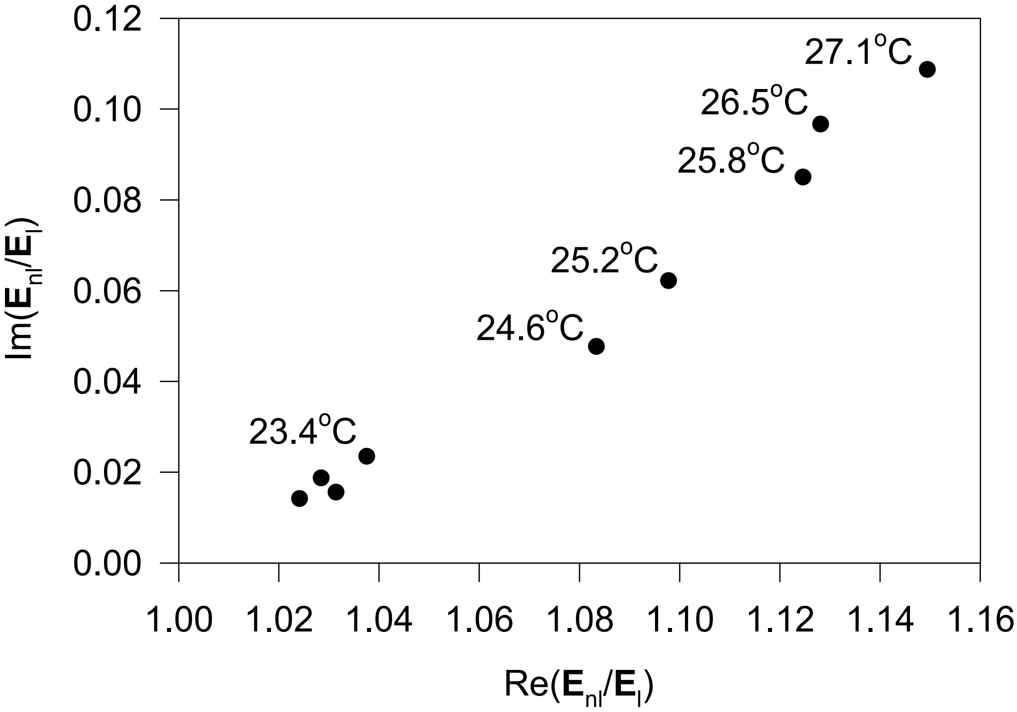

Fig. 4.26 Representation on the complex plane of the ratio of the nonlinear to the linear reflected electric field for pump power 5mW and various temperatures

4.9 Reproducibility

During the experiments described in the previous sections the gallium samples were changed every one or two days, as it was observed that their performance tended to degrade with time. To assess the reproducibility/degradation of the effect, gallium mirrors were taken through several continuous meltings and solidifications in the range 18 to 32°C, under square wave pump excitation of 5mW peak power, while their reflectivity level and induced modulation depth were monitored. Fig. 4.27 shows the modulation depth profile versus temperature for a series of 28 cycles, carried out over a period of three days. Although the mirror's short-term performance was rather stable and reproducible, it showed a long-term degradation in terms of the modulation depth achieved. Thus, the plots in the graph can be divided into three groups, according to the achievable modulation depth. Each one of the groups corresponds to one day, with the modulation depth being bigger for the first day. The most noticeable difference though, is the fast degradation and eventually vanishing of the phase of the

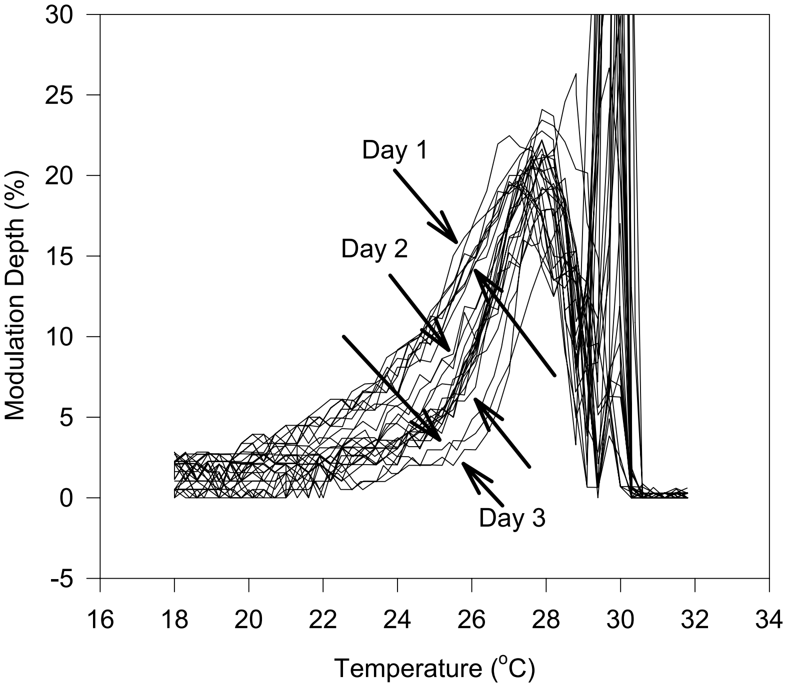

Fig. 4.27 Output probe modulation depth as a function of temperature for 28 consequent meltings of the same sample, carried out over a period of 3 days for square wave pump pulses of 5mW peak power at a modulation frequency of 500Hz, 100% modulation depth and 50% duty cycle

inverse nonlinearity close to the melting point. The vertical axis of fig. 4.27 shows only changes of the magnitude of the modulation depth and does not contain any information on the sign of reflectivity change. The sharp peak just below 30°C represents the region where reflectivity decreases in the presence of pump power. However, in other experiments where the gallium sample was continuously exposed to a square wave pump signal of peak power of 5mW for a whole day, the induced modulation depth would not degrade as significantly if the mirror was kept in a constant temperature. It is currently thought the observed degradation can be attributed (in some part at least) to oxidisation of the sample, or some other form of contamination of the interface.

Novel techniques for manufacturing gallium mirrors are currently being considered, that would provide protection of the gallium bead from contamination, as well as help improve the handling of the material. These techniques, which will be briefly discussed in Chapter Six, mainly have to do with decreasing the volume of the gallium bead, which apart from providing enhanced protection, should result in enhancement of the dynamic effect as well.

4.10 Discussion and conclusions

In the experiments presented in this chapter, we have established that the reflectivity at the interface of bulk gallium with glass can be controlled by light to change by as much as 30%, when operating at temperatures close to, but below gallium's melting point of ~30^{o}C. These experiments were conducted at wavelengths around 1550nm, but the broadband reflectivity characteristics of gallium suggest that these effects should be observable in other parts of the spectrum, both in the visible and the infrared [Albanis99a]. The effect that we observe is reversible, i.e. after removal of the optical stimulation the reflectivity returns back to its original level. This implies the initiation of a true nonlinear process [Klingshirn95].

A range of possible scenarios for the physical mechanisms that might be at the origin of the huge nonlinearity of gallium have been considered. The most obvious candidate is simple bulk melting. However, bulk melting due to light-induced local heating of the sample can be excluded, since gallium exhibits supercooling, and hence any nonlinearity caused by bulk melting would be irreversible. Moreover, assuming τ = 3μs, a representative figure of the nonlinearity transient time for temperatures a few degrees below the melting point in presence of a pump power of P = 5mW (see section 4.6.1), then it can be shown that the heat will spread $L_D \sim (\chi \cdot \tau)^{1/2} \sim 7.5\mu m$ inside the gallium sample, around the excitation point, where $\chi = 1.86 \cdot 10^{-5}$W/m·K is the thermal diffusivity of gallium (polycrystalline data [Duley78]). The energy required to melt gallium in this volume is approximately $L_D^3 \cdot H \sim 200nJ$, where $H = 4.7 \cdot 10^8 J/m^3$ is the latent heat of melting for α-Ga. However, during this period of time, the pump is capable of delivering only a small fraction of the energy required for melting, since $(1 - R) \cdot P \cdot \tau \sim 7nJ$, where R = 0.47 is the reflectivity of α-Ga at 1550nm. Therefore, the nonlinearity has to be governed by some other mechanism.

An alternative is that a continuous phase transition from the α-Ga phase to some other metastable phase of higher reflectivity is responsible for the nonlinearity. A model was developed to describe this possibility, and can be found in [Albanis99b].

Although the development of this model was not immediately relevant to the work described here, its main features are given below for completeness.

According to the model, the metastable phase has a more metallic character, and hence a higher reflectivity than α-Ga, and once the optical stimulation is removed it relaxes back to the stable α-Ga phase. It is shown in [Gong91], that the molecular character of α-Ga leads to a broad absorption band extending from 0.8 - 4eV (i.e. 310 - 1550nm). Absorption of a quantum with energy within this band leads to breaking of the typical covalent bonding of the α-Ga lattice. The crystal then tends to jump into a new phase, one more energetically favourable. Thus, we believe that a layer of this metastable phase is formed at the gallium:glass interface. This phase, because of its free-electron structure, is of a more metallic nature than α-Ga, resulting in a higher reflectivity. We have seen in the experiments a strong dependence of the magnitude of the nonlinear response on pump power. An increase of the excitation power levels reduces the energy difference between the stable α-Ga and the metastable phase. Sample temperature has a similar effect, as the DOS gap at the Fermi energy is weaker at temperatures near the melting point. Consequently, the depth of this layer of metastable phase depends on the pump power and the temperature, and the reflectivity of the interface increases according to the thickness of the layer.

It is believed that the glass interface plays a critical role in supporting this layer, and hence enhancing the development of the continuous phase transition. Gallium is one of the few metals that show surface melting [Gong91], i.e. covering of the crystal surface by a layer of a different phase, if this is thermodynamically preferable. The thickness of this layer can explicitly be determined by thermodynamical considerations [Trittibach94], and is associated with the energy difference between the two phases. Moreover, it increases as the temperature approaches the transition temperature (in our case the melting point), a feature which is in agreement with the nonlinearity growth with temperature that we have seen in our experiments.

Once the optical stimulation terminates, the α-Ga phase becomes once again energetically more favourable. The interface between the metastable phase and α-Ga moves from inside the sample towards the surface, and its kinetics are governed by the classical thermodynamic model [Petteves91], according to which the velocity of an interface is proportional to the difference between the bulk melting temperature and the sample temperature. The relaxation time is then proportional to $1/(T_m\text{-}T)$, a fact which is in good agreement with our experimental observations (see fig. 4.15b).

However, not every aspect involving this nonlinearity is fully understood yet. For example, the effect of decreasing reflectivity, observed just below melting (fig. 4.7 and 4.25) is now being looked at. First indications attribute this to surface roughening, but the creation of a grating structure that scatters the light at a direction perpendicular to the incidence has not been excluded yet.

In order to evaluate the strength of the nonlinearity, an estimate of the frequency degenerate third order nonlinear susceptibility $\chi^{(3)}$ would be required. This can be estimated from the difference in the dielectric coefficients between the normal crystalline form of gallium (α-Ga) ε_α, and the phase of gallium, once nonlinearities have arisen ε_m. The susceptibility $\chi^{(3)}$ is then given (in electrostatic units) as [Albanis99b]

$$\chi^{(3)} = \frac{|\varepsilon_\alpha - \varepsilon_m|}{4\pi E^2} \qquad \text{Eq. 4.3}$$

Measurements of the dielectric coefficient for α-Ga for the different crystalline axes of the metal are given in [Kofman77]. Based on this data, we estimate that the dielectric coefficient of α-Ga is $\varepsilon_\alpha = -1.29\text{-}i21.55$ at 1550nm. This is based on an assumption of equal contributions from the *a* and *c* axes of the Ga crystal [Kofman77], which is consistent with the broadband reflectivity characteristics of α-Ga for polarised light [Albanis99c]. Consequently using $N_\alpha^2 = \varepsilon_\alpha$, where $N_\alpha = n_\alpha\text{-}ik_\alpha$ is the complex refractive index of the material, we find that $n_\alpha = 3.186$ and $k_\alpha = 3.382$. From this the reflectivity R_α and phase change $\Delta\phi_\alpha$ at a gallium glass interface can be calculated respectively from

$$R_\alpha = \frac{(n_\alpha - n_g)^2 + k_\alpha^{\ 2}}{(n_\alpha + n_g)^2 + k_\alpha^{\ 2}}$$
$$\Delta\phi_\alpha = \tan^{-1}\left(-\frac{k_\alpha}{n_\alpha - n_g}\right) - \tan^{-1}\left(-\frac{k_\alpha}{n_\alpha + n_g}\right) \qquad \text{Eq. 4.4}$$

where $n_g = 1.456$ is the refractive index of glass. These calculations give a figure $R_\alpha = 0.44$ for this face of the crystal, which is close to 0.47 that we have characterised from the experiments, and $\Delta\phi_\alpha$ = -0.47rad (-26.83^o). Since the nature of the metastable phase of gallium under optical excitation is unknown, a crude estimation of the dielectric coefficient of this phase ε_m can be made if we assume that the reflectivity of the interface under conditions of maximum nonlinear response is solely due to the metastable phase. This would imply that the net reflectivity and optical phase of this metastable phase of gallium is that observed under such conditions. Fig. 4.24 shows a maximum nonlinear change in reflectivity of 0.333 and in phase of 94mrad (5.4^o). Using these, and the numbers calculated before for α-Ga, one can easily find that $R_{nl} = R_\alpha + 0.333R_\alpha$ or $R_{nl} = 0.59$, and $\Delta\phi_{nl} = \Delta\phi_\alpha + 0.094$ rad or $\Delta\phi_{nl}$ = -0.37rad (-21.43^o). The complex refractive index N_m can then be calculated using a system of equations of the type of eq. 4.4. A root that satisfies this system is $N_m = 3.730\text{-}i5.108$, and consequently $\varepsilon_m = N_m^2 = -12.18\text{-}i38.11$ and $|\varepsilon_\alpha - \varepsilon_m| = 19.82$. Eq. 4.3 yields then a third order nonlinear susceptibility $\chi^{(3)}$ of ~0.06esu (~10^{-9}m^2/V^2 in SI), where an intensity of the order of 1kW/cm^2 was used in the calculations, which was found adequate to give rise to the nonlinearity.This obviously is making certain simplifying assumptions regarding the physical origins of the effect, which might not be strictly valid. However, the nonlinearity is clearly huge, as a comparison to that of silica can show - 10^{-14}esu. (As an additional calibration of the magnitude, if we were to assume that this metastable phase of gallium has the same properties as liquid gallium, which is actually not unreasonable, since several identified metastable phases of gallium possess such properties [Wolny86], then $|\varepsilon_\alpha - \varepsilon_m| = 176$ [Albanis99b]. This yields a third order nonlinear susceptibility $\chi^{(3)}$ of ~0.55esu or ~10^{-8}m^2/V^2 in SI).

We have applied this big nonlinearity to perform passive Q-switching of fibre lasers. These experiments are described in the following chapter.

Chapter Five

Application of the nonlinearity of gallium for Q-switching of fibre lasers

Overview: The potential of nonlinear gallium mirrors for Q-switching of lasers was initially demonstrated in an erbium-fibre ring cavity, which gave ~1μs wide pulses of repetition rate and peak power varying with the mirror temperature. Gallium mirrors were then used to Q-switch higher power fibre lasers, of more appropriate designs to deliver shorter pulses, and pulse energies up to 10μJ. More importantly, Q-switching of ytterbium-fibre lasers (operating in the 1μm region) was also demonstrated, and constitutes the first experimental verification of the existence of the nonlinearity in that part of the spectrum.

5.1. Passively Q-switched lasers in the infrared region

Q-switching of lasers is a well established technique for providing high peak power pulses and is based on rapid modulation of the laser cavity loss from a high to a low value and back again [Siegman86]. Q-switched lasers have found use in numerous applications including amongst others lidar, remote sensing, nonlinear optical processing, material processing, frequency doubling and pumping of nanosecond optical parametric oscillators (OPO's). Many different approaches can be employed to achieve Q-switching. Acousto-optic [Myslinski92] or electro-optic modulators [Morkel92] are more commonly used for active Q-switching (see also e.g. [Mears85], [Chandonnet93] and [Alvarez-Chavez00]), whereas a variety of saturable absorbers provide a passive alternative. In general, active techniques are less preferable since they require more power supplies and bulky optical components, making the laser system less compact and more complex and expensive.

A good passive Q-switch mirror should exhibit a good reflectivity contrast, an adequately high radiation damage threshold, and sufficiently fast turn-on time, i.e. the saturable absorber should saturate before the laser gain coefficient, but at the same time the energy necessary for bleaching the absorber should be delivered to it after the laser threshold is reached [Siegman86]. This last point comes from the requirement that for good Q-switching the initial number of photons in the laser cavity, before any Q-switching action has occurred, must grow at a very fast rate, typically $\frac{d\Phi}{dt} > 10^7 \frac{photons}{s \cdot cm^3}$, and which consequently requires laser action [Pollack95].

Organic dyes [Jones93], colour centres [Beach92] and materials incorporating the Cr^{4+} ion [Zhou93] are well known saturable absorbers for wavelengths extending from the visible up to ~1200nm. However, there is a constant interest to develop efficient Q-switches for the near-infrared region to satisfy the demands for eye-safe lasers (i.e. those based on the Er^{3+} ion at 1550nm) in the medical, industrial and military fields. Only a small number of papers has been published towards this direction, and research for an efficient and practical solution is still active.

In [Stultz94], U^{4+} in a strontium fluoride (SrF_2) matrix was used to produce Q-switched pulses of 3mJ and 60ns width from an Er:glass laser, and in [Terry95] single pulses of energy 1 - 3mJ and duration of ~100ns were produced using multiple quantum well (MQW) structures. In both cases though, damage of the Q-switch due to excessive power density was a major issue. Other approaches [Denker90, Spariosu93] used materials doped with Er^{3+} ions as saturable absorbers, however since the saturation intensities for the absorber and the gain medium were the same, the results reported were not very impressive.

Recently, vanadium dioxide (VO_2) has attracted some interest for Q-switching of a variety of lasers. VO_2 undergoes a phase transition at ~68°C, manifesting itself as a change in the optical constants. Thus, the temperature-dependent reflectivity can provide the reflectivity contrast required. In [Pollack95], VO_2 films were temperature biased around that temperature, and the fast phase transition caused by heat released by laser radiation resulted in Q-switching of an Er:glass laser, giving pulses of a few mJ energy and duration of the order of 10^{-7}s. Moreover, the change of the optical constants across the phase transition of VO_2 is quite significant in both the visible and infrared wavelength ranges [Becker96]. Subsequently, VO_2 was successfully used to Q-switch a Nd:YAG laser, yielding similar results [Bugaev81]. However, problems concerning longevity and damage as well as optimisation of the film thickness, substrate composition, contrast and operational temperature have not been solved.

The most promising and successful solution for passive Q-switching (as well as mode-locking) is semiconductor saturable absorber mirrors (SESAM's). The recent advent of bandgap engineering has allowed growth of materials with good control over their critical paremeters, such as absorption wavelength and saturation energy. SESAM technology enables fabrication of devices with reflectivity, modulation depth and response times that can be accurately controlled to fit any requirements [Keller96]. The majority of research on SESAM's focuses on lasing wavelengths around 1μm. Recently, however, there has been considerable interest in designing saturable absorbers suitable for longer wavelengths as well [see e.g. Fluck97, Paschotta99]. In particular, in [Paschotta99], an erbium-fibre laser was Q-switched using a specially designed SESAM. The laser delivered 65ns pulses, with 4.9μJ pulse energy. A collimated beam was applied to the mirror, which enabled use of multiple bounces on it, to increase the effective modulation depth. With this method (and six bounces on the mirror) 14ns pulses with 17μJ pulse energy were produced.

However, all of the options that were considered above involve the use of complex structures to obtain the necessary saturable absorption characteristics and, with the exception of VO_2, none is particularly broadband. As discussed in Chapter Four, the nonlinearity of gallium near its melting point exhibits saturable absorption characteristics, raising the issue of its suitability for use as a Q-switch.

5.2. Q-switching of an erbium-fibre ring laser

The viability of using liquefying gallium mirrors for Q-switching of fibre lasers was first explored and demonstrated with a fiberised ring laser cavity, constructed from connectorised ready-to-use components. The scope of these experiments, was to characterise the behaviour of the mirror itself as a Q-switching element, and no effort was taken to optimise the laser design. It was later demonstrated (see Section 5.3) that with optimisation considerably shorter pulses and higher peak powers could be obtained.

5.2.1 *Laser configuration*

Fig. 5.1a shows the fibre ring cavity initially used. The active medium was an in-house Nd:YLF pumped power amplifier containing a 5m section of erbium:ytterbium co-doped fibre containing 700ppm Er^{3+} and 20000ppm Yb^{3+}. A polarisation insensitive isolator and use of an optical circulator ensured unidirectional operation and light was outcoupled of the cavity by a 40% coupler. The mirror was formed at the cleaved end of a single-mode fibre in the same fashion that was described in section 4.3 and light was coupled onto and off it by means of an optical circulator. The ring was thus effectively fully fiberised and had a total cavity length of 15m, corresponding to ~73ns cavity round-trip time.

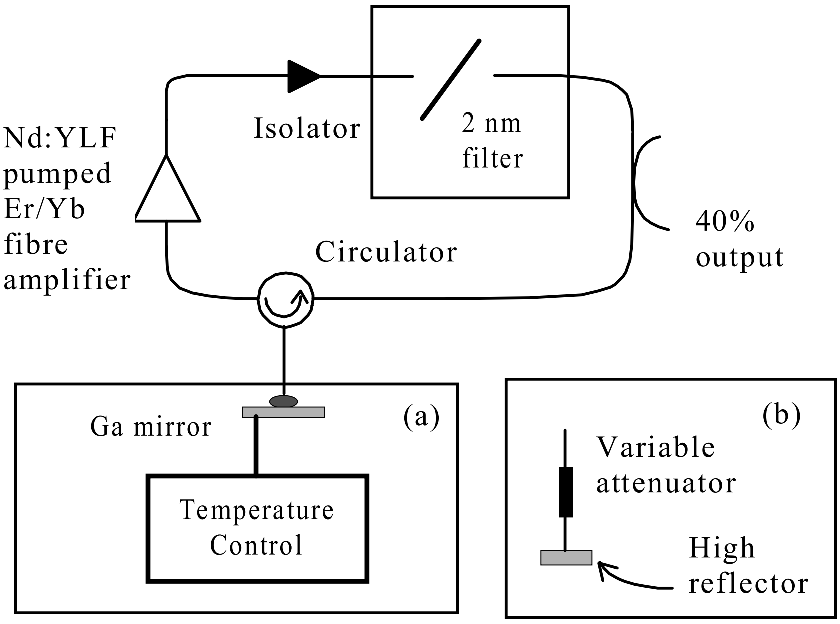

Fig. 5.1 Q-switch ring laser cavity incorporating (a) the liquefying gallium mirror and (b) a variable reflectivity fiberised linear reflector. The 2nm tunable filter was included later to demonstrate tunability of the laser

The performance of the laser configuration shown in fig. 5.1a was characterised for a broad range of pump powers and mirror temperatures, ranging from as low as 0°C up to ~3 - 5°C below the bulk melting point. By adding a 2nm intracavity filter it was verified that lasing was not highly wavelength specific. Tunability of the Q-switched laser over the whole erbium gain band was demonstrated.

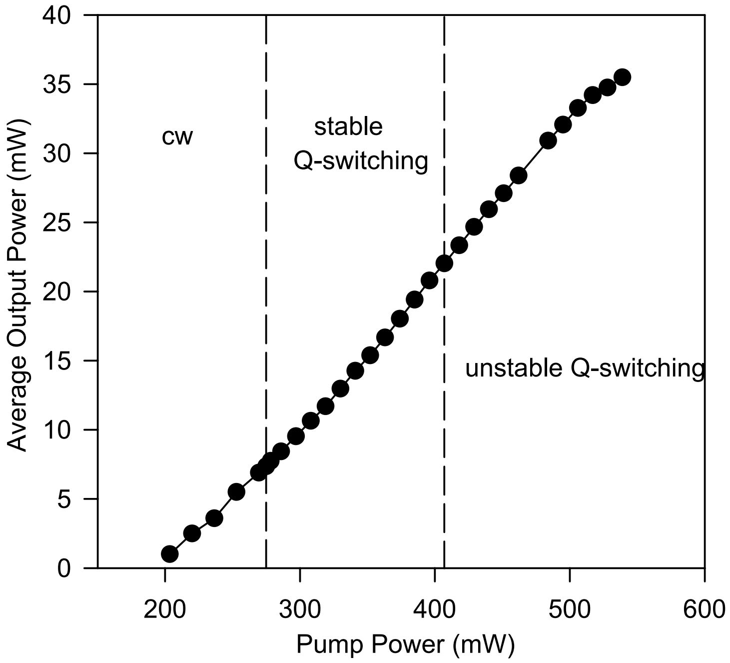

Fig. 5.2 Laser characteristic obtained for a mirror temperature of 17°C. Regions of continuous wave output, stable Q-switching and unstable Q-switching are indicated. The laser threshold is ~200mW and slope efficiency ~16.5%

5.2.2 *Laser characteristic*

A typical laser characteristic obtained for a mirror temperature of 17°C is shown in fig. 5.2. The slope efficiency is 16.5% and the laser threshold is ~200mW. It can be separated into three well defined sections: At low pump powers no pulsing is observed and the laser gives a continuous wave output. As the pump power is increased though stable Q-switching self-starts, which is maintained until some higher pump power is reached. Beyond that power level, which is again well defined for each mirror temperature, pulsing becomes rather unstable, exhibiting either excessive jitter and amplitude noise or frequency doubling; by frequency doubling we mean that between every two pulses a third pulse (usually of smaller amplitude) is generated. The pump power at which stable pulsing self-starts, and instabilities start, are temperature dependent but well defined at a given temperature. For example, at 17oC the self-start threshold is 270mW (output signal power ~7mW), and instability threshold 410mW (output power ~22mW). The power region of stable Q-switching becomes narrower as the mirror temperature approaches the bulk melting point, closing down mainly from the upper limit side. For temperatures above ~27°C stable Q-switching is not possible.

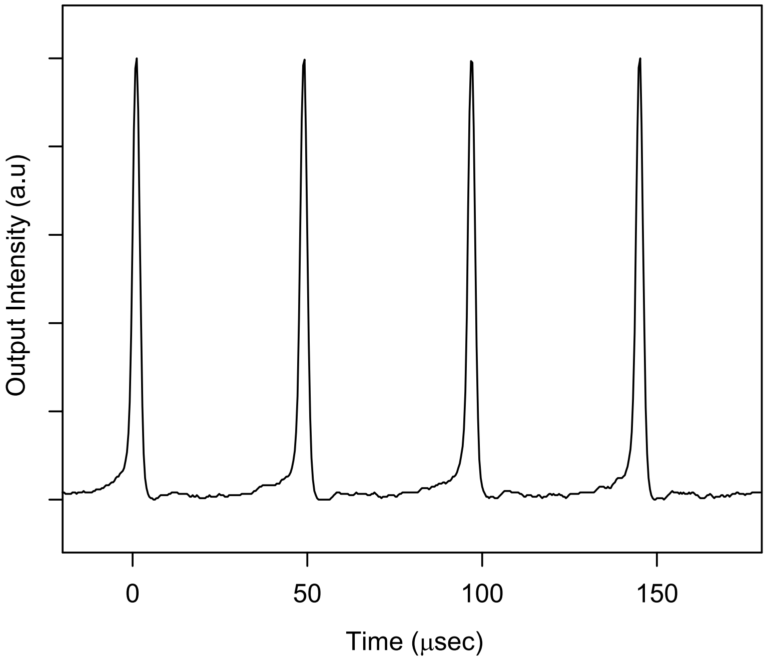

Fig. 5.3 Typical Q-switch pulse train obtained at a mirror temperature of 17°C. The pulse duration is 1.75μs and pulse peak power 100mW

A typical pulse trace for a mirror temperature of 17°C is shown in fig. 5.3. The pump power to the system was 300mW in this instance and the average output power was 13mW, giving pulses of 100mW peak power. The pulse repetition rate was ~20kHz and pulse duration was ~1.75μs. Although the frequency and peak powers varied with temperature, no significant change in the pulse width was noticed and was always between 1 and 1.75μs, depending on the intracavity polarisation settings.

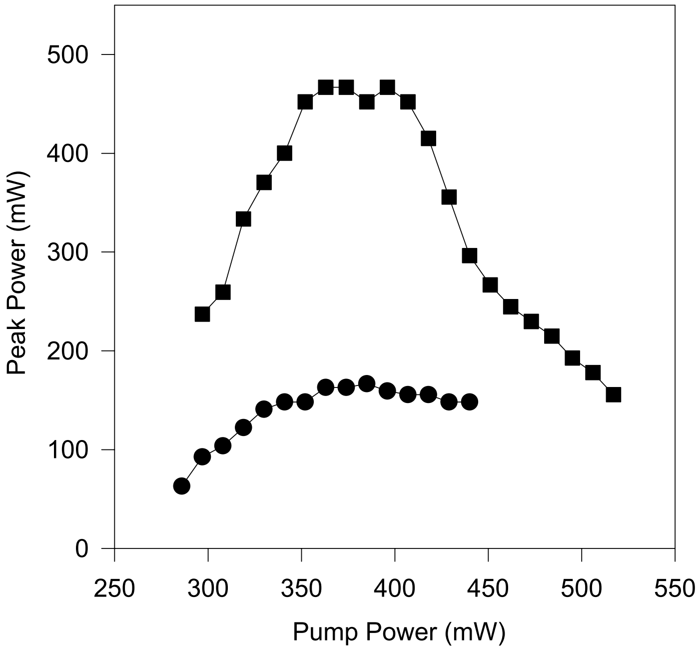

Fig. 5.4 Variation of pulse peak power with pump power for two mirror temperatures: ● 17°C, ■ 5°C

5.2.3 *Dependence of frequency and pulse peak power on pump power*

When operating in the stable Q-switching regime, the peak powers and especially the repetition rates of the pulses depended strongly on the pump power. Fig. 5.4 shows how the pulse peak powers varied with pump power for two mirror temperatures, 5 and 17°C. At 5°C the peak power reached ~450mW for ~400mW pump power, around three times more intense than that at 17°C. This fact is actually expected, due to the smaller reflectivity change for fixed pulse power that the nonlinearity exhibits at lower temperatures. However, as the pump power is increased further, towards the unstable operation regime, the peak powers decreased.

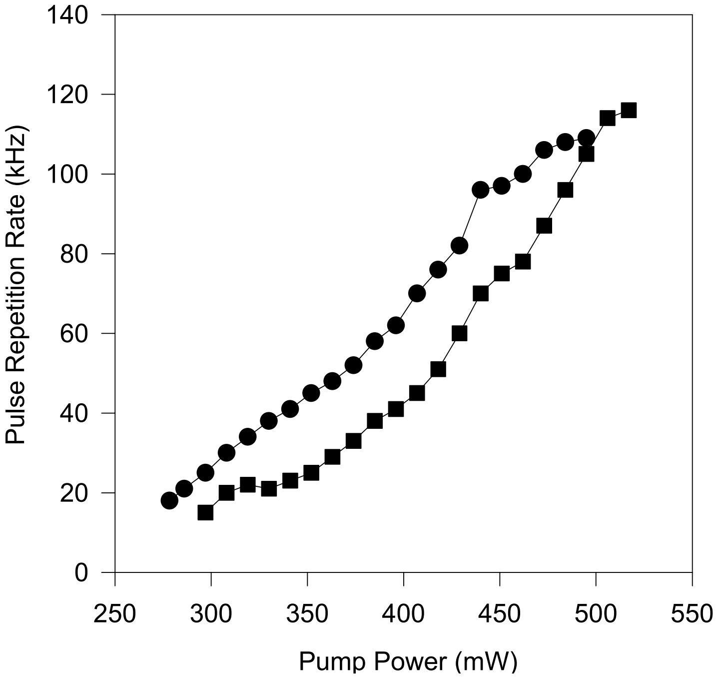

Fig. 5.5 Variation of pulse repetition rate with pump power for two mirror temperatures: ● 17°C, ■ 5°C

The variation of repetition rate with pump power for the same two mirror temperatures of 5 and 17°C is shown in fig. 5.5. The pulse frequency increased in an almost linear fashion with increasing pump power.

5.2.4 *Tunability*

In order to demonstrate tunability of the Q-switched laser over the erbium lasing band, a tuneable 2nm bandpass filter was included in the cavity. The lasing wavelength could be easily tuned from ~1533nm to 1560nm - which was the limit of the filter - covering thus the whole gain spectrum of the erbium:ytterbium amplifier. Q-switched operation was maintained throughout. A typical spectrum obtained at 1543nm is shown in fig. 5.6 showing a 3dB bandwidth of ~0.2nm.

In order to confirm that the observed Q-switching was indeed due to the gallium mirror and not due to some other mechanism, such as self-driven relaxation oscillations of the gain medium, a number of additional experiments were performed, in which the nonlinear mirror was replaced by a conventional reflector with variable linear reflectivity (fig. 5.1b). The reflector was a broadband dielectric mirror with reflectivity >99.9%, and was butt-coupled to the cleaved fibre to form the mirror. The

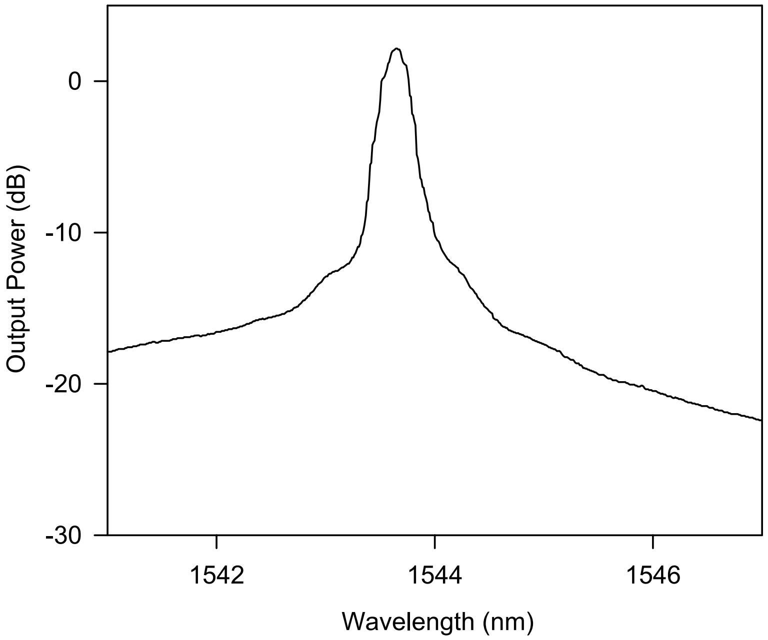

Fig. 5.6 Typical laser emission spectrum for the stable Q-switching regime at 1543nm showing a 3dB bandwidth of ~0.2nm

effective reflectivity of the reflector could be controlled by introducing appropriate bend losses to the fibre. The laser performance was investigated for effective mirror reflectivities spanning from 20% to 99.9%, encompassing the whole range of gallium reflectivities from ~50% (solid) to ~90% (liquid).

5.3. High power Q-switching

The experiments that were described in the previous section demonstrated clearly the suitability of liquefying gallium mirrors for Q-switching of fibre lasers. However, the performance achieved in terms of pulse duration and peak power was not especially impressive. The main limitation of the system performance was imposed by the long cavity length. We thus conducted a number of further experiments to ascertain the performance properties and limits in more optimised cavities, and over broader operating wavelength ranges. We experimented with three more cavities, a large mode area (LMA) erbium- and two ytterbium-fibre lasers. They were of a standard Fabry-Perot design, and used highly doped fibres to reduce the physical cavity length. In these experiments, the liquefying gallium mirror was formed by pressing a thin glass slide on an initially molten gallium bead, which was placed on a Peltier unit. This mirror configuration was used here, rather than the usual fiberised one, to enable experimentation with different spot sizes on the mirror surface. The temperature of the mirror could be controlled in the range 10-35°C, and stabilised within 0.1°C. Note however, that due to the physical layout of the temperature stabilisation unit, any temperature readings that are quoted in the description of the experimental procedure below could differ significantly from the actual temperature at the mirror surface. The characteristics and performance of these lasers are described below.

5.3.1 *LMA Er-doped fibre laser*

The set-up for the LMA Er-fibre laser is shown in fig. 5.7. The Fabry-Perot cavity was formed between the cleaved front end of the fibre, through which the laser was pumped, and the liquefying gallium mirror. The far end of the fibre was angle-polished to prevent any cavity formation from the 4% Fresnel reflection. The spot size on the mirror could be controlled by varying the ratio of the focal lengths of the lens pair L2 and L3. A filter was introduced between the two lenses to block any excess pump light reaching the mirror, and a polariser to allow control of the state of polarisation of the light incident upon the gallium surface. Note that formation of some kind of polarisation controller on the fibre was not possible, due to the high bend loss sensitivity of the LMA fibre. The pump to the system was provided by a 1.6W Ti:sapphire laser operating at 980nm.

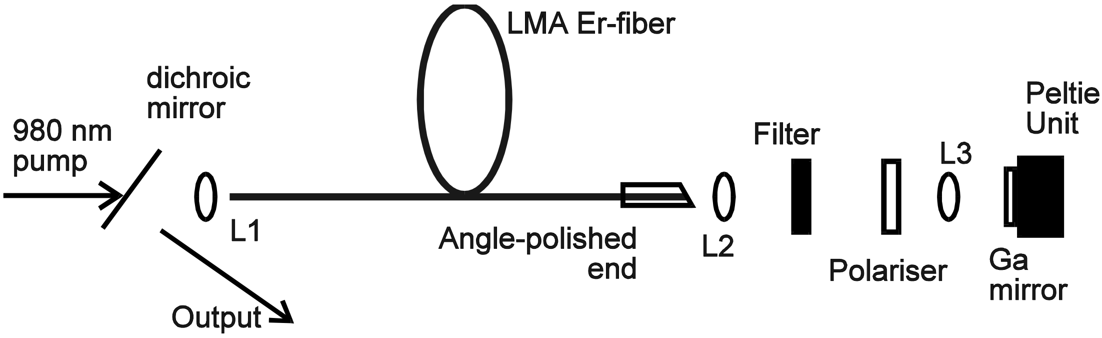

Fig. 5.7 Schematic of the Q-switched laser incorporating LMA Er-doped fibre

The fibre section was 60cm long, and was doped with 1400ppm by weight Er^{3+} ions. The mode field area was ~300μm^2, much larger than the 50μm^2 of a typical Er-doped fibre. It is well known that this method of increasing the core area of the active fibre increases the energy stored in it per unit length [Taverner97, Lees97]. The limitation for this increase is imposed by the requirement that the fibre remains single-moded.

This can be ensured by decreasing its numerical aperture (NA). Thus the NA of the fibre used was 0.06 and its cut-off wavelength 1450nm.

Stable Q-switching of the laser could readily be achieved, once the polarisation on the mirror was adjusted and the level of pump power was suitable. We experimented with a number of spot sizes on the mirror surface, and found that optimum operation, in terms of stability and noise suppression could be performed with a tightly focused beam. Thus, a 30μm^2 spot size was used throughout the characterisation experiments.

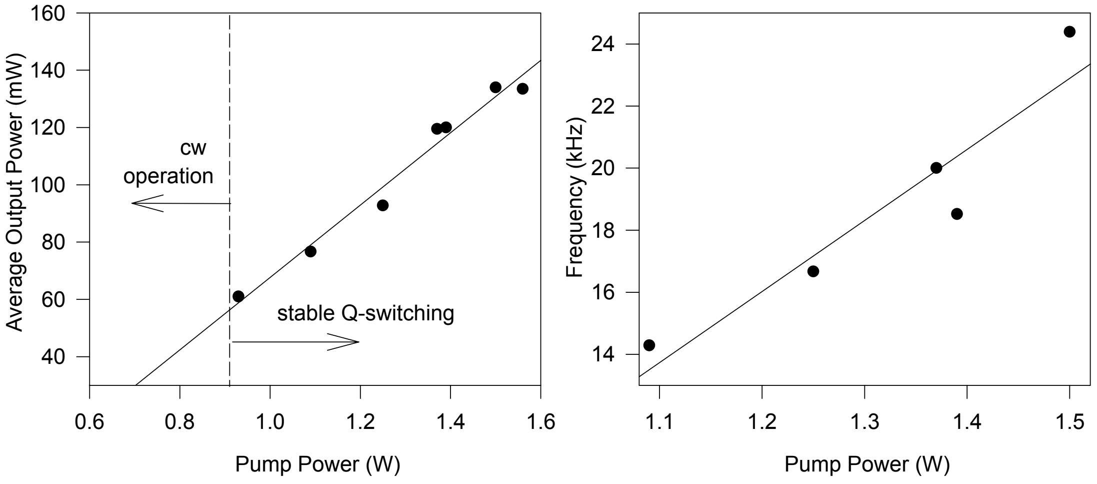

(a) (b)

Fig. 5.8 (a) Typical power characteristic of the LMA Er-fibre laser, showing the regime of stable Q-switching; (b) dependence of the repetition rate on pump power

A typical power characteristic of the laser is shown in fig. 5.8a. Q-switching self-started above a certain incident pump power level, which was ~930mW for a mirror temperature of 14.0°C. Typically, the laser delivered 50-70ns pulses with ~6μJ pulse energy at 1531nm (fig. 5.9). The peak power of the pulses was hence 70-100W. The pulse width and energy were independent of the pump power, whereas the pulse repetition rate increased in an almost linear fashion with increasing pump power (fig. 5.8b). Thus, the repetition rate changed from 14kHz at the self-start threshold up to 25kHz at maximum pump power. Adjustment of the polarisation of the light incident to the mirror was critical for good and stable Q-switching operation. In fact, even a slight departure from the optimal state of polarisation resulted in an increase in the repetition rate and a small increase in the pulse width. More significant detuning of the polarisation rendered self-start Q-switching impossible.

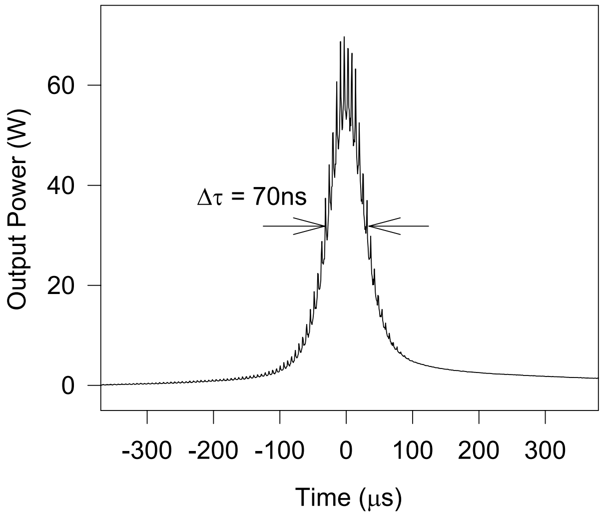

Fig. 5.9 Typical pulse trace, obtained at a mirror temperature of 13.8°C and pump power of 1.09W

The effect of the mirror temperature on the quality of pulsing was investigated as well. The performance of the laser seemed not to be affected significantly by the mirror temperature as long as this was maintained below ~23°C. However, as the temperature increased above 23°C, the repetition rate steadily increased, the timing jitter became more significant (~25°C), and eventually pulsing could no longer be maintained (~26°C). Once the mirror was re-cooled below ~25°C, Q-switching self-started again.

The cavity described here actually used the same components and length of fibre, as that described in [Paschotta99], where a state-of-the-art SESAM designed for Q-switching applications at 1.55μm replaced the gallium mirror. The results reported there (65ns pulses with a pulse energy of 4.9μJ) were almost identical to those obtained with our approach, indicating that the gallium mirror itself was not limiting the performance of the laser.

5.3.2 *Yb-doped fibre laser*

The experiments described in the previous section established gallium as a suitable material for Q-switching, capable of delivering intense pulses, with low amplitude noise and timing jitter. However, the true advantage that gallium mirrors possess is that these inexpensive, simple to make devices have an enormous operational bandwidth. In the experiments described so far we used only ~30nm of this bandwidth around 1550nm, whereas the nonlinearity itself operates from ~400nm to ~1700nm. To demonstrate this we took the same mirror used in the LMA fibre laser described above, and incorporated it in a cavity of the same design as that shown in fig. 5.7, but employing an ytterbium-doped fibre as the active medium, instead of the erbium-doped fibre, thereby shifting the wavelength of operation from 1.55μm to 1μm.

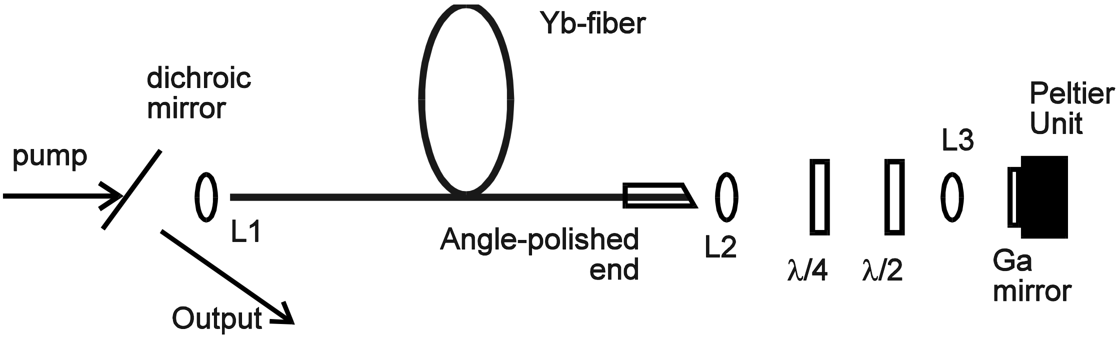

Fig. 5.10 Schematic of the Q-switched laser incorporating the Yb-doped fibre

A schematic of the new arrangement is shown in fig. 5.10. The laser used the same 980nm Ti:sapphire pump source. The Yb-doped fibre was ~90cm long, and of a conventional design with a NA of 0.21 and a cut-off wavelength of 940nm. The fibre was doped with 2300ppm by weight Yb^{3+} ions. The spot size on the mirror surface was maintained at ~30μm^2, by using an appropriate lens combination (L2, L3). Polarisation control of the light incident to the mirror was performed by a quarter- and a half-wave plate that were placed between L2 and L3.

A typical power characteristic for a mirror temperature of 13°C is shown in fig. 5.11a. At low pump power levels the laser operates continuous wave. As the pump power approaches a well-defined level (290mW in this instance), Q-switching self-starts. The width of the pulses was 115-150ns (fig. 5.12), the pulse energy ~1μJ, and the peak power 8-10W. The laser operated at 1030nm. Stable Q-switching would be maintained, as long as pump power did not exceed a second well-defined level (520mW in this case). The individual pulse characteristics did not vary significantly with pump power, but they did vary with the state of polarisation of the light. The repetition rate on the other hand, increased with increasing pump power from 50 to 150kHz (fig. 5.11b).

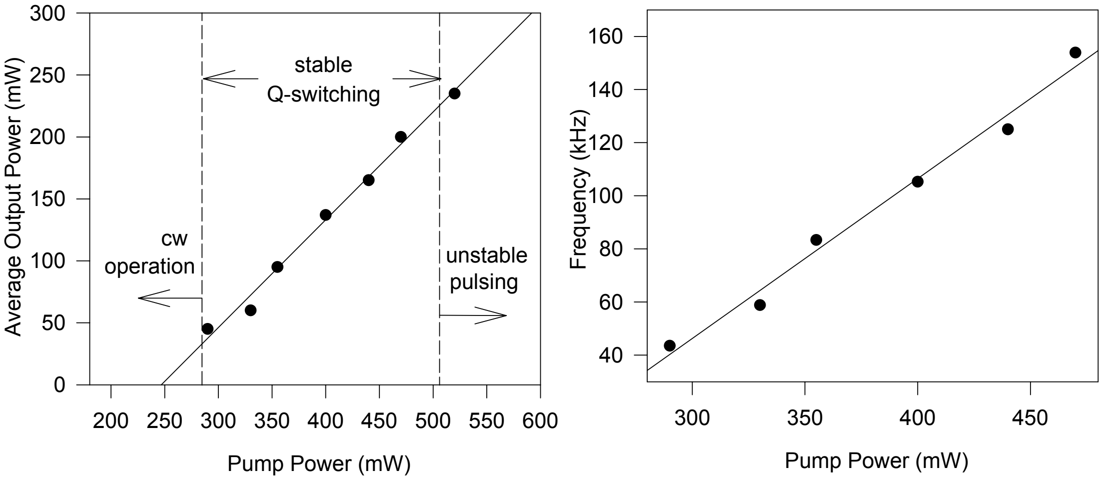

(a) (b)

Fig. 5.11 (a) Typical power characteristic of the Yb-fibre laser, showing the regime of stable Q-switching; (b) dependence of the repetition rate on pump power

Laser operation was not affected by the mirror temperature, as long as this did not exceed ~15°C. At higher temperatures the pulses developed timing jitter, and for temperatures higher than ~21°C pulsing could no longer be maintained.

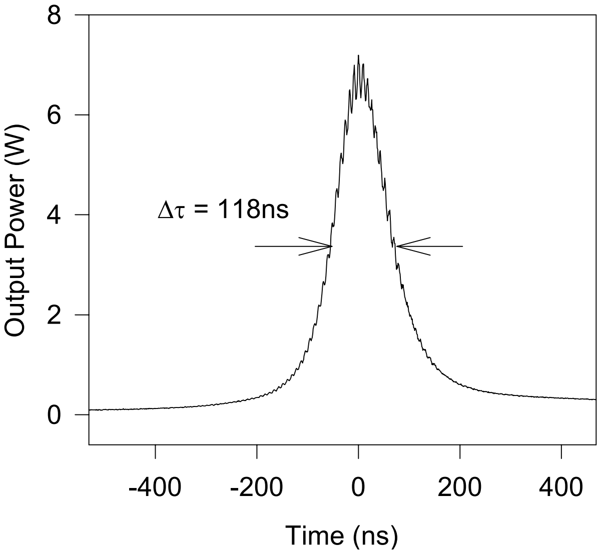

Fig. 5.12 Typical pulse trace, obtained at a mirror temperature of 17.0°C and pump power of 420mW

5.3.3 *Double-clad Yb-doped fibre laser*

Novel fibre designs have hugely contributed to the tremendous progress that the field of high power fibre lasers has experienced in recent years. Double-clad fibres are now commonly used in such lasers to enable the generation of higher output powers. The profile of a double-clad fibre consists of a core, an inner cladding and an outer cladding. The signal propagates in the core, which contains the rare-earth dopant, whereas the pump can propagate in the inner cladding as well. This allows the launch of more pump power into the fibre, whilst maintaining single-moded operation of the laser output. Hence, power scaling of fibre technology is achieved through the use of relatively low brightness, but high power diodes.

The fibre employed in our third laser cavity combined the features of both an LMA and a double-clad fibre. It was a 1.55m section of Yb-doped fibre with a concentration in Yb^{3+} ions of 7000ppm by weight. It had an outer cladding diameter of ~160μm and an inner cladding diameter of ~50μm, whereas the mode field diameter was ~17μm. The NA of the fibre was ~0.1. The laser was otherwise of the same configuration as that described in the previous section (fig. 5.10), and was pumped with a 915nm beam-shaped diode bar [Clarkson96], capable of producing up to 35W in a nearly circular beam of 200μm diameter.

As previously, a tight laser spot size on the gallium mirror proved optimum for stable Q-switching. Although pulsing was highly sensitive to the pump power level, the general behaviour of the laser was the same as that described earlier. Q-switching self-started at a pump power level of 15.5W, and could be maintained as long as pump power did not exceed 21W (fig. 5.13a). The repetition rate depended strongly on pump power varying from as little as 1.5kHz (at the low limit) to ~23kHz (at the high limit) - see fig. 5.13b. The pulses had an energy of ~10μJ (corresponding to a peak power of ~60W) and their width varied slightly with polarisation between 160 and 250ns (fig. 5.14). Q-switching could not be maintained for mirror temperatures above ~21°C.

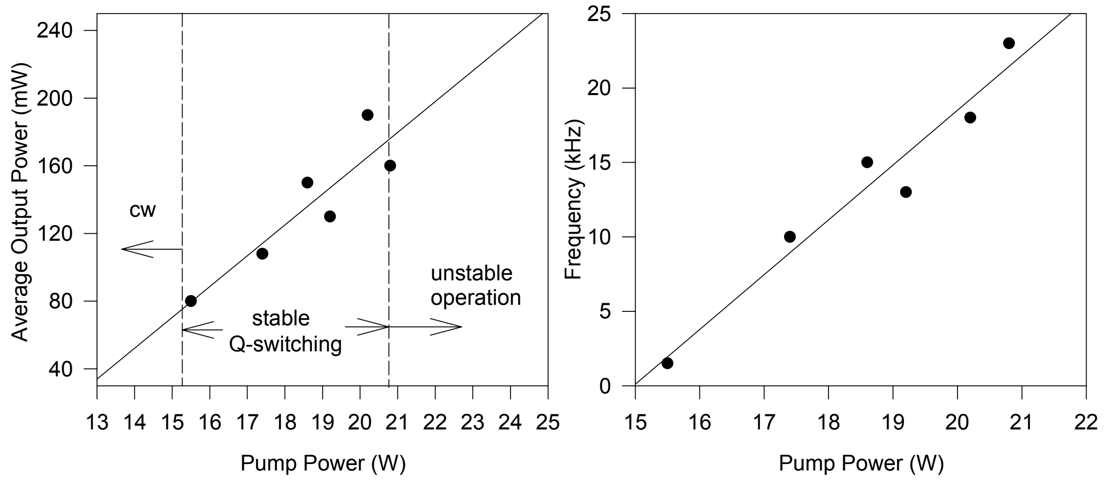

(a) (b)

Fig. 5.13 (a) Typical power characteristic of the double-clad Yb-fibre laser, showing the regime of stable Q-switching; (b) dependence of the repetition rate on pump power

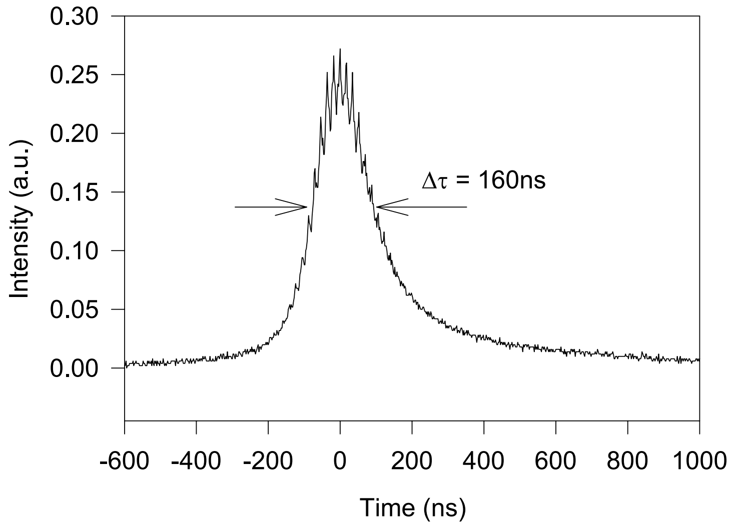

Fig. 5.14 Typical pulse trace, obtained at a mirror temperature of 17.5^{o}C, and pump power of 19W

5.4. Conclusions

In this chapter Q-switching with liquefying gallium mirrors of four fibre lasers was described. The operating wavelengths of these lasers were either around 1 or 1.5μm, demonstrating thus, the compatibility of gallium mirrors with a wide range of lasing regimes. Nanosecond long pulses with pulse energies of a few μJ and kHz repetition rates were achieved. Each of the lasers had their own individual characteristics, but we were able to draw some general conclusions on the behaviour of the gallium mirrors as elements for passive Q-switching.

Stable pulsing can be achieved even for low levels of intracavity laser intensities, in agreement with the measurements presented in chapter Four. In most cases there was an upper limit in the pump levels for which pulsing could be achieved. This is most probably due to the nonlinearity response times not recovering rapidly enough under strong optical excitation, to give rise to stable pulse trains at high repetition rates. However, thermal issues due to signal and pump absorption may also play a role. Q-switching could be obtained even at nominal mirror temperatures much lower than the bulk melting point. However, stable pulsing could not be maintained at temperatures some 5°C below the melting point, most likely due to local heating at the focal spot.

The most stable Q-switching and the shortest pulses were achieved after careful alignment of the signal polarisation. The pulse widths achieved with the different lasers spanned from ~1.5μs to ~50ns, reducing for shorter cavities. Nonetheless, a comparison with Q-switching obtained by SESAM's showed that even in the case of the shortest achievable pulses the width was not limited by the mirror's nonlinear behaviour. It is also worth mentioning that recent measurements have shown that the response times of the nonlinearity can be as fast as a few picoseconds [Luther-Davies00], indicate that possibly, under certain circumstances, the mirrors could be used for mode-locking of lasers, although this was not achieved in our experiments.

The repetition rate of the pulses in the stable Q-switch mode depends strongly on both pump power and temperature. Both these factors are associated with the strength of the nonlinearity, and the fact that the nonlinearity is energy rather that intensity dependent. As the nonlinearity increases (or decreases) smaller (or bigger) energy pulses are required to switch the mirror.

The table below attempts a comparison between different Q-switching materials that have been reported for the near-infrared. Clearly, SESAM's and gallium mirrors are the only Q-switching materials that have been proven suitable for fibre lasers operating at this spectral region. It should be noted that all the pulse width and pulse energy figures quoted correspond to Er-glass (or Er-fibre) lasers.

Table 5.1 Q-switching materials for the near-infrared

	Laser Type	**Operating Bandwidth**	**Pulse Width**	**Pulse Energy**	**Damage Problems**
U^{4+} [Stultz94]	Bulk	1533nm ±10nm	20 - 590ns	10 – 20mJ @1533nm	Yes
MQW [Terry95]	Bulk	* 1550nm ±50nm	~100ns	1 – 3mJ @1533nm	Yes
Er^{3+} [Spariosu93]	Bulk	1550nm ±20nm	83ns	6mJ @1526nm	Yes
VO_2	Bulk	1060nm [Bugaev81] – 1540nm [Pollack95]	>14ns	1mJ @1540nm	Yes
SESAM [Paschotta99]	Fibre	* 1550nm ±50nm	65ns **	4.9μJ @1530nm **	No
Ga	**Fibre**	**1030 – 1560nm**	**50-70ns**	**6μJ @1533nm**	**No**

* Engineerable absorption wavelength

** Based on single-bounce measurements

Chapter Six

Future directions

Overview: The directions that research on gallium as a nonlinear material is currently following are briefly discussed.

Following the investigation of the fundamental nonlinear properties of the metal, which were described in this part of the thesis, further research on gallium focuses firstly on applying more sophisticated mirror fabrication techniques that will guarantee the preparation of more reliable samples, and secondly on further investigating the limits of the speed of the response. Early in our work, it became evident that although the high purity of gallium samples was guaranteed by the supplier, the simple method that was used to manufacture and handle the mirrors compromised their quality and made them extremely vulnerable to external conditions. In an attempt to improve this, gallium mirrors formed on a glass interface have been successfully prepared using the Pulsed Laser Deposition (PLD) technique, according to which a strong pulsed laser beam is aimed at a gallium film placed opposite the glass slide where the mirror is to be formed. The energy from the laser beam causes a uniform evaporation of gallium into free space, part of which condenses onto the glass slide. Such mirrors have been tested showing consistency in their nonlinear characteristics and exceptionally good performance - similar to that described in Chapter Four. Research in this field is ongoing, and a major objective is to prepare fiberised mirrors using the PLD technique, by depositing gallium on the tips of cleaved fibres. Control of the temperature of these mirrors would then be achieved by heating the fibre close to its end.

As well as improving the practical handling aspect of such mirrors, it is thought that further miniaturisation should give rise to an explosive metallisation at the interface. This effect is characterised by response speeds that may reach some three orders of magnitude higher than the ones reported herein. Quite clearly, even though the magnitude of the nonlinearity observed during the course of this work was enormous, implementation of a practical device useful as an optical switch for communication networks, requires much higher response speeds. Indeed, very recently, by using suitable short pulse sources and the aforementioned PLD samples, response times as short as 2ps were discovered [Luther-Davies00]. The pulse energy required to excite the nonlinearity, as well as the magnitude of the response that was observed corresponded directly to the numbers observed in our experiments (see section 4.7.2).

Furthermore, significant research is going on at the Department of Physics that attempts to model the exact behaviour of the nonlinearity, and thus establish a robust model that will fully describe it. Finally, spectroscopic measurements of gallium, concerning its nonlinear behaviour will soon be carried out.

References (Part Two)

[Albanis99a] V. Albanis, S. Dhanjal, N.I. Zheludev, P. Petropoulos, D.J. Richardson, "Cross-wavelength all-optical switching using nonlinearity of liquefying gallium", Optics Express, Vol. 5, pp. 157-62, 1999.

[Albanis99b] V. Albanis, S. Dhanjal, K.F. MacDonald, V.I. Emelyanov, P. Petropoulos, D.J. Richardson, N.I. Zheludev, "Light-induced structural phase transition and optical nonlinearity at a gallium/silica interface", unpublished, 1999.

[Albanis99c] V. Albanis, N.I. Zheludev, private communication, 1999.

[Alvarez-Chavez00] J.A. Alvarez-Chavez, H.L. Offerhaus, J. Nilsson, P.W. Turner, W.A. Clarkson, D.J. Richardson, "High energy, high power ytterbium-doped Q-switched fiber laser", Optics Letters, Vol. 25, pp. 37-9, 2000.

[Beach92] R. Beach, J. Davin, S. Mitchell, W. Benett, B. Freitas, R. Solarz, P. Avizonis, "Passively Q-switched transverse-diode-pumped Nd^{3+}:YLF laser oscillator", Optics Letters, Vol. 17, pp. 124-6, 1992.

[Becker96] M.F. Becker, A. B. Buckman, R.M. Walser, T. Lépine, P. Georges, A. Brun, "Femtosecond laser excitation dynamics of the semiconductor-metal phase transition in VO_2", Journal of Applied Physics, Vol. 79, pp. 2404-8, 1996.

[Bennett98a] P.J. Bennett, PhD Thesis, "Novel polarization phenomena and their spectroscopic application in bulk solids and films", University of Southampton, 1998.

[Bennett98b] P.J. Bennett, A. Malinowski, B.D. Rainford, I.R. Shatwell, Yu.P. Svirko, N.I. Zheludev, "Femtosecond pulse duration measurements utilizing an ultrafast nonlinearity of nickel", Optics Communications, Vol. 147, pp. 148-52, 1998.

[Bennett98c] P.J. Bennett, S. Dhanjal, Yu.P. Svirko, N.I. Zheludev, "Cubic optical nonlinearities of metals in the visinity of the melting point", Journal of Modern Physics, Vol. 45, pp. 1009-18, 1998.

[Boyd92] R.W. Boyd, “Nonlinear Optics”, Academic Press, 1992.

[Bugaev81] A.A. Bugaev, B.P. Zakharchenya, F.A. Chudnovskii, “Q switching of a resonator by the metal-semiconductor phase transition”, Soviet Journal of Quantum Electronics, Vol. 11, pp. 1638-9, 1981.

[Chandonnet93] A. Chandonnet, G. Larose, “High power Q-switched erbium laser using an all-fiber intensity modulator”, Optical Engineering, Vol. 32, pp. 2031-5, 1993.

[Clarkson96] W.A. Clarkson, D.C. Hanna, “Two-mirror beam-shaping for high-power diode bars”, Optics Letters, Vol. 21, pp. 375-7, 1996.

[Denker90] B.I. Denker, G.V. Maksikova, V.V. Osiko, S.E. Sverchkov, Yu.E. Sverchkov, “New methods for passive Q switching of erbium glass lasers”, Soviet Journal of Quantum Electronics, Vol. 20, pp. 877-8, 1990.

[Dhanjal97a] S. Dhanjal, S.V. Popov, I.R. Shatwell, Yu.P. Svirko, N.I. Zheludev, V.E. Gusev, “Femtosecond optical nonlinearity of metallic indium across the solid-liquid transition”, Optics Letters, Vol. 22, pp. 1879-81, 1997.

[Dhanjal97b] S. Dhanjal, I.R. Shatwell, Yu.P. Svirko, N.I. Zheludev, “Giant nonlinearity and reflectivity hysteresis in metallic gallium at melting”, 1997 OSA Technical Digest Series, Vol.12, Conference Edition, p.223-4.

[Duley78] W.Duley, “Laser processing and analysis of materials”, Plenum Press N.Y. and London, 1978.

[Fluck97] R. Fluck, B. Braun, U. Keller, E. Gini, H. Melchior, “Passively Q-switched microstrip lasers at 1.3μm and 1.5μm”, Proceedings on Conference on Lasers and Electro-Optics’97, paper CThK3, 1997.

[Gong91] X.G. Gong, G.L. Chiarotti, M. Parrinello, E. Tosatti, “α-gallium: A metallic molecular crystal”, Physical Review B, Vol.43, pp. 14277-80, 1991.

[Hafner90] J. Hafner, W. Jank, “Structural and electronic properties of the liquid polyvalent elements. III. The trivalent elements”, Physical Review B, Vol. 42, pp. 11530-9, 1990.

[Hecht98] E. Hecht, "Optics", 3rd Edition, Addison-Wesley, 1998.

[Jackson89] D.A. Jackson, J.D.C. Jones, "Interferometers", in "Optical fiber sensors, Vol. II: Systems and applications", by B. Culshaw and J.P. Dakin (eds.), Artech House, Inc., 1989.

[Jones93] D.C. Jones, D.A. Rockwell, "Single-frequency, 500-ns laser pulses generated by a passively Q-switched Nd laser", Applied Optics, Vol. 32, pp. 1547-50, 1993.

[Keller96] U. Keller, K.J. Weingarten, F.X. Kartner, D. Kopf, B. Braun, I.D. Jung, R. Fluck, C. Honninger, N. Matuschek, J. Aus der Au, "Semiconductor Saturable Absorber Mirrors (SESAM's) for femtosecond to nanosecond pulse generation in solid-state lasers", Journal of Selected Topics in Quantum Electronics, Vol. 2, pp. 435-51, 1996.

[Klingshirn95]C.F. Klingshirn, "Semiconductor Optics", Springer, 1995.

[Kofman77] R. Kofman, P. Cheyssac, J. Richard, "Optical properties of Ga monocrystal in the 0.3-0.5-eV range", Physical Review B, Vol. 16, pp. 5216-24, 1977.

[Kofman79] R. Kofman, P. Cheyssac, R. Garrigos, "Optical investigation of the solid-liquid transition in gallium", Journal of Physics F: Metal Physics, Vol. 9, pp. 2345-51, 1979.

[Lees97] G.P. Lees, D. Taverner, D.J. Richardson, L. Dong, T.P. Newson, "Q-switched erbium doped fibre laser utilising a novel large mode area fibre", Electronics Letters, Vol. 33, pp. 393-4, 1997.

[Luther-Davies00] B. Luther-Davies, A.V. Rode, M. Scimoe, N.I. Zheludev, and K. Mac Donald, in Conference on Lasers and Electro-Optics, OSA Technical Digest (Optical Society of America, Washington DC, 2000), *to be presented.*

[Mears85] R.J. Mears, L. Reekie, S.B. Poole, D.N. Payne, "Low threshold tunable cw and Q-switched fibre laser operating at 1.55 μm", Electronics Letters, Vol. 22, pp. 159-60, 1985.

[Morkel92] P.R. Morkel, K.P. Jdrzejewski, E.R. Taylor, D.N. Payne, "Short-pulse, high-power Q-switched fiber laser", IEEE Photonics Technology Letters, Vol. 4, pp. 545-7, 1992.

[Myslinski92] P. Myslinski, J. Chrostowski, J.A. Koningstein, J.R. Simpson, "High power Q-switched erbium doped fibre laser", IEEE Journal of Quantum Electronics, Vol. 28, pp. 371-7, 1992.

[Paschotta99] R. Paschotta, R. Häring, E. Gini, H. Melchior, U. Keller, H.L. Offerhaus, D.J. Richardson, "Passively Q-switched 0.1mJ fiber laser system at 1.53μm", Optics Letters, Vol. 24, pp. 388-90, 1999.

[Petteves91] S.D. Petteves, R. Abbaschian, Metallurgical Transactions A, Vol. 22A, p. 1259, 1991.

[Pollack95] S.A. Pollack, D.B. Chang, F.A. Chudnovsky, I.A. Khakhaev, "Passive Q switching and mode-locking of Er:glass lasers using VO_2 mirrors", Journal of Applied Physics, Vol. 78, pp. 3592-9, 1995.

[Schnering91] H.G. von Schnering, R. Nesper, "α-gallium: An alternative to the boron structure", Acta Chemica Scandinavica, Vol. 45, pp. 870-2, 1991.

[Siegman86] A.E. Siegman, "Lasers", University Science Books, California, 1986.

[Spariosu93] K. Spariosu, R.D. Stultz, M. Birnbaum, T.H. Allik, J.A. Hutchinson, "Er:$Ca_5(PO_4)_3F$ saturable-absorber Q switch for the Er:glass laser at 1.53μm", Applied Physics Letters, Vol. 62, pp. 2763-5, 1993.

[Stultz94] R.D. Stultz, M.B. Camargo, S.T. Montgomery, M. Birnbaum, K. Spariosu, "U^{4+}:SrF_2 efficient saturable absorber Q switch for the 1.54 μm erbium:glass laser", Applied Physics Letters, Vol. 64, pp. 948-50, 1994.

[Taverner97] D. Taverner, D.J. Richardson, L. Dong, J.E. Caplen, K. Williams, R.V. Penty, "158μJ pulses from a single transverse mode, large mode-area EDFA", Optics Letters, Vol. 22, pp. 378-80, 1997.

[Terry95] J.A.C. Terry, M.J.P. Payne, "Passive Q-switching of infrared lasers with multiple quantum well structures", Journal of Physics D: Applied Physics, Vol. 28, pp. 2015-9, 1995.

[Trittibach94] R. Trittibach, Ch. Grütter, J.H. Bilgram, "Surface melting of gallium single crystalls", Physical Review B, Vol. 50, pp. 2529-36, 1994.

[Wolny86] J. Wolny, S. Niziol, W. Luzny, L. Pytlik, J. Soltys, R. Kokoszka, "Structure changes in gallium near its melting point", Solid State Communications, Vol. 58, pp. 573-5, 1986.

[Zheludev95] N.I. Zheludev, P.J. Bennett, H. Loh, S.V. Popov, I.R. Shatwell, Yu.P. Svirko, V.E. Gusev, V.F. Kamalov, E.V. Slobodchikov, "Cubic optical nonlinearity of free electrons in bulk gold", Optics Letters, Vol. 20, pp. 1368-70, 1995.

[Zhou93] S. Zhou, K.K. Lee, Y.C. Chen, S. Li, "Monolithic self-Q-switched Cr,Nd:YAG laser", Optics Letters, Vol. 18, pp. 511-2, 1993.

List of Publications

P.Petropoulos, D.J.Richardson, S.Dhanjal and N.I.Zheludev, “Passive Q-switching of an erbium fibre laser using nonlinear reflection from a liquefying gallium mirror”, CLEO '98 San Francisco, USA, 3-8 May 1998, Proc 6, CTuE5, 79-80.

P.J.Bennett, S.Dhanjal, P.Petropoulos, D.J.Richardson and N.I.Zheludev, “Nonlinearity of liquefying gallium: controlling light with light at milliwatt power levels”, CLEO '98 San Francisco, USA, 3-8 May 1998, Proc 6, QME7.

P.J.Bennett, S.Dhanjal, P.Petropoulos, D.J.Richardson, N.I.Zheludev, V.I.Emelianov, “A photonic switch based on a gigantic, reversible optical nonlinearity of liquefying gallium”, Applied Physics Letters 1998 Vol.73(13) pp.1787-89.

H.Geiger, A.Fu, P.Petropoulos, M.Ibsen, D.J.Richardson, R.I.Laming, “Demonstration of a simple CDMA transmitter and receiver using sampled fibre gratings”, ECOC'98 Madrid, Spain, 20-24 September 1998, Proc. TuD10.

S.Dhanjal, V.I.Emelianov, P.Petropoulos, D.J.Richardson, N.I.Zheludev, “Nonlinearity of liquefying gallium: a breakthrough opportunity for controlling light with light at milliwatt power levels”, Proc.ICONO '98, Moscow, Russia, 1998, ThB3 (invited).

V.Albanis, S.Dhanjal, P.Petropoulos, D.J.Richardson, N.Zheludev, V.Emelyanov, “Light-induced structural phase transition in confining gallium and associated gigantic optical nonlinearity", MRS Fall Meeting Boston, USA 30 November - 4 December 1998 W7.19.

V.Albanis, P.Petropoulos, S.Dhanjal, D.J.Richardson, N.Zheludev, "Confining metallic gallium - new material structure for optical data processing at milliwatt power level", MRS Fall Meeting Boston, USA 30 November - 4 December 1998 T1.6.

P.Petropoulos, M.Ibsen, A.Fu, H.Geiger, R.I.Laming, D.J.Richardson, "Coherent control of short pulses using fibre Bragg gratings", IEE Colloquium on Optical Fibre Gratings Aston University, Birmingham 26 March 1999.

V.Albanis, S.Dhanjal, V.Emelyanov, P.Petropoulos, D.J.Richardson, N.I.Zheludev, "Dynamics of the light-induced structural phase transition in confining gallium and associated gigantic optical nonlinearity", QELS `99 Baltimore, 23-28 May 1999 (Invited)QME3.

P.Petropoulos, M.Ibsen, D.J.Richardson, "GHz-repetition-rate pulse multiplication using a sampled fiber Bragg grating", CLEO `99 Baltimore, 23-28 May 1999 CWA1.

B.C.Thomsen, P.Petropoulos, H.L.Offerhaus, D.J.Richardson, J.D.Harvey, "Characterization of a 10 GHz harmonically mode-locked erbium fiber ring laser using second harmonic generation frequency resolved optical gating", CLEO `99 Baltimore, 23-28 May 1999, CTuJ5.

S.Dhanjal, K.F.MacDonald, P.Petropoulos, D.J.Richardson, N.I.Zheludev, "Broadband optical switching in confined Gallium at milliwatt power levels", CLEO `99 Baltimore, 23-28 May 1999 CWF50.

P.Petropoulos, H.L.Offerhaus, D.J.Richardson, S.Dhanjal, N.I.Zheludev, "High energy passive Q-switching of an erbium fiber laser using a nonlinear liquifying gallium mirror", 'Novel Lasers and Devices' Topical Meeting, CLEO/Europe, Munich 13-17 June 1999 LWA7.

P.Petropoulos, S.Dhanjal, D.J.Richardson, N.I.Zheludev, "Passive q-switching of an Er3+:Yb3+ fiber laser with a fiberized liquefying gallium mirror", Optics Communications 1999 Vol.166(1-6) pp.239-43.

P.Petropoulos, H.L.Offerhaus, D.J.Richardson, S.Dhanjal, N.I.Zheludev, "Passive q-switching of fiber lasers using a broadband liquefying gallium mirror" , Appl. Phys. Lett. 1999 Vol.74(24) pp.3619-21.

P.Petropoulos, M.Ibsen, D.J.Richardson, "Rectangular pulse generation based on pulse reshaping using a superstructured fiber Bragg grating", BGPP`99 Stuart, Florida 23-25 September 1999, FC4.

P. Petropoulos, M. Ibsen, D.J. Richardson, "Shaping of soliton- into rectangular-pulses using a superstructure fiber Bragg grating", TOPS, Vol. 33, *Bragg Gratings, Photosensitivity and Poling*, (to appear).

V.Albanis, S.Dhanjal, N.I.Zheludev, P.Petropoulos, D.J.Richardson, "Cross-wavelength all-optical switching using nonlinearity of liquefying gallium", Optics Express 1999 Vol.5(8) pp.157-162.

P.Petropoulos, M.Ibsen, D.J.Richardson, M.N.Zervas, "Generation of a 40 GHz pulse stream by pulse multiplication using a sampled fiber Bragg grating", Optics Letters (accepted).

P.C.Teh, P.Petropoulos, M.Ibsen, D.J.Richardson, "A 10Gbit/s, 160Gchip/s OCDMA coding:decoding system based on superstructured fiber gratings", OFC 2000 Baltimore, 7-10 March 2000, postdeadline paper PD-9.

M.Ibsen, R.Feced, P.Petropoulos, M.N.Zervas, "99.9% reflectivity dispersion-less square-filter fibre Bragg gratings for high speed DWDM networks", OFC 2000 Baltimore, 7-10 March 2000, postdeadline paper PD-21.

P.C.Teh, P.Petropoulos, M.Ibsen, D.J.Richardson, "An Optical Processing Device based on fibre gratings", UK Patent Application, No 0005615.0 (2000).

P.Petropoulos, P.C.Teh, M.Ibsen, M.N.Zervas, D.J.Richardson, "The use of fibre Bragg gratings for advanced optical signal processing", Rank Prize Fund Mini Symposium: Microwave Photonics Grasmere, 17-20 April 2000.

P.Petropoulos, H.S.Kim, D.J.Richardson, N.I.Zheludev, "Measurement of the nonlinear optical phase response of liquefying gallium", CLEO 2000 San Francisco 7-12 May 2000, (accepted) CWK.

R.T.Bratfalean, S.Dhanjal, N.Zheludev, P.Petropoulos, D.J.Richardson, V.I.Emelyanov, "The dynamically light-induced low-reflectivity state in gallium", CLEO 2000 San Francisco, 7-12 May 2000 (accepted) CTuA.

P. Petropoulos, H.S. Kim, D.J. Richardson, V. Fedotov, N.I. Zheludev, "Measurement of the nonlinear phase response of liquefying gallium", *submitted to Applied Physics Letters* (2000).

P. Petropoulos, M. Ibsen, D.J. Richardson, "Rectangular pulse generation based on pulse reshaping using a superstructured fiber Bragg grating", *submitted to Optics Letters* (2000).

P.C. Teh, P. Petropoulos, M. Ibsen, D.J. Richardson, "160Gbit/s, 64-bit all-optical code generation and recognition using superstructured fibre Bragg gratings", *submitted to ECOC'2000.*

M. Ibsen, R. Feced, P. Petropoulos, M.N. Zervas, "High reflectivity linear-phase fibre Bragg gratings", *submitted to ECOC'2000.*